



5-2006

Structural and Magnetic Investigations of Cs_2AgF_4 and Its Doped Derivatives

Michelle Renee Dolgos
University of Tennessee, Knoxville

Recommended Citation

Dolgos, Michelle Renee, "Structural and Magnetic Investigations of Cs_2AgF_4 and Its Doped Derivatives." Master's Thesis, University of Tennessee, 2006.
https://trace.tennessee.edu/utk_gradthes/4469

This Thesis is brought to you for free and open access by the Graduate School at Trace: Tennessee Research and Creative Exchange. It has been accepted for inclusion in Masters Theses by an authorized administrator of Trace: Tennessee Research and Creative Exchange. For more information, please contact trace@utk.edu.

To the Graduate Council:

I am submitting herewith a thesis written by Michelle Renee Dolgos entitled "Structural and Magnetic Investigations of Cs_2AgF_4 and Its Doped Derivatives." I have examined the final electronic copy of this thesis for form and content and recommend that it be accepted in partial fulfillment of the requirements for the degree of Master of Science, with a major in Chemistry.

John F. C. Turner, Major Professor

We have read this thesis and recommend its acceptance:

Craig E. Barnes, Robert Compton

Accepted for the Council:

Dixie L. Thompson

Vice Provost and Dean of the Graduate School

(Original signatures are on file with official student records.)

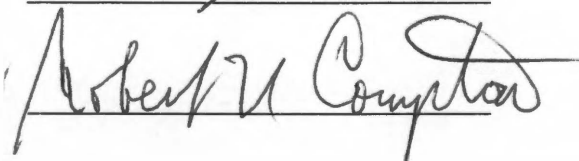
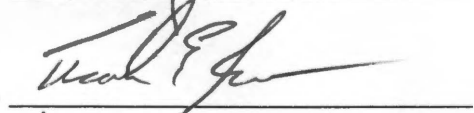
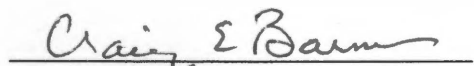
To the Graduate Council:

I am submitting herewith a thesis written by Michelle Renee Dolgos entitled "Structural and magnetic investigations of Cs_2AgF_4 and its doped derivatives." I have examined the final paper copy of this thesis for form and content and recommend that it be accepted in partial fulfillment of the requirements for the degree of Master of Science, with a major in Chemistry.



John F.C. Turner, Major Professor

We have read this thesis
and recommend its acceptance:



Acceptance for the Council:



Vice Provost and Dean of
Graduate Studies

Thesis
2006
.D65

Structural and magnetic investigations of Cs₂AgF₄ and its doped derivatives

A thesis

Presented for the

Master of Science

Degree

University of Tennessee, Knoxville

Michelle Renee Dolgos

May 2006

Dedication

This thesis is dedicated in loving memory of Stanley (5/8/1927-3/20/1998) and Mary (4/2/1928-4/15/2000) Kotlarczyk and Brett Klenow (7/25/1987-11/4/2005).

Acknowledgements

First I would like to thank my advisor, John F.C. Turner, for showing me how to be an experimental chemist. Thanks for helping me in the transition from theoretical physical chemist to experimental fluorine chemist and thank you for your patience and guidance over the last year and a half. A sincere thank you also goes to Ted Barnes, Thomas Proffen, Alan Tennant, Sylvia McLain, Peter Stephens, and Brian Sales for moving this work forward and helping me learn about the various aspects of the project. Thank you also to my committee members, John F.C. Turner, Ted Barnes, Robert Compton, and Craig Barnes. I also thank Jeff Fieberg for encouraging me to pursue a graduate degree and Steve Cook for sparking my interest in science. I would like to thank the Turner group members for always making me laugh and for answering all the dumb questions about lab type things that I dare not ask John. Mike and Laura, thank you for taking care of me, making sure that I got some rest and relaxation and ate a good meal once in awhile. Thanks for treating me like a member of your family, it means more to me than you will ever know. Jamie, thanks for being my office buddy, showing me how to blow glass, and just making me laugh. Your comical antics and sarcasm will be greatly missed. I would also like to thank Peter Yaron and Jeff Steill for not being afraid to think that science is cool. Thank you for all the engaging scientific conversations. Thanks to Brandon Farmer for teaching me the squiggly lines that are polymers. Who knew such a hand-waving type of science existed? I would like to thank my roommates Peter Yaron and Brandon Farmer for putting up with me and for sometimes peer pressuring me to drink a few beers with them or eat ice cream instead of work – you knew when I needed a break. You have made living in Knoxville enjoyable and I will miss you both. A special thanks goes to Jessica Karnik and Cheri Pfister for supporting me and listening to me go on and on about chemistry that they probably could not care less about. You two are the best friends a girl could ask for. Another special thanks goes to Fr. John O’Neill for his encouraging words, prayers, packages and letters in the mail, and inspiration. I would also like to thank Andy Kenst for his endless support and his shoulder to cry on. Thank you for providing a release when I was sick of working, and also for understanding when I needed to work. You are a truly amazing

person and I am so thankful you are a part of my life. Thanks for putting up with my erratic behavior and erratic work schedule. My biggest thanks go to God for giving me the strength and stubbornness to finish this degree, and to my parents for their constant support and for teaching me the value of an education. Mom and Dad, I am so thankful for your love and support over the years. I know I can be a pain, but I appreciate everything you have done for me.

Abstract

This thesis describes the structural and magnetic properties of solid state silver fluorides such as Cs_2AgF_4 and its doped derivatives. A wide range of techniques such as X-ray and neutron diffraction, susceptibility measurements and inelastic neutron scattering experiments are used to characterize these materials. Silver fluorides are important given their strongly correlated magnetic behavior and the potential to discover a new class of high T_C materials. Few studies have been done on silver (II) fluorides as their characterization has been problematic due to their inherent air and water sensitivity. This study is the first to accurately characterize two of these materials.

Table of contents

1 Introduction	1
1.1 A short history of magnetism	1
1.2 Quantum mechanical derivation of magnetism	2
1.2.1 A brief review of quantum numbers	2
1.2.2 Orbital angular momentum.....	3
1.2.3 Spin angular momentum	5
1.2.4 Spin-Orbit coupling	7
1.3 Magnetic Behavior	9
1.3.1 Diamagnetism and Paramagnetism.....	9
1.3.2 Cooperative magnetism	10
1.3.3 Heisenberg Hamiltonian	11
1.4 Structure	12
1.4.1 Crystal field theory	12
1.4.2 Jahn-Teller distortion.....	16
1.5 The chemistry of Ag(II)	17
1.5.1 Ag(II) compounds and superconductivity	19
1.5.2 Properties of Ag(II).....	19
1.5.3 Oxide/Fluoride analogy	20
1.5.4 Difficulties of Ag(II) synthesis	20
1.6 Theory of experimental techniques	21
1.6.1 Diffraction techniques.....	22
1.6.2 X-ray diffraction	22
1.6.3 Neutron diffraction.....	23
1.6.4 Powder diffraction and the Rietveld method	24
1.6.5 Inelastic neutron scattering	29

1.6.6 Bulk susceptibility measurements.....	30
2 Experimental.....	32
2.1 Synthesis.....	32
2.2 X-ray diffraction	32
2.2.1 Rietveld refinements	33
2.3 Neutron diffraction	34
2.3.1 Background Subtraction.....	34
2.3.2 Rietveld refinements	38
2.4 Inelastic neutron scattering.....	38
2.5 Susceptibility measurements.....	39
3 Structural and magnetic characterization of Cs₂AgF₄.....	41
3.1 Introduction.....	41
3.1.1 Previous studies of Cs ₂ AgF ₄	41
3.2 Data and results.....	45
3.2.1 X-ray diffraction	45
3.2.2 Neutron diffraction.....	48
3.2.3 Magnetic susceptibility	60
3.2.4 Inelastic Neutron Scattering.....	62
3.3 Discussion.....	70
3.3.1 Magnetism.....	70
3.3.2 Orbital ordering.....	72
3.3.3 Structure.....	75
3.3.4 Conclusion	80

4 Structural determination of Cs_{1.9}Ba_{0.1}AgF₄.....	82
4.1 Introduction.....	82
4.2 Data and results.....	84
4.2.1 X-ray diffraction	84
4.2.2 Neutron diffraction.....	87
4.2.3 Magnetism.....	99
4.3 Discussion.....	99
4.4 Conclusion	108
References.....	110
Vita.....	122

List of Tables

Table 1.1: Different types of magnetic response.	11
Table 1.2: The five <i>d</i> orbitals and their corresponding wavefunction.	16
Table 1.3: Structural radii and energetics for O ²⁻ and F ⁻	20
Table 1.4: Structures of common oxides and fluorides.	21
Table 3.1: Bond lengths from <i>I4/mmm</i> room temperature X-ray refinements for Cs ₂ AgF ₄	46
Table 3.2: ADPs from the room temperature X-ray <i>I4/mmm</i> refinement.....	46
Table 3.3: Comparison of the bond lengths from the X-ray vs. the neutron diffraction <i>I4/mmm</i> GSAS refinements.	50
Table 3.4: Thermal parameters from the room temperature neutron <i>I4/mmm</i> refinement.	50
Table 3.5: Bond lengths from the room temperature Cs ₂ AgF ₄ <i>Bbcm</i> neutron refinement.	54
Table 3.6: Thermal parameters from the room temperature <i>Bbcm</i> neutron refinement.	54
Table 3.7: Bond lengths from the Cs ₂ AgF ₄ 6K <i>I4/mmm</i> refinement.	57
Table 3.8: Thermal parameters from the low temperature <i>I4/mmm</i> refinement.	57
Table 3.9: Bond lengths from the Cs ₂ AgF ₄ 6K <i>Bbcm</i> refinement.	59
Table 3.10: Bond length comparison for K ₂ NiF ₄ , La ₂ CuO ₄ , and Cs ₂ AgF ₄ , all in the <i>I4/mmm</i> space group.	78
Table 3.11: Normalized thermal parameters from the low temperature <i>I4/mmm</i> refinement.	79
Table 3.12: Bond length comparison for K ₂ CuF ₄ and Cs ₂ AgF ₄ , in the <i>Bbcm</i> space group.	80
Table 4.1: Possible lattice parameters for Cs _{1.9} Ba _{0.1} AgF ₄ generated by Crysfire. ¹¹³	85
Table 4.2: Cs _{1.9} Ba _{0.1} AgF ₄ bond distances from the room temperature X-ray <i>I4/mmm</i> refinements.....	86
Table 4.3: Occupancies of Cs _{1.9} Ba _{0.1} AgF ₄ from room temperature X-ray refinements.	88

Table 4.4: ADPs from the room temperature X-ray <i>I4/mmm</i> refinement for $\text{Cs}_{1.9}\text{Ba}_{0.1}\text{AgF}_4$	88
Table 4.5: $\text{Cs}_{1.9}\text{Ba}_{0.1}\text{AgF}_4$ bond distances from the room temperature neutron refinements with a comparison to the distances from the X-ray refinement.	90
Table 4.6: ADPs from the room temperature neutron <i>I4/mmm</i> refinement for $\text{Cs}_{1.9}\text{Ba}_{0.1}\text{AgF}_4$	90
Table 4.7: Occupancies of the atoms in $\text{Cs}_{1.9}\text{Ba}_{0.1}\text{AgF}_4$ given by the room temperature <i>I4/mmm</i> neutron refinement.	90
Table 4.8: $\text{Cs}_{1.9}\text{Ba}_{0.1}\text{AgF}_4$ bond distances from the room temperature neutron refinements using the <i>Bbcm</i> space group.....	93
Table 4.9: ADPs from the room temperature neutron <i>Bbcm</i> refinement for $\text{Cs}_{1.9}\text{Ba}_{0.1}\text{AgF}_4$	94
Table 4.10: Occupancies of the atoms in $\text{Cs}_{1.9}\text{Ba}_{0.1}\text{AgF}_4$ given by the room temperature <i>Bbcm</i> neutron refinement.	94
Table 4.11: $\text{Cs}_{1.9}\text{Ba}_{0.1}\text{AgF}_4$ bond distances from the low temperature <i>I4/mmm</i> refinements.....	97
Table 4.12: ADPs from the low temperature neutron <i>I4/mmm</i> refinement for $\text{Cs}_{1.9}\text{Ba}_{0.1}\text{AgF}_4$	97
Table 4.13: Occupancies of the atoms in $\text{Cs}_{1.9}\text{Ba}_{0.1}\text{AgF}_4$ given by the low temperature <i>I4/mmm</i> neutron refinement.	97
Table 4.14: $\text{Cs}_{1.9}\text{Ba}_{0.1}\text{AgF}_4$ bond distances from the low temperature <i>Bbcm</i> refinements.	100
Table 4.15: Occupancies of the atoms in $\text{Cs}_{1.9}\text{Ba}_{0.1}\text{AgF}_4$ given by the low temperature <i>Bbcm</i> neutron refinement.	101
Table 4.16: ADPs from the low temperature neutron <i>Bbcm</i> refinement for $\text{Cs}_{1.9}\text{Ba}_{0.1}\text{AgF}_4$	101
Table 4.17: Comparison of Cs_2AgF_4 , and $\text{Cs}_{1.9}\text{Ba}_{0.1}\text{AgF}_4$ lattice parameters assuming the space group <i>I4/mmm</i>	105

List of Figures

Figure 1.1: a) Crystal structure of Fe_3O_4 and b) mineral form of magnetite.	2
Figure 1.2: Orbital angular momentum showing the z -component.	4
Figure 1.3: Quantization of the z -component of the spin angular momentum.	6
Figure 1.4: Zeeman Effect of the $J=2$ energy state.....	8
Figure 1.5: Spin interactions, including the direction and magnitude for a) an antiferromagnet, b) a ferromagnet, and c) a ferrimagnet.	12
Figure 1.6: Energy splitting of the d orbitals due to a crystal field of an octahedrally coordinated metal center.	15
Figure 1.7: Example of Jahn-Teller distortion occurring with the d orbitals of an octahedrally coordinated metal-ligand complex.	18
Figure 1.8: a) X-ray scattering intensity as a function of atomic number, b) Neutron scattering cross section as a function of atomic number.....	25
Figure 1.9: Gaussian peak shape versus the Lorentzian peak shape with $\mu = 0$ and $\sigma = 1$	28
Figure 1.10: Change in wavevector when a) energy is lost and b) when energy is gained.	30
Figure 2.1: Schematic drawing similar to the X3B1 X-ray diffractometer.	33
Figure 2.2: Simple schematic of interior of NPDF.....	35
Figure 2.3: a) Cs_2AgF_4 before background subtraction and absorbance correction. Note the amorphous quartz peaks and the absorbance at low Q values. b) Cs_2AgF_4 after background subtraction and absorbance correction.....	37
Figure 3.1: Perovskite stacking scheme for the a) $n=1$, b) $n=2$, and c) $n=3$ Ruddlesden-Popper phases. A perovskite unit cell can be seen in d). ⁸²	42
Figure 3.2: Susceptibility data of Hoppe fit to a 10 th order 2D Heisenberg ferromagnet with paramagnetic behavior above T_C . ⁸⁴⁻⁸⁶	43
Figure 3.3: Ortep of Cs_2AgF_4 from the room temperature X-ray $I4/mmm$ refinements. The red atoms are silver, blue atoms are cesium, and the green atoms are fluorine.....	47

Figure 3.4: Three phase Cs_2AgF_4 Rietveld refinement for $I4/mmm$ space group at room temperature. The black tick marks represent Cs_2AgF_4 peaks, the red represent AgF, and the blue tick marks represent CsF. The red crosses indicate the data while the green lines represent the model. The purple pattern at the bottom represents the residual between the model and the data.	47
Figure 3.5: $S(Q)$ of Cs_2AgF_4 factor for the three detector banks of NPDF. The data extends out to around Q values of 40 \AA^{-1} depending on the bank, but the data is only shown up to $Q=10 \text{ \AA}^{-1}$ to better see the scattering at low Q	49
Figure 3.6: Ortep of Cs_2AgF_4 in the $I4/mmm$ space group at room temperature from the neutron data.....	52
Figure 3.7: Three phase neutron Rietveld refinement using the $I4/mmm$ space group. The black represents the Cs_2AgF_4 peaks, the red marks represent the positions of AgF, and the blue represent CsF. The data in this plot is from the 148° bank of NPDF.	52
Figure 3.8: Comparison of the a) $I4/mmm$ and b) $Bbcm$ unit cells for an $n=1$ Ruddlesden-Popper phase.	53
Figure 3.9: Ortep of Cs_2AgF_4 from the room temperature $Bbcm$ neutron refinements..	55
Figure 3.10: Rietveld refinement from the 148° detector bank of the room temperature Cs_2AgF_4 neutron data assuming the $Bbcm$ space.....	55
Figure 3.11: Rietveld refinement of the 48° bank of NPDF using the $I4/mmm$ space group for Cs_2AgF_4 at 6K.....	58
Figure 3.12: Cs_2AgF_4 unit cell model at 6K in the $I4/mmm$ space group. The blue atoms represent cesium, the red are silver, and the green atoms are fluorine.	58
Figure 3.13: Example of a split site model for the equatorial fluorines. Each fluorine has an occupancy of $1/2$	59
Figure 3.14: Rietveld refinement of the 48° bank of Cs_2AgF_4 data at 6K using the $Bbcm$ space group.	60
Figure 3.15: Magnetization data of Cs_2AgF_4 as a function of temperature.	61
Figure 3.16: Fit of the 10^{th} order ferromagnetic 2D Heisenberg model susceptibility to Cs_2AgF_4 , using data above the Curie temperature. ⁸⁴⁻⁸⁶	63

Figure 3.17: a) Cs ₂ AgF ₄ inelastic neutron scattering data for E _i =50meV, T=8K, before background subtraction and b) after background subtraction.....	64
Figure 3.18: Cs ₂ AgF ₄ inelastic neutron scattering data with E _i =50meV and T=8K. The scattering intensity at these higher temperatures is due to phonons.	65
Figure 3.19: PTFE and aluminum can background data at E _i =50K. Note the elastic peak at Q=1.3Å ⁻¹	66
Figure 3.20: Simulated inelastic scattering pattern of Cs ₂ AgF ₄ at E _i =50 for a) a2D Heisenberg antiferromagnet, and b) a 2D Heisenberg ferromagnet.	68
Figure 3.21: Cs ₂ AgF ₄ inelastic scattering data at 8K fit to the ferromagnetic, cosinusoidal dispersion relation.	69
Figure 3.22: Antiferromagnetic array in the CuO ₂ planes of La ₂ CuO ₄ . ⁹⁷ The arrows on the oxygen in the center octahedra represent the direction of rotation that causes the orthorhombic distortion.	71
Figure 3.23: Orbital ordering for a) <i>b_{1g}</i> ground state, b) <i>a_{1g}</i> ground state, and c) linear combination of <i>z²-y²</i> and <i>z²-x²</i> <i>d</i> -orbitals as a possible ground state.....	73
Figure 3.24: Formation of a <i>b_{1g}</i> ground state with partial filled <i>x²-y²</i> orbitals (left) is accompanied by axial extension of octahedral ligands (right).....	74
Figure 3.25: Anharmonic coupling to ligands favors the formation of staggered orbital ordering of <i>z²-x²</i> and <i>z²-y²</i> orbitals, as in K ₂ CuF ₄ . In-plane ligands are displaced from central positions, lowering the crystal symmetry. Strong ferromagnetic super-exchange occurs through the unfilled in-plane orbitals.	76
Figure 3.26: The unit cell of K ₂ NiF ₄ including the thermal parameters. Lattice parameters are <i>a</i> = <i>b</i> = 4.013 Å and <i>c</i> = 13.088 Å. The pink atoms are nickel, green atoms are fluorine, and the brown atoms are potassium.....	77
Figure 3.27: Ortep of K ₂ CuF ₄ which is of the <i>Bbcm</i> space group. The blue atoms represent copper, the green is fluorine, and the brown atoms are potassium.	77
Figure 3.28: <i>χ²</i> value versus fluorine displacement for the low temperature Cs ₂ AgF ₄ data. The fluorine displacement is Δ <i>r</i> which is the distance from the symmetric <i>I4/mmm</i> fluorine position to the displaced <i>Bbcm</i> fluorine position.	81

Figure 4.1: Phase diagram of $\text{La}_{2-x}\text{A}_x\text{CuO}_4$ ($\text{A}=\text{Ba}, \text{Sr}$). The abbreviations are AF(antiferromagnet), SG(spin glass), SC(superconducting), T_N (Neél Temperature), T_C (critical temperature), I (insulator), M (metal), O (orthorhombic), and T (tetragonal).¹¹¹ 83

Figure 4.2: Ortep, or unit cell representation of $\text{Cs}_{1.9}\text{Ba}_{0.1}\text{AgF}_4$ from the room temperature X-ray refinements. A split site refinement was performed where the grey atoms are barium and the blue atoms are cesium 89

Figure 4.3: Four phase $I4/mmm$ refinement of the room temperature X-ray data for $\text{Cs}_{1.9}\text{Ba}_{0.1}\text{AgF}_4$. The green tickmarks represent the peak positions for $\text{Cs}_{1.9}\text{Ba}_{0.1}\text{AgF}_4$, the blue tickmarks are for CsF, red for AgF, and black for BaF_2 89

Figure 4.4: Model of $\text{Cs}_{1.9}\text{Ba}_{0.1}\text{AgF}_4$ based on the room temperature neutron refinements assuming an $I4/mmm$ space group 92

Figure 4.5: Rietveld refinement of the room temperature neutron data assuming an $I4/mmm$ space group. The black tickmarks represent $\text{Cs}_{1.9}\text{Ba}_{0.1}\text{AgF}_4$, the red AgF, the blue, CsF, and the green, BaF_2 92

Figure 4.6: $Bbcm$ Rietveld refinement of $\text{Cs}_{1.9}\text{Ba}_{0.1}\text{AgF}_4$ using the room temperature neutron data..... 95

Figure 4.7: Model of $\text{Cs}_{1.9}\text{Ba}_{0.1}\text{AgF}_4$ based on the room temperature $Bbcm$ refinements. 95

Figure 4.8: $I4/mmm$ Rietveld refinement for $\text{Cs}_{1.9}\text{Ba}_{0.1}\text{AgF}_4$ using the low temperature neutron data..... 98

Figure 4.9: Model of $\text{Cs}_{1.9}\text{Ba}_{0.1}\text{AgF}_4$ based on the low temperature $I4/mmm$ neutron refinement. 98

Figure 4.10: Four phase Rietveld refinement for $\text{Cs}_{1.9}\text{Ba}_{0.1}\text{AgF}_4$ using the $Bbcm$ space group. 102

Figure 4.11: Ortep of $\text{Cs}_{1.9}\text{Ba}_{0.1}\text{AgF}_4$ using the $Bbcm$ refinements. 102

Figure 4.12: Magnetization of $\text{Cs}_{1.9}\text{Ba}_{0.1}\text{AgF}_4$ from versus temperature..... 103

Figure 4.13: Magnetization curves comparing undoped Cs_2AgF_4 to doped $\text{Cs}_{1.9}\text{Ba}_{0.1}\text{AgF}_4$ 104

Figure 4.14: Ortep of $\text{La}_{1.83}\text{Sr}_{0.17}\text{CuO}_4$. The green atoms represent oxygen, the blue atoms represent La/Sr and the pink atoms represent copper..... 107

1 Introduction

Magnetochemistry is defined as the study of the relationship between magnetic properties and physical and chemical structure. The following chapter will be divided into three parts; firstly, an introduction to some of the basic concepts of magnetism and how it relates to the chemical structure of a material; secondly, a summary of the chemistry of Ag^{II} together with a brief overview of the high- T_{C} cuprates, and thirdly, a summary of the theory underlying the experimental techniques used to study these compounds.

1.1 A short history of magnetism

The phenomenon of magnetism has been known since the time of early man through observations of the mineral known today as magnetite or Fe_3O_4 . Magnetite is naturally magnetic, attracts iron, and will act as a compass. The structure of Fe_3O_4 and a picture of the mineral can be seen in Figure 1.1. References to the magnetic stone are present in literature of Plato and the ancient Greeks, but it is thought that they did not understand the properties or possible uses of magnets and only concerned themselves with it because they believed it possessed mystic powers.^{1,2} The first recorded use of these stones as directional devices was by the Chinese philosopher Shen Kua in A.D. 1080, but they may have been used by the Chinese thousands of years earlier.² These stones, which later became known as lodestones, transformed travel, especially sea-borne navigation. This application also inspired early interest in magnetic materials.

Despite the increased interest in magnetic phenomena, little progress was made until the 19th century. In 1819 Hans Christian Ørsted discovered the relationship between electricity and magnetism by showing that an electric current was able to deflect a magnetic compass, thereby showing that an electric current generated a magnetic field.¹⁻³ This discovery led to a series of advances in magnetism that has allowed magnetic materials to become a crucial component of modern technology. Today magnets and magnetic materials are used in a wide range of applications, including electrical power applications such as transformers and motors, and also medical uses such as MRI (Magnetic Resonance Imaging).

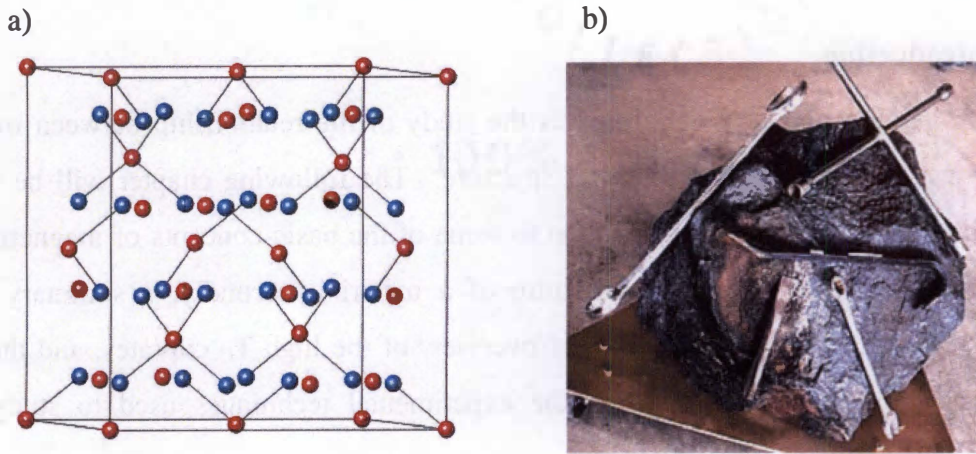


Figure 1.1: a) Crystal structure of Fe₃O₄ and b) mineral form of magnetite.

1.2 Quantum mechanical derivation of magnetism

When considering the atomic origin of magnetism, it is necessary to look at the orbital and spin properties of electrons.³ The following sections provide an overview of the quantum mechanical description of magnetism. Many books detail this topic with the following quantum mechanics summary drawn mostly from references 1-11.¹⁻¹¹

1.2.1 A brief review of quantum numbers

Solutions of the Schrödinger equation

$$-\frac{\hbar^2}{2m} \left\{ \nabla^2 - \frac{e^2}{r} \right\} \psi = E \psi \quad 1.1$$

for a single electron bound in an atom, take the form

$$\psi = R(r) \cdot \Theta(\vartheta) \cdot \Phi(\phi) \quad 1.2$$

when the calculation is performed in spherical polar coordinates (r, ϑ, ϕ) . Each of these independent functions is labeled using a quantum number. The quantum number associated with the radial function, $R(r)$ is n , the principle quantum number. This number determines the shell structure of the atom and therefore the row in the periodic table in which the element resides.

The combined angular functions, $\Theta(\vartheta) \cdot \Phi(\phi)$ take the form

$$\Theta(\vartheta) \cdot \Phi(\phi) = Y_m^l \cdot e^{im\phi} \quad 1.3$$

where Y_m^l is a spherical harmonic and l and m are the angular quantum numbers. l is the orbital quantum number, which determines the chemical group in which the element is placed, and m is the magnetic quantum number.

1.2.2 Orbital angular momentum

The angular functions $\Theta(\vartheta) \cdot \Phi(\phi)$ are also suitable wave functions for the quantum mechanical description of orbital angular momentum, which arises from the orbital motion of electrons around a nucleus. The orbital angular momentum operators are defined as

$$l_x = -i\hbar \left(y \frac{\partial}{\partial z} - z \frac{\partial}{\partial y} \right) \quad 1.4$$

$$l_y = -i\hbar \left(z \frac{\partial}{\partial x} - x \frac{\partial}{\partial z} \right) \quad 1.5$$

$$l_z = -i\hbar \left(x \frac{\partial}{\partial y} - y \frac{\partial}{\partial x} \right) \quad 1.6$$

$$l^2 = l_x^2 + l_y^2 + l_z^2 \quad 1.7$$

where the operators are found by replacing the coordinates and momenta in the classical equations with their quantum mechanical operators.⁷ These operators can be evaluated by determining their commutation relations. One of the rules of commutation states that $[A, B]$ must equal zero for two observables to be simultaneous measurable.¹² The commutation relations of orbital angular momentum are as follows

$$[l_x, l_y] = i\hbar l_z \quad 1.8$$

$$[l_y, l_z] = i\hbar l_x \quad 1.9$$

$$[l_z, l_x] = i\hbar l_y \quad 1.10$$

$$[l^2, l_x] = 0 \quad 1.11$$

$$[l^2, l_y] = 0 \quad 1.12$$

$$[l^2, l_z] = 0 \quad 1.13$$

where $[A, B] = AB - BA$. Because l^2 commutes with each of the components, an exact value for l^2 and one vector component can be measured at the same time, but the system as a whole cannot be assigned values simultaneously as the vector components do not commute with each other.⁷

Another interesting property of orbital angular momentum is that l^2 is an eigenvector of each spherical harmonic

$$l^2 Y_m^l = l(l+1)\hbar^2 Y_m^l \quad 1.14$$

where l is the orbital angular momentum vector operator, l is the orbital quantum number, \hbar is $h/2\pi$ where h is Planck's constant, and Y_m^l is the spherical harmonic.

The magnetic quantum number m in the spherical harmonics defines the component of the vector l in a chosen direction.¹ This direction is traditionally chosen as the z vector with the spherical harmonics being eigenfunctions of this operator giving the relation

$$l_z Y_m^l = \hbar m Y_m^l \quad 1.15$$

which shows that the angular momentum values are quantized as shown in Figure 1.2.

It is also possible to find the eigenvalues of the eigenvectors l^2 and l_z by using the raising and lowering operators

$$l_+ = l_x + il_y \quad 1.16$$

$$l_- = l_x - il_y \quad 1.17$$

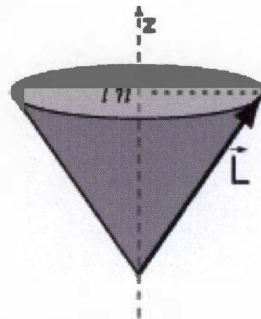


Figure 1.2: Orbital angular momentum showing the z -component.

The commutation relationship between raising operator and the z component of angular momentum is

$$[l_+, l_z] = -\hbar l_+ \quad 1.18$$

which can be used to show that

$$l_z l_+ = \hbar(m+1)l_+ |lm\rangle \quad 1.19$$

using Dirac notation.⁹ Therefore $l_+ |lm\rangle$ is an eigenfunction of l_z which shows that

$$l_+ |lm\rangle \propto |lm+1\rangle \quad 1.20$$

When $l_+ |lm\rangle$ is normalized the following relationship is established

$$l_{\pm} |lm\rangle = \hbar \sqrt{l(l+1) - m(m \pm 1)} |lm \pm 1\rangle \quad 1.21$$

which is often used for evaluating integrals.⁹

The orbital quantum numbers give rise to the shape and orientation of the orbitals which are linear combinations of the spherical harmonics.⁹ For example, an l value of 1 is a p orbital and has three possible orientations on the x , y , or z axis and the d orbitals possess an l value of 2 with five possible orientations.

All of these above expressions only describe the angular momentum vector of one electron. In atoms and molecules with multiple electrons, the total orbital angular momentum is simply the vector sum of all the individual l values

$$L = \sum_i l_i \quad 1.22$$

where the summation extends over all the electrons.³

1.2.3 Spin angular momentum

Electrons also possess an intrinsic angular momentum that is known as spin which is governed by the same rules as orbital angular momentum. The spin commutation relations are

$$[s_x, s_y] = i\hbar s_z \quad 1.23$$

$$[s_y, s_z] = i\hbar s_x \quad 1.24$$

$$[s_z, s_x] = i\hbar s_y \quad 1.25$$

$$[s^2, s_x] = 0 \quad 1.26$$

$$[s^2, s_y] = 0 \quad 1.27$$

$$[s^2, s_z] = 0 \quad 1.28$$

which indicate that, as in orbital angular momentum, the components of the spin angular momentum cannot be measured at the same time and only s^2 and one vector component may be measured simultaneously.

Spin angular momentum and the spherical harmonics are analogous to the eigenvalue/eigenfunction relationship of orbital angular momentum and the spherical harmonics and give the following relationships

$$s^2 |sm_s\rangle = \hbar^2 s(s+1) |sm_s\rangle \quad 1.29$$

$$s_z |sm_s\rangle = \hbar m_s |sm_s\rangle \quad 1.30$$

and show the quantization of spin angular moment which can be seen in Figure 1.3.

The spin eigenvalues of s_z are

$$s_z \alpha = \frac{1}{2} \hbar \alpha \quad 1.31$$

$$s_z \beta = -\frac{1}{2} \hbar \beta \quad 1.32$$

where

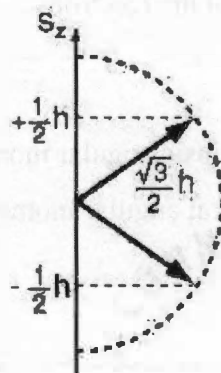


Figure 1.3: Quantization of the z-component of the spin angular momentum.

$$|\alpha\rangle = \left| \frac{1}{2} \frac{1}{2} \right\rangle \quad 1.33$$

$$|\beta\rangle = \left| \frac{1}{2} -\frac{1}{2} \right\rangle. \quad 1.34$$

Also, because s_z commutes with s^2 , the eigenfunctions of s_z are the same as those of s^2 so the eigenvalues with $s = 1/2$ are

$$s^2 \alpha = \frac{3}{2} \hbar^2 \alpha \quad 1.35$$

$$s^2 \beta = \frac{3}{2} \hbar^2 \beta. \quad 1.36$$

Similar to orbital angular momentum, these equations for spin angular momentum only take into account one electron. The total spin angular momentum can be expressed as

$$\mathbf{S} = \sum_i \mathbf{s}_i \quad 1.37$$

where the total spin angular momentum is a sum of the individual s values each electron.

1.2.4 Spin-Orbit coupling

In an unfilled shell of the electrons of a free ion, there is a coupling between the spin and orbital angular momentum which is known as Russell-Saunders coupling.⁶ In Russell-Saunders coupling, the total orbital angular momentum vector and the total spin angular momentum vector are simply added together

$$\mathbf{J} = \mathbf{L} + \mathbf{S} \quad 1.38$$

where the J values can range from $L - S$ to $L + S$. Therefore J will have a multiplicity of $2J + 1$ degenerate levels.

The degeneracy of these electronic states will be split into states of different energy levels when a magnetic field is present. The term for this lifting of degeneracy is called the Zeeman Effect and an example of this energy level splitting can be seen in Figure 1.4. The energy level which is dependant on J is

$$E_{M_j} = m_j g_J \mu_B \mathbf{B} \quad 1.39$$

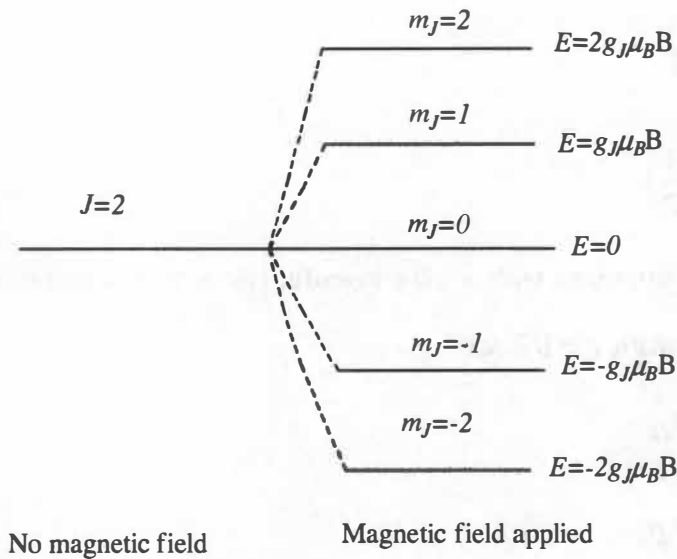


Figure 1.4: Zeeman Effect of the $J=2$ energy state.

where E_{M_j} is called the Zeeman coefficient and is equal to the energy of the perturbed wavefunction, g_J is the Landé splitting factor for a specific J state and is essentially the ratio between the magnetic moment and 1 Bohr magneton, μ_B is the magnetic moment and B is the magnetic field vector⁶. The separation between each m_J energy levels is $g_J \mu_B B$.

The split in the energy levels causes different terms to arise that are unequal in energy. When Zeeman splitting occurs, Hund's rules are used to determine the lowest energy state. Hund's rules are as follows: 1) Of terms arising from a particular configuration those with the most unpaired electrons (maximum S value) lie lowest, 2) if there is more than one term with maximum spin multiplicity, the lowest is that of the higher L value and 3) when an atom has a less than half filled shell, the term with the lowest J values has the lowest energy.⁵

1.3 Magnetic Behavior

1.3.1 Diamagnetism and Paramagnetism

One of the weakest forms of magnetism is known as diamagnetism. This form of magnetism is temperature independent, and is clearly evident in closed shell atoms. It is present to some degree in all materials, but is usually masked by paramagnetism.⁴ In diamagnetic materials, an induced magnetic moment occurs which causes the magnetization and the susceptibility to be negative.^{1,2,4} The negative susceptibility displayed follows from Lenz's law of electromagnetic induction.¹ Lenz's law states that when a magnetic field is applied, the flux enclosed by a current loop is changed and a current is induced in a direction which opposes the magnetic field.³

The susceptibility of a diamagnetic material is proportional to the average squared radius of the electron occupied orbitals

$$\chi_{dia} = -\left(\frac{N_A e^2}{6mc^2}\right) \sum_i \bar{r}_i^2 \quad 1.40$$

where χ_{dia} is the susceptibility per kilogram atom, N_A is Avogadro's number, r_i is the radius of the orbital of electron i , and the summation extends over all the electrons of the atom.⁶

Paramagnetism occurs in materials with open shell atoms and results in a positive susceptibility, unlike in diamagnetism. The electrons in paramagnetic materials are uncorrelated magnetically. However, when exposed to a magnetic field there is some orientation of atomic dipoles but the alignment is generally weak due to rapid thermal motion, thus causing the effect to be strongly temperature dependent.^{1,4} Most materials are paramagnetic at high temperature because the thermal energy, kT , is much greater than the energy of aligned spins.⁶ At higher temperatures the susceptibility of an ideal paramagnet with thermal energy, kT is given by

$$\chi_m = \frac{C}{T} \quad 1.41$$

which is known as the Curie law. Here C is the Curie constant, and T is the temperature.

When there are multiple energy level states for example, when the Zeeman Effect occurs, the electron populations of these states are described by a Boltzmann distribution. The susceptibility in this case is given by the van Vleck equation which is simply a sum over these energy states

$$\chi_A = N_A \frac{\sum_i [(E_i^I)^2 / kT - 2E_i^{II}] \exp(-W_i^0 / kT)}{\sum_i (\exp - E_i^0 / kT)} \quad 1.42$$

where the sum is over all electrons, E_i^0 is the unperturbed energy, E_i^I and E_i^{II} are the perturbed energies of the first and second order Zeeman Effect where the first order Zeeman Effect only includes the ground state while the second order Zeeman Effect includes higher levels.

1.3.2 Cooperative magnetism

The orientation of electrons in diamagnetic and paramagnetic materials is not strongly affected by electron-electron interactions. There are however magnetic materials in which the magnetism does display cooperative properties. These cooperative properties generally only occur at low temperature. This phenomenon is due to the fact that at low temperatures, the energy of the aligned spins is able to overcome the thermal energy and thermal fluctuations.

One such type of magnetism is antiferromagnetism, which is common among magnetic insulators. Most antiferromagnetic materials are paramagnets at room temperature, but at a certain temperature known as the Néel Temperature, T_N , the dipoles align in an antiparallel arrangement.^{1,4} In this arrangement, half of the dipoles orient with the magnetic field while the others oppose the first half with the coupling between the electrons stronger than the interaction with the field.¹

Another type of less common cooperative magnetism is known as ferromagnetism. Ferromagnetism shows the strongest magnetism of all the types mentioned as shown in Table 1.1. Like antiferromagnets, most ferromagnetic materials are paramagnets at high temperature due to thermal fluctuations. However, at a certain temperature known as the Curie point, the dipoles spontaneously orient with the electrons all arranged parallel to the applied magnetic field. Most ferromagnetic materials are

Table 1.1: Different types of magnetic response.

Effect	Magnitude ^a	Temperature dependant?	Applied field dependant?
Diamagnetism	-10^{-3}	No	No
Paramagnetism	1	Yes	No
Antiferromagnetism	<0.1	Yes	Yes
Ferromagnetism	10^7	Yes	Yes
Ferrimagnetism	10^6	Yes	Yes

^a compared to a typical paramagnetic susceptibility of $10^{-8} \text{ m}^3 \text{ mol}^{-1}$ at 300K.

metallic and interestingly, often retain magnetic properties when the applied field is taken away.

A third type of magnetism is known as ferrimagnetism which is the type of magnetism displayed by the first known magnetic material, magnetite. Many Fe(III) compounds which contain oxygen order at what is called the ferrimagnetic Néel temperature. In these types of materials, the metal ions are positioned in sublattices with different numbers of ions.¹ Nearest neighbor ions belong to different sublattices and arrange in an antiparallel manner as the coupling between the nearest ions is stronger than the coupling between the ions in the sublattice. This interaction results in sublattices with different magnetizations, with the net effect being ferromagnetic in the direction of the higher populated sublattice. Figure 1.5 shows the interactions of the types of cooperative magnetism mentioned.

1.3.3 Heisenberg Hamiltonian

The Heisenberg Hamiltonian is used in quantum mechanics to describe the energy of a magnetically ordered state. The Hamiltonian is a sum over all pairs of electrons

$$H = J_{ij} \sum_{\substack{i < j \\ i \neq j}} \mathbf{S}_i \cdot \mathbf{S}_j \quad 1.43$$

where \mathbf{S}_i and \mathbf{S}_j are the atomic spin vectors of the i^{th} and j^{th} atom and J is the exchange interaction between atoms i and j . In most cases, it is necessary to use only the nearest neighbor atoms pairs. Because the exchange constant depends on the degree of overlap

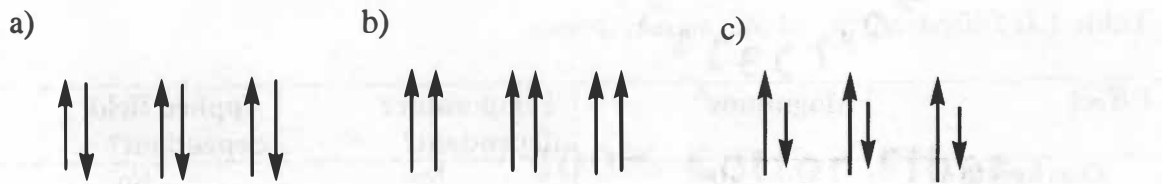


Figure 1.5: Spin interactions, including the direction and magnitude for a) an antiferromagnet, b) a ferromagnet, and c) a ferrimagnet.

between the two atomic wave functions some interactions will be coupled more strongly than others. Therefore J is a measure of the interaction between two spins. This exchange constant is also able to distinguish between cooperative magnetic behavior that causes the electron spins to align parallel (ferromagnetic) to each other or in an antiparallel (antiferromagnetic) arrangement. If $J < 0$ then the material displays ferromagnetic properties and if $J > 0$ it is an antiferromagnet.

1.4 Structure

1.4.1 Crystal field theory

Crystal field theory was first introduced by John H. van Vleck in the early 1930's as an alternative to the valence bond theory developed by Linus Pauling just a few years earlier.¹³ It is an ionic model which is used to explain the effects on a point charge from an electrostatic potential due to electron-electron repulsions and spin-orbit coupling. This theory is often used when studying transition metal complexes. The d orbitals in transition metals have a $2J+1$ ground state degeneracy, but when electrostatic interactions occur, the degeneracy is lifted and the energy splits into different levels. As a result of this splitting the magnetic, structural, and energetic properties of the material are affected.

When a point charge is surrounded by ions in an octahedral arrangement, the electrostatic potential is

$$V_{x,y,z} = \sum_{i=1}^6 \frac{e z_i}{r_{ij}} \tag{1.44}$$

where $V_{x,y,z}$ is the potential caused by the i^{th} ion, e is the charge of an electron, and r_{ij} is the distance from the point charge to the i^{th} surrounding ion. The inverse of r_{ij} can be expanded into

$$\frac{1}{r_{ij}} = \sum_{n=0}^{\infty} \sum_{m=-n}^n \frac{4\pi}{2n+1} \cdot \frac{r^n}{a^{n+1}} \cdot Y_{n,j}^l Y_{n,i}^l \quad 1.45$$

where a is the coordinate of the ligand where the transition metal is the center point, and Y_l^m are the spherical harmonics of the point charge and the corresponding ligand. When expanding out this summation, it is only necessary to include terms up to $n=4$. The reason for this is because the d orbitals have an l value of 2 and therefore the integrals with a product of a d orbital spherical harmonic with a spherical harmonic that has an l value greater than twice its own value will be equal to zero.⁶ By expanding the r_{ij} to $n=4$, $V_{x,y,z}$ becomes

$$V_{Oh} = \sqrt{\frac{49}{18}} \cdot \sqrt{2\pi} \frac{ze^4}{a_5} \left[Y_4^0 + \sqrt{\frac{5}{14}} (Y_4^4 + Y_4^{-4}) \right] \quad 1.46$$

and leads to the splitting of the d orbitals.⁶

This potential which is specific to octahedral complexes is used as a perturbation in the Hamiltonian

$$H'\psi' = E'\psi' \quad 1.47$$

where

$$H' = H_o + H_1 \quad 1.48$$

And

$$H_o = -\frac{\hbar^2}{2m} \nabla^2 \quad 1.49$$

$$H_1 = V_{Oh} \cdot \quad 1.50$$

To solve the eigenvalue problem for this perturbed system, the determinant of a matrix is calculated to minimize the energy. The matrix of the five d wave functions ($\psi_2, \psi_1, \psi_0, \psi_{-1}, \psi_{-2}$) is set up so that each matrix element is

$$H_{ij}^1 = \int \psi_i^* H \psi_j d\tau \quad 1.51$$

With the matrix diagonalized to determine the energies of the d orbitals.⁶

The determinant of the diagonalized matrix is reduced to

$$\begin{vmatrix} D_q - E & 0 & 0 & 0 & 5D_q \\ 0 & -4D_q - E & 0 & 0 & 0 \\ 0 & 0 & 6D_q - E & 0 & 0 \\ 0 & 0 & 0 & -4D_q - E & 0 \\ 5D_q & 0 & 0 & 0 & D_q - E \end{vmatrix} \quad 1.52$$

Which give energies of

$$E(\psi_1) = E(\psi_2) = E(-i2^{-1/2}[\psi_2 - \psi_{-2}]) = -4D_q \quad 1.53$$

$$E(d_0) = E(2^{1/2}[\psi_2 + \psi_{-2}]) = 6D_q \quad 1.54$$

where

$$Dq = \frac{1}{6} \left(\frac{ze^2 r^4}{a} \right) \quad 1.55$$

This solution shows that there are three orbitals with an energy of $-4Dq$ which make up the t_{2g} orbitals and there are two orbitals with energies of $6Dq$ which are called the e_g orbitals and can be seen in Figure 1.6. Table 1.2 shows which wavefunctions represent which orbitals.

The electrons in these orbitals follow Hund's rules for arranging the electrons. There are two possible ways to configure the electrons depending on if the complex follows the rules for low spin or high spin. There is a need to balance between maximizing the multiplicity and overcoming the repulsive energy that arises when two electrons are placed in the same orbital.¹⁴ In complexes with high spin electron configuration, a weak field is said to exist and Δ is small. In a high spin octahedral complex, one electron is placed in each of the five orbitals before the spins are paired in the same orbital. In low spin states, a high Δ is observed and a strong field is present. For octahedral complexes with low spin, the t_{2g} orbitals are completely filled before electrons can be placed in the higher energy e_g orbitals because the repulsion energy is smaller than the energy between the two levels.

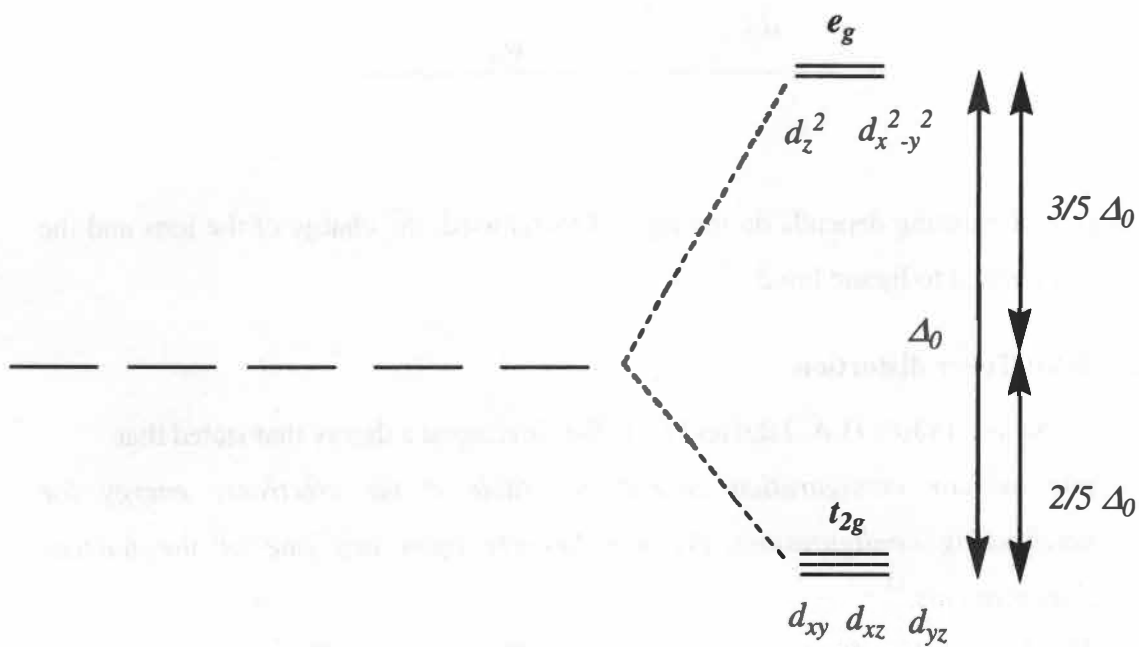


Figure 1.6: Energy splitting of the d orbitals due to a crystal field of an octahedrally coordinated metal center.

Table 1.2: The five d orbitals and their corresponding wavefunction.

d orbital	wavefunction
d_{xz}	ψ_1
d_{yz}	ψ_{-1}
d_{xy}	$-i2^{-1/2}[\psi_2 - \psi_{-2}]$
$d_{x^2-y^2}$	$2^{-1/2}[\psi_2 + \psi_{-2}]$
$d_{z^2-r^2}$	ψ_0

The degree of splitting depends on the type of metal used, the charge of the ions and the nature of the metal to ligand bond.

1.4.2 Jahn-Teller distortion

In the late 1930's H.A. Jahn and E. Teller developed a theory that stated that *any nuclear configuration cannot be stable if the electronic energy for neighboring configurations depends linearly upon any one of the nuclear displacements.*¹⁵

The Jahn-Teller effect can occur in two different forms: first order and second order. What is known today as a first order Jahn-Teller distortion is what the original paper by Jahn and Teller discussed.¹⁶ First order distortions arise from orbitally degenerate electronic states and usually only occurs in partially filled shells with orbitals that are doubly or triply degenerate such as in d orbitals with t_{2g} or e_g symmetry.¹⁷ In order to gain stability, any non-linear molecule with degenerate electronic states, will distort to reach a lower energy state.

This theory of distortion is supported by applying group theory to the perturbation theory of quantum mechanics.¹⁵ The displacement of a coordinate is

$$Q = Q_0 + \sum_i Q_i \eta_i \quad 1.56$$

where η_i is a nonsymmetrical displacement.¹⁵ The Hamiltonian is expanded as a power series with the variable η_i

$$H = H_0 + \sum_i V_i(q)\eta_i + \sum_{ij} V_{ij}(q)\eta_i\eta_j \quad 1.57$$

where H_0 is the regular Hamiltonian, and $V_i(q)$ and $V_{ij}(q)$ are the potential energy functions of the electrons. The eigenvalue problem is solved by setting up a matrix similar to that in the crystal field problem above. Each element in this matrix is

$$M_{ab} = \sum_r \eta_r \int \psi_a^* V_i(Q) \psi_b d\tau \quad 1.58$$

where the integral will be equal to zero if it does not contain the symmetrical representation A_{1g} .¹⁵ Therefore, if a displacement caused by a normal mode does not contain the completely symmetrical representation, then the symmetrical configuration will not be stable.¹⁵

As shown above, the first order Jahn-Teller effects occur as a result of the orbital overlap and changes in radial motion. The distortion changes the degree of overlap in the bond and therefore causes the central axis to either elongate or contract, thus lowering its symmetry as shown in Figure 1.7. First order distortions are small due to the fact that a large energy barrier must be overcome in order to change the amount of overlap of the wave functions.

Second order Jahn-Teller distortions occur in molecules that have both full and empty orbitals with a small energy gap in between them.¹⁷ The small energy gap allows a mixing of the highest occupied molecular orbital (HOMO) and lowest unoccupied molecular orbital (LUMO).¹⁶ Second order Jahn-Teller can cause much larger distortions than first order and may even cause dissociation.¹⁷ Large distortions are possible because there is a small energy barrier to reach the lowest energy state so it is possible for a large change in angular position to occur with a small change in energy.

1.5 The chemistry of Ag(II)

This section will describe in detail the chemistry of Ag(II) as well as the relationship between silver fluorides and high T_C copper oxides.

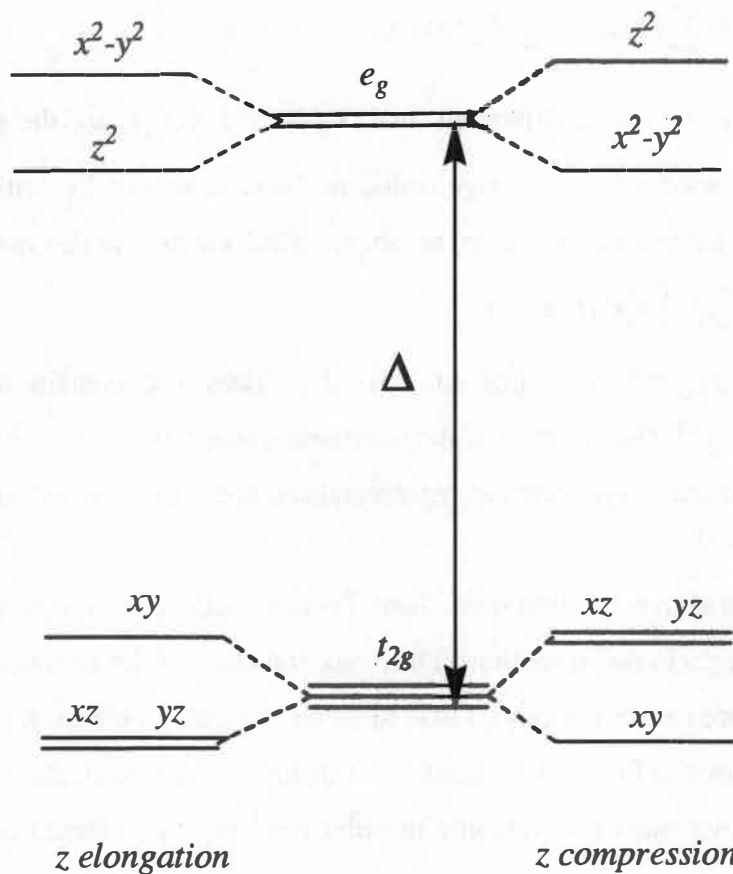


Figure 1.7: Example of Jahn-Teller distortion occurring with the d orbitals of an octahedrally coordinated metal-ligand complex.

1.5.1 Ag(II) compounds and superconductivity

The interest in Ag(II) compounds has grown dramatically in the past few years. The reason for the increase in interest in Ag(II)-containing materials is due to their interesting magnetic behavior including the possibility of high T_C superconductivity.¹⁸ Superconducting materials are those in which resistance drops to zero below a critical temperature, T_C .⁸ High T_C materials possess a critical temperature somewhere between 30K and 120K, which is much higher than normal. The mechanism in which this occurs is currently unknown, but it is most likely not due to the electron-phonon interaction that is typical of a normal superconductor.⁸ The potential for Ag(II) compounds, particularly silver fluorides, to attain superconducting properties stems from their similarity to the well studied copper oxides such as La_2CuO_4 and its doped derivatives.^{19,20}

1.5.2 Properties of Ag(II)

One of the reasons Ag(II) compounds are potential superconductors is because of the similarities between Ag(II) and Cu(II). Both Ag(II) and Cu(II) are d^9 , spin- $1/2$ ions which, for copper, is of the utmost importance because of the antiferromagnetic coupling of these ions in the lattice of the copper oxides. Despite these major similarities between silver(II) and copper(II), their chemical behavior regarding oxidation-state stability is quite different. In chemistry involving copper, different oxidation states include Cu(I), Cu(II), and Cu(III). All are common and well represented, but with silver, most compounds contain ions in the Ag(I) or Ag(III) state.^{18,21,22} The reason why Ag(II) compounds are rare is because Ag(II) is an extremely strong oxidizer and therefore extremely reactive.²³ Ag(II) is such a strong oxidizer that when elemental xenon is in the presence of Ag(II) ions in anhydrous HF solution, Xe is oxidized to form Xe(II).^{24,25}

In order to mimic the copper oxide systems, it would be necessary to produce a material with AgO_2 sheets. However, there is no known compound with these AgO_2 sheets that exist and also AgO is actually found as the mixed-valence complex, $[\text{Ag}^{\text{I}}\text{Ag}^{\text{III}}]\text{O}_2$.²² The only known ligand that stabilizes Ag(II) is fluorine. Several materials containing silver(II) fluoride lattices are known due to the mainly the work of Bartlett,²⁶⁻³¹ Hoppe,³²⁻⁴⁰ Müller,⁴¹⁻⁴⁸ and Ževma.^{25,29-31,49-55} Most of these silver fluorides

appear in a distorted octahedral environment with AgF_2 sheets or AgF^+ infinite chains and occasionally a square planar AgF_4^- ion can be found in these structures.¹⁸ An example of a compound with AgF_2 sheets would be Cs_2AgF_4 and K_2AgF_4 ,³⁸ while materials with AgF^+ infinite chains include $[\text{AgF}]^+[\text{AuF}_4]^-$,²⁶ and $[\text{AgF}]^+[\text{Cd}_3\text{HfF}_{19}]^+$,⁴² and an example of AgF_4 planes is BaAgF_4 .

1.5.3 Oxide/Fluoride analogy

As stated in the above section, the only ligand that is able to stabilize silver in the +2 oxidation state is fluorine. However, that reason alone is not enough to justify using argentic silver fluoride based compounds as a comparison to copper oxides. An important analogy between O^{2-} and F^- must be made as well.

Oxide and fluoride are both small, extremely electronegative ions with high oxidation potentials and both are classified as hard bases.⁵⁶ Table 1.3 shows that the ionic radius, electronegativities, and also the ionization potential of these two ions are very similar. Both oxide and fluoride also have the ability to form hydrogen bonds and indeed form very strong ones in materials such as H_2O ⁵⁷⁻⁶⁰ and HF .^{61,62} The fact that electronic and crystalline radii similarities exist between oxide and fluoride imply that the solid state oxides and fluorides will share similar structure types as shown in Table 1.4.⁶³

1.5.4 Difficulties of Ag(II) synthesis

Although silver (II) fluorides are an excellent start in the search for a new class of high T_C materials analogous to the copper oxides, little is known about these compounds,

Table 1.3: Structural radii and energetics for O^{2-} and F^- .

atom	$r_{\text{ion}}^{\text{a}} / \text{\AA}$	$r_{\text{xx}} / \text{\AA}$	$r_{\text{HX}} / \text{\AA}$	BDE ^b /kJmol ⁻¹	IP ^c /kJmol ⁻¹	EA ^d /kJmol ⁻¹
F	1.17-1.19	1.24-1.28	0.92	154.8	1681	328
O	1.414	1.207	0.96	498.36	1313.9	141 ^e 752 ^f

a) Shannon-Prewitt Radii

b) bond dissociation energy

c) 1st ionization energy

d) 1st electron affinity

e) for $\text{O} + \text{e}^- \rightarrow \text{O}^-$

f) for $\text{O} + 2\text{e}^- \rightarrow \text{O}^{2-}$

Table 1.4: Structures of common oxides and fluorides.

Composition	Coordination Number		Structure type	Examples	
	M	A		F	O
MA ₃	6	2	Rhenium trioxide	ScF ₃	WO ₃
MA ₂	8	4	Fluorite	SmF ₂	ZrO ₂
	6	3	Rutile	MnF ₂	MnF ₂
	4	2	SiO ₂	BeF ₂	GeO ₂
MA	6	6	Rock salt	NaF	MnO

with past structural and magnetic characterizations being sparse or incorrect. Given that they are extremely strong oxidizers which cause them to be highly reactive, their inherent air and water sensitivity present problems and difficulties with synthetic techniques.^{18,38} Stabilizing silver in the +2 oxidation state involves using materials such as elemental fluorine or anhydrous HF as a solvent. This could potentially create safety problems as F₂ spontaneously combusts with most metals and HF is one of the strongest and most corrosive acids known. Also, sample containment is a difficult issue as most of the silver (II) fluoride compounds will corrode any material except 24k gold, quartz, and PTFE. Despite all of these difficulties, the Turner lab at the University of Tennessee is one of the few in the world that is able to properly synthesize and contain these materials.

1.6 Theory of experimental techniques

In studying each silver fluoride, several different experimental techniques were employed to completely characterize each material. X-ray and neutron diffraction measured elastic scattering giving complementary data of the high Z and low Z atomic positions. All X-ray diffraction experiments in this thesis were performed at National Synchrotron Light Center (NSLS) of Brookhaven National Laboratory (BNL) on the X3B1 beam line. All neutron diffraction experiments were performed at the Lujan Neutron Scattering Center of Los Alamos National Laboratory (LANL) on the NPDF beam line. In order to understand the magnetic properties of these materials magnetic susceptibility measurements were done using a Superconducting Quantum Interference Device (SQUID) and inelastic neutron scattering was performed to measure the magnetic excitations of the materials. SQUID measurements were performed using the instrument

at the University of Liverpool and also at the Solid State Division of Oak Ridge National Laboratory (ORNL). And finally, the inelastic neutron scattering experiments were performed at the ISIS pulsed neutron and muon source of Rutherford Appleton Laboratory, on MARI and the High Energy Transfer (HET) beam lines. The following sections will describe each of these four techniques in detail.

1.6.1 Diffraction techniques

Diffraction is a type of scattering where coherently scattered waves interfere with each other and the intensity of these scattered waves are measured as a function of momentum transfer. In diffraction, the scattering is elastic so the incident energy always equals the scattered energy. Materials will diffract when the wavelength of the radiation is on the same length scale as the distribution of scattering density. The intensity of these scattered waves has the form

$$I(Q) = \sum_{\substack{i,j \\ i \neq j}} f_i f_j \exp(iQ \cdot \vec{r}_{ij}) \quad 1.59$$

where f_i and f_j are the scattering factors specific to atom i and j , \vec{r}_{ij} is the vector between atoms i and j and Q is the scattering vector

$$Q = \frac{4\pi \sin \theta}{\lambda} \quad 1.60$$

where θ is the scattering angle and λ is the wavelength of the scattered neutron or photon. Diffraction experiments can be performed using both X-rays and neutrons. The similarities and differences of the two techniques will be described in the following sections.

1.6.2 X-ray diffraction

X-rays possess a wavelength of approximately 1\AA and are a form of electromagnetic radiation generated when electrons are accelerated by a high voltage source. The intensity measured in the experiment is a combination of scattering from the individual atoms and interference between the scattered waves of different atoms. This scattering intensity of X-rays is defined as

$$I = I_0 r_e^2 \frac{1 + \cos^2 \theta}{2} \frac{1}{16\pi \sin^2 \theta \cos \theta} \lambda^3 F_{h,k,l}^2 n \frac{1}{V_c} D dV \quad 1.61$$

where I_0 is the incident beam intensity, r_e is $7.9 \cdot 10^{-26} \text{ cm}^2$, $(1 + \cos^2 \theta)/2$ is the polarization factor, $1/(16\pi \sin^2 \theta \cos \theta)$ is the Lorentz geometry factor, V_c is the volume of the unit cell, D is the Debye Waller factor, and $F_{h,k,l}$ is the structure factor. The structure factor is

$$F_{h,k,l} = \sum_i f_i \exp\{-2\pi i(hx_i + ky_i + lz_i)\} \quad 1.62$$

where f_i is the atomic structure factor

$$f(Q) = \sum_n \int_0^\infty 4\pi r^2 \rho_n(r) \frac{\sin(Qr)}{Qr} dr \quad 1.63$$

where $\sum_n \int_0^\infty 4\pi r^2 \rho_n(r) dr$ is equal to the atomic number. This shows that the amount of scattering from an atom depends on the atomic number and therefore the electron density of an atom. As a result, heavier atoms will scatter much more effectively than lighter atoms and therefore the scattering power increases with atomic number.^{64,65} Also, because the length scale of the distribution of scattering density in the sample is also that of the wavelength of the X-ray, there is a strong angular dependence in the form factor. The form factor, $f(Q)$ is a function of Q and when $Q=0$, the form factor is the same as the atomic number.⁶⁶

1.6.3 Neutron diffraction

Neutron diffraction is complimentary to X-ray diffraction but their measured intensities arise from different physical origins. While X-rays scatter from electron density, neutrons scatter from nuclear density. There is no Coulomb barrier to overcome, so it can be said that neutrons are scattered by nuclear forces.⁶⁷ Neutrons have no charge and little or no electric dipole. The neutron-nucleus interaction produces scattered waves in which the intensity of the scattered waves is measured during the experiment. Neutrons are a genuine bulk probe with wavelengths that are tunable according to the size

scale of the molecule. The scattering centers are point charges, so neutrons can generally travel through most materials without interacting and as a result they usually only scatter weakly when they penetrate.⁶⁴

Unlike X-rays which are sensitive to heavy atoms, neutrons do not discriminate between light or heavy atoms and it can be said that neutrons can be decoupled from the chemical nature of the atom (Figure 1.8). For example, in X-ray diffraction atoms such as hydrogen or fluorine will be virtually transparent to X-ray, but neutrons will scatter strongly from these atoms. Also, the form factors are not angular dependant due to the fact that the neutrons are scattering off of a point charge unlike in X-ray diffraction where the distribution of scattering density is broad over a large range of area.

1.6.4 Powder diffraction and the Rietveld method

In these experiments, diffraction experiments are performed on powder samples. This means that instead of a single crystal, many small crystals of the material are used in the experiments. Polycrystalline materials, like single crystals, consist of a lattice arranged in a periodic manner where the scattering can be predicted by Bragg's law

$$n\lambda = 2d_{h,k,l} \sin \theta \quad 1.64$$

which relates the scattering angle 2θ to the interplanar spacing of the plane, $d_{h,k,l}$, formed by the faces in the sample, thus making it a useful tool for determining the structure of a system.⁶⁴ Unlike single crystal diffraction, in most powder diffraction experiments it is not necessary to worry about the orientation of the crystals because in an experiment, the powder average is taken due to a large number of crystals present in an isotropic orientation.⁶⁵ The h,k,l values contain a distribution of all the differently oriented crystals. This distribution gives the intensity of the Bragg peak as the number of reflections with a defined set of h,k,l values therefore presenting an average structure of the material.

The type of method used to analyze a powder pattern is called the Rietveld method developed by Hugo M. Rietveld.^{68,69} The Rietveld method is a whole-pattern structure refinement which has the ability to extract detailed crystallographic information from powder diffraction data.⁷⁰ A least squares method is used to find the best possible calculated model based on the diffraction pattern.

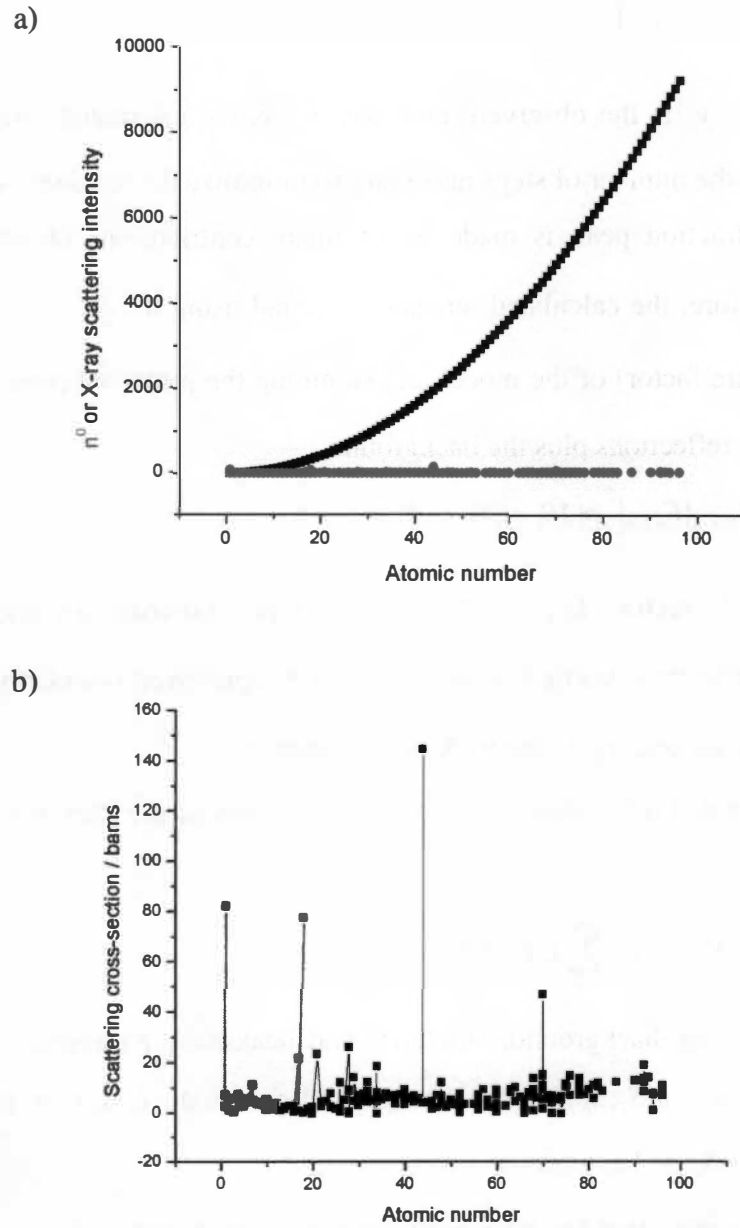


Figure 1.8: a) X-ray scattering intensity as a function of atomic number, b) Neutron scattering cross section as a function of atomic number.

The method aims to minimize the residual between the observed and calculated intensities

$$S_y = \sum_i w_i (y_i - y_{ci}) \quad 1.65$$

where w_i is $1/y_i$, y_i is the observed intensity, y_{ci} is the calculated intensity and the summation is over the number of steps necessary to minimize the residual. Generally, the intensity of a diffraction peak is made up of many contributions of different Bragg reflections. Therefore, the calculated intensity is found using the $|F_{h,k,l}|^2$ values (where $F_{h,k,l}$ is the structure factor) of the model and summing the projected contributions from neighboring Bragg reflections plus the background

$$y_{ci} = s \sum_{h,k,l} L_{h,k,l} |F_{h,k,l}|^2 \phi(2\theta_i - 2\theta_{h,k,l}) P_{h,k,l} A + y_{bi} \quad 1.66$$

where s is the scale factor, $L_{h,k,l}$ contains the Lorentz, polarization, and multiplicity factors, ϕ is the reflection profile function, $P_{h,k,l}$ is the preferred orientation function, A is the absorption factor and y_{bi} is the background intensity.⁷⁰

These calculated intensities are then used as a basis of the Rietveld model which is

$$M(S_i, x) = b(S_i, x_b) + \sum_{k1}^{k2} I_k(x_s) \phi(S_i - S_k, x_p) \quad 1.67$$

Where x_b , x_s , and x_p are background, structure, and peakshape parameters, k represents h, k, l , $S_i = 2 \sin \theta_i / \lambda_i$, $b(S_i, x_b)$ is the background function, $I_k(x_s)$ is the integrated intensity, and $\phi(S_i - S_k, x_p)$ is a profile function.

The model shows that the background must be taken into account in the model. In equation 1.62, the background intensity factors into the calculated intensities and therefore an accurate background fit is essential for obtaining the correct intensities in the model.

Another important aspect of the model is the peak shape, which is described by the profile function. Different experimental techniques and different instrument settings

result in different types of peak shapes.⁷⁰ Many neutron peaks can be fit using a Gaussian function where the probability density of this normal distribution is

$$f(x) = \frac{1}{\sigma\sqrt{2\pi}} \exp\left(-\frac{(x-\mu)^2}{2\sigma^2}\right) \quad 1.68$$

where σ is the standard deviation, μ is the mean, and σ^2 is the variance. Other peaks are best fit using a Lorentzian function

$$f(x) = \frac{\sigma/2\pi}{(x-\mu)^2 + (\sigma/2)^2} \quad 1.69$$

which is sharper and more narrow as shown in Figure 1.9. X-ray peaks generally have a longer tail than a Gaussian which causes the peak to be asymmetric. These peak shapes can be fit with a pseudo-Voigt function which determines the fraction of Gaussian and Lorentzian terms needed to correctly fit the profile

$$f(x) = (1-\eta)\text{Gaussian}(\Gamma) + \eta\text{Lorentzian}(\Gamma) \quad 1.70$$

where η is the mixing parameter and Γ is the FWHM, or full width half maximum of the peak.

When calculating a model based on the observed powder pattern, the extraction of peak intensities is very important due to overlaps that may occur. One common method to do this is by performing a Le Bail extraction. In the Rietveld method, the peak extractions are biased because $|F_{obs}|$ is estimated by a division of the reflections of each profile according to the contributed reflections based on $|F_{calc}|$.⁷¹ However, in the Le Bail method, the overlapping peak profiles are extracted through an iterative process where the $|F_{calc}|$ value of the current step becomes $|F_{obs}|$ of the next iteration.^{72,73} This process allows $|F_{calc}|$ to converge to a set of reflections as close to the actual pattern as possible. The initial $|F_{calc}|$ can either be computed from the model of the crystal structure, or if no good model is known, then it can be assumed that all the reflections are equally likely to contain intensity so if two or more reflections overlap, then each begins with the same calculated intensity.⁷¹

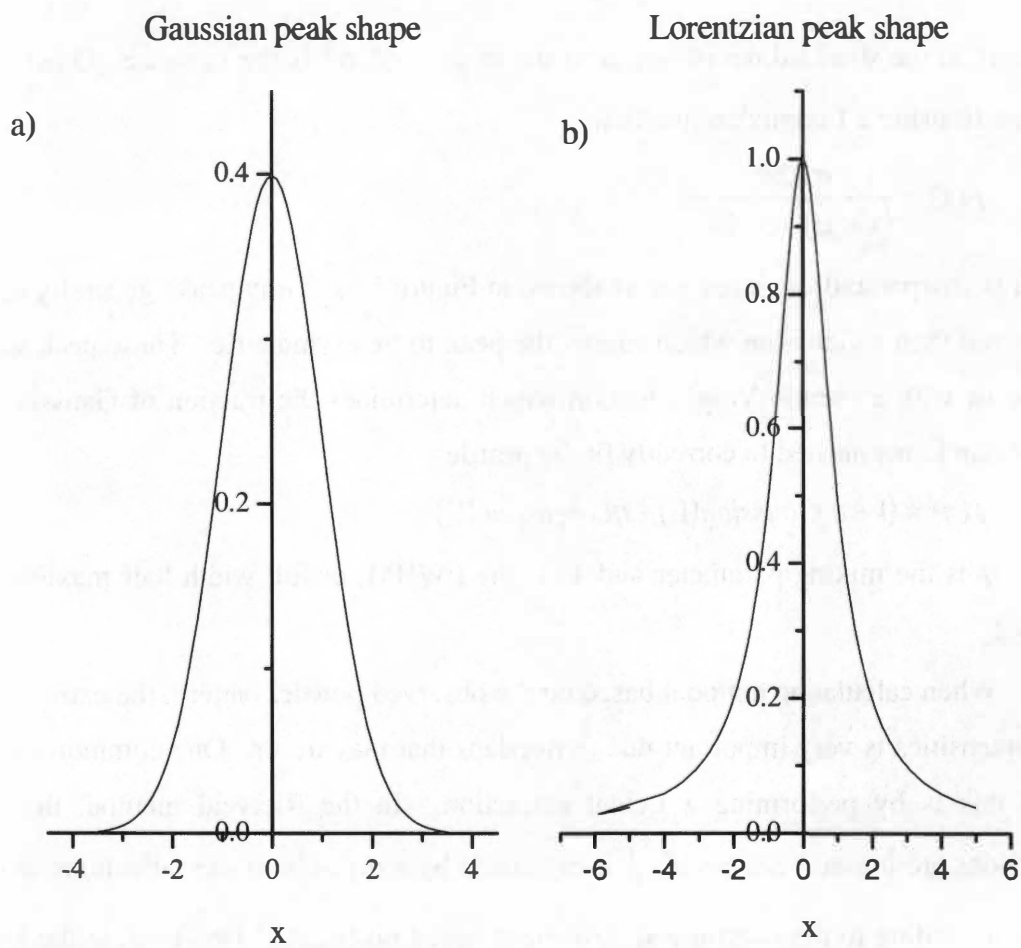


Figure 1.9: Gaussian peak shape versus the Lorentzian peak shape with $\mu = 0$ and $\sigma = 1$.

When using the Le Bail peak extraction method, it is also possible to refine model independent parameters such as background, lattice parameters, peak profile functions, as well as the wavelength and other instrument related parameters. Once the intensities have been extracted, then the Rietveld method can then be used to refine the model dependent parameters such as atomic position, thermal parameters, and occupancy.

1.6.5 Inelastic neutron scattering

Inelastic scattering is extremely useful in probing the dynamics of a system. In inelastic scattering, constant incident energy is used to probe the material at different Q vectors. The energy excitations can be measured because unlike diffraction, the incident energy does not equal the scattered energy as both momentum and energy can be transferred to or from the sample as shown in Figure 1.10.

In an inelastic neutron scattering experiment, the energy and momentum change from the neutron to the sample is measured where

$$S(\mathbf{Q}, E) = \frac{1}{2\pi\hbar} \int G(\mathbf{r}, t) \exp[i(\mathbf{Q}\mathbf{r} - \alpha t)] d\mathbf{r} dt \quad 1.71$$

is called the scattering function.⁶⁷ The Fourier transform of the scattering function is

$$G(\mathbf{r}, t) = \frac{\hbar}{(2\pi)^3} \int S(\mathbf{Q}, E) \exp[-i(\mathbf{Q}\mathbf{r} - \alpha t)] d\mathbf{Q} dt \quad 1.72$$

and is known as the time dependent pair-correlation function.

Although inelastic scattering can be used for many different purposes, in this work it is used to determine the magnetic excitations of a material and allows for a time dependent study of spin correlations in the scattering system.⁶⁷ Neutrons possess a magnetic moment

$$\mu_n = -1.913\mu_N \quad 1.73$$

which can interact with the magnetic moment of various materials and neutrons are scattered as a result of the interaction.⁶⁷

In these experiments, it is possible to determine the amount of energy gained or lost when the magnetic excitations occur by the time in which the scattered neutrons reach the detector. The low lying magnetic modes can be investigated to determine the

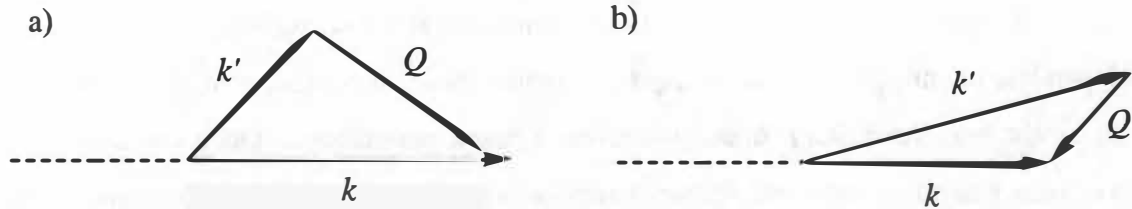


Figure 1.10: Change in wavevector when a) energy is lost and b) when energy is gained.

magnetic Hamiltonian. This type of neutron scattering is used to establish the energy scale and dispersion relations of the magnetic excitations.

1.6.6 Bulk susceptibility measurements

A superconducting quantum interference device, or SQUID, is used to determine the magnetic susceptibility of a material over a range of temperatures. A magnetic dipole produces a field of the order

$$B = \frac{M}{d^3} \quad 1.74$$

where M is the dipole moment and d is the distance of the point on the field from the center of the dipole.⁴ The SQUID method is able to fix d , measuring the field which leads to the dipole moment and therefore its magnetization or susceptibility.⁴

The instrument is composed of two superconducting rings that are separated by thin insulating layers which form parallel Josephson junctions in which electrons can tunnel through.⁸ The tunneling occurs at a insulating barrier of the superconducting current where current passes through without any resistance. Electrons are able to move through the barrier and in turn, continue the superconducting effect.

A SQUID is an extremely sensitive device that can measure the change in a magnetic field associated with one quantum flux. The magnetic flux induces a current density across the junction

$$j = \frac{2\pi}{\Phi_0} C |\psi_1 \psi_2| \sin(\theta_1 - \theta_2) + \frac{2\pi\Phi(y)}{\Phi_0} \quad 1.75$$

where the wave function is a function of r with the square of the wave function being the probability of finding the electron at distance r , and Φ_0 is the magnetic flux.⁸ The SQUID maintains a constant current and the voltage oscillates with a change in phase at

the junction which depends on the magnetic flux. By counting the oscillations, the magnetometer can determine any change that occurs in the magnetic flux.

2 Experimental

2.1 Synthesis

Cs_2AgF_4 was synthesized using the starting materials AgF_2 (98%) and CsF (99.9%) which were purchased from Strem Chemicals. For each synthesis, 0.01212 mols of AgF_2 and 0.02424 mols of CsF were combined and ground using an agate mortar and pestle until a homogeneous mixture was achieved.

$\text{Cs}_{1.9}\text{Ba}_{0.1}\text{AgF}_4$ was synthesized using AgF_2 , CsF , and BaF_2 (99.0%). For this synthesis, 0.009059 mols of AgF_2 , 0.01721 mols of CsF , and 0.0009057 mols of BaF_2 were mixed together and ground as above in an agate mortar and pestle until a uniform mixture was present.

Both of the above syntheses used the following procedure to achieve the final product. The preparation procedures were performed in a dry glove box under an inert nitrogen atmosphere. The mixed powder was transferred to a 24 karat gold tube with a height of 9 cm and an inner diameter of 1.5 cm. The gold tube was placed in a Schlenk flask and transferred to a furnace and heated to 270°C for 24 hours with an argon flow through the flask. The resultant material from both reactions was a fine powder that was lilac in color. The compounds were vacuum sealed in flame dried quartz tubing using a high vacuum line and stored in a nitrogen atmosphere glove box. A Bruker AXS Smart 1000 diffractometer with a Mo-K_α monochromator was then used to check the purity of the sample using the lattice parameters previously published.³⁸

2.2 X-ray diffraction

X-ray diffraction measurements were performed at NSLS of Brookhaven National Laboratory on the X3B1 beam line. Approximately 20 mg of the sample was ground up and transferred into a quartz capillary tube with a 0.3 mm diameter under nitrogen atmosphere. The capillaries were then flame sealed under vacuum to form an airtight container.

In X3B1, the X-rays pass through a monochromator enclosed in a helium atmosphere with parallel $\text{Si}(111)$ crystals, then 2mm x 8mm collimating slits, an ionization chamber monitor for the incident flux, then strike the sample which was

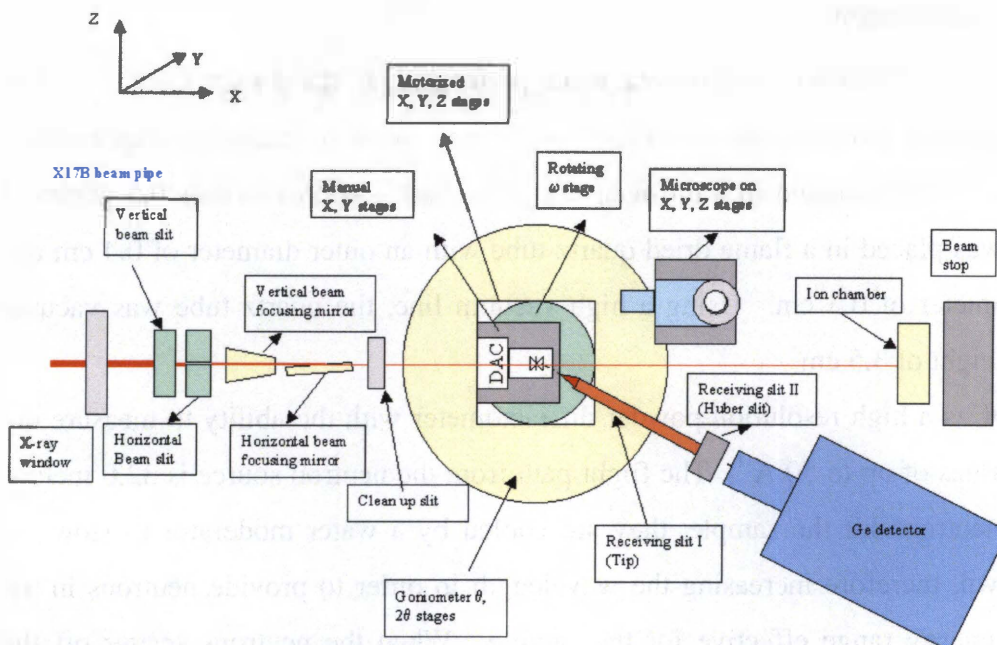


Figure 2.1: Schematic drawing similar to the X3B1 X-ray diffractometer.

mounted on a rotating stage. The diffracted X-rays pass through another set of slits which strike the Ge(111) analyzer crystal which diffracts the beam into a NaI scintillation counter. Figure 2.1 shows a schematic of the set up of the X3B1 diffractometer.

The diffractometer was calibrated using Al_2O_3 to calculate the wavelength which was 0.6994 \AA . Data sets were obtained for temperatures of 300K and 12K from 2θ values of 5° to 40° in steps of 0.003° with a counting time of 2 seconds.

2.2.1 Rietveld refinements

Rietveld refinements were performed on the data using the GSAS package.^{70,71} The first step in these refinements was to execute a Le Bail extraction on the model independent parameters. This method was used to refine the background (manual background fitting was performed), lattice parameters, wavelength, and the peak profile. The peak profile used for X3B1 was type 3 which is a pseudo-Voigt function and mixes Gaussian and Lorentzian terms. Next, the Rietveld method was used to refine the model dependant parameters such as atom position, thermal parameters, and atomic occupancy, being careful not to refine the occupancy and thermal parameters at the same time.

2.3 Neutron diffraction

Neutron diffraction experiments were performed at the Lujan Center of Los Alamos National Laboratory on the NPDF beam line. As with the X-ray experiments, these samples were prepared in a nitrogen dry glove box. Approximately 0.5 grams of the sample was placed in a flame dried quartz tube with an outer diameter of 0.4 cm and an inner diameter of 0.3 cm. Using a high vacuum line, the quartz tube was vacuum sealed at a height of 3.5 cm.

NPDF is a high resolution powder diffractometer with the ability to measure out to high Q values of up to 50 \AA^{-1} . The flight path from the neutron source is 32.0 meters. Before the neutrons hit the sample, they are cooled by a water moderator to slow the neutrons down, therefore increasing the wavelength in order to provide neutrons in the appropriate energy range effective for the sample. When the neutrons scatter off the sample, they are counted by detector banks at 90° , 119° , and 148° . The detector banks are composed of 20 panels with 160 smaller individual detectors (Figure 2.2).

The sealed quartz samples were placed in a vanadium can approximately 4 cm in height with an inner radius of 0.586 cm and an outer radius of 0.632 cm under a helium atmosphere. The vanadium can was attached to a metal conducting rod that controls the temperature and was placed under vacuum in the helium cryostat of the instrument. Data was taken at 300K and at 6K with a counting time of 12 hours for each temperature, which was necessary due to the high absorption cross section (63.3 barns) of silver. Empty quartz tubes in the vanadium can were also measured in order to perform a background subtraction.

2.3.1 Background Subtraction

All of the diffraction data was corrected for background scattering, incident neutron flux, multiple scattering, and absorption effects using the PDFgetN software program.⁷⁴ This program was also used to perform the background subtraction and correct absorbance problem at low Q . Background subtraction for Cs_2AgF_4 is not typical. Because of the air sensitivity of the sample, both the vanadium can and the quartz can must be subtracted off of the data. Quartz is an amorphous material and leaves an

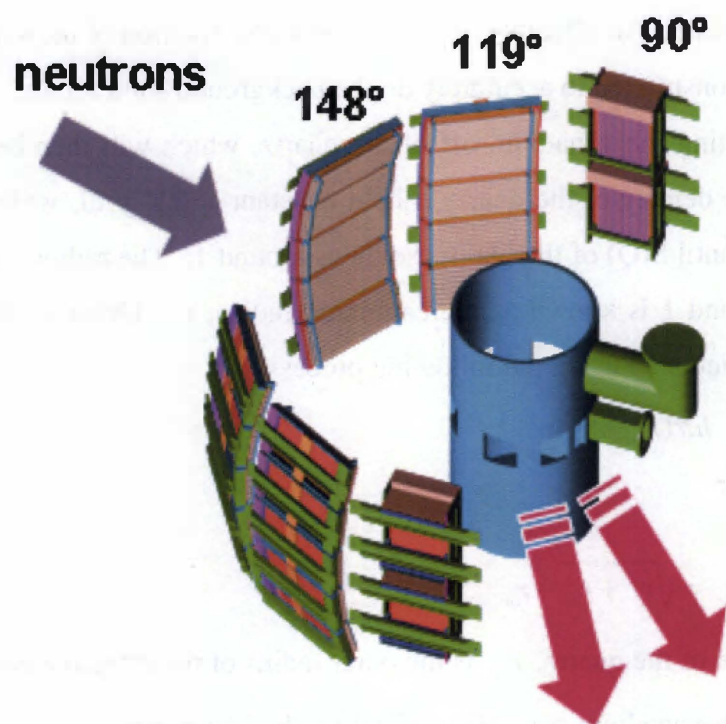


Figure 2.2: Simple schematic of interior of NPDF.

obvious pattern in the data (Figure 2.3a). In order to do this appropriately and consistently with each sample, a new method was developed. First it was necessary to analyze the blank that was run and subtract off the vanadium from the quartz to ultimately find the effective radius of the sample in the beam. Of all the variables in PDFgetN, the two that affect the absorbance are the density of the sample and the radius of the sample in the beam. An effective can, which is a combination of the vanadium and quartz cans must be constructed to accurately do the background subtraction.

When subtracting the vanadium off of the quartz, which will then be subtracted off of the sample, the density of the quartz is held constant at 2.2 g/mL while the radius of the sample varies until $S(Q)$ of the blank oscillates around 1. The radius which allows $S(Q)$ to oscillate around 1 is known as the calibrated radius, r_c . Using r_c , the effective thickness, d_{eff} , was calculated using the following process

$$V_{SiO_2} = h\pi r_c^2 = h\pi(r_{out}^2 - r_{in}^2) \quad 2.1$$

$$r_{out} = \sqrt{r_{in}^2 + r_c^2} \quad 2.2$$

$$d_{SiO_2} = r_{out} - r_{in} = \sqrt{r_c^2 + r_{in}^2} - r_{in} \quad 2.3$$

where V is the volume of the quartz, r_{out} is the outer radius of the effective can, and r_{in} is the inner radius of the vanadium can. This effective thickness, however, only accounts for the thickness of the quartz, so the thickness of the vanadium must be taken into account

$$d_{eff} = d_{SiO_2} + d_v \quad 2.4$$

where d_{eff} is the total effective thickness, d_{SiO_2} is the effective thickness of quartz, and d_v is the thickness of the vanadium can.

The next step of the background subtraction was to calculate the number density, scattering cross section, and absorbance cross section of the effective can. First, the volume of the quartz and vanadium was calculated using the following formulas

$$V_{SiO_2} = h\pi r_c^2 \quad 2.5$$

$$V_v = h\pi(r_{out}^2 - r_{in}^2) \quad 2.6$$

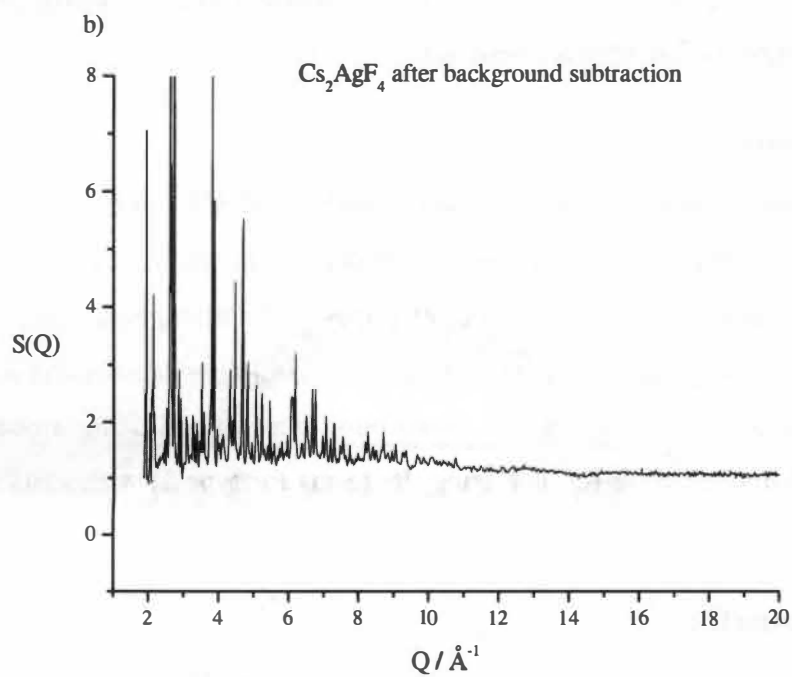
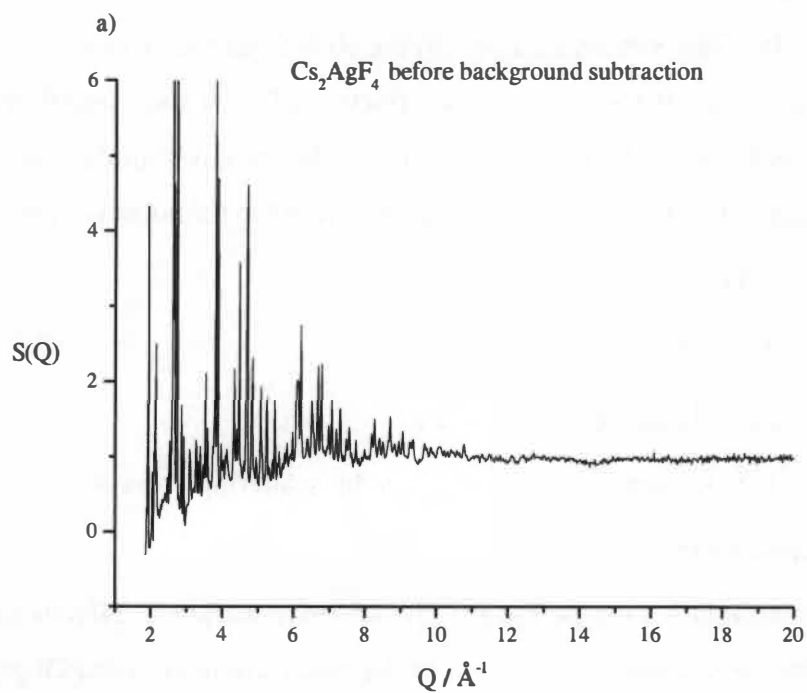


Figure 2.3: a) Cs_2AgF_4 before background subtraction and absorbance correction. Note the amorphous quartz peaks and the absorbance at low Q values. b) Cs_2AgF_4 after background subtraction and absorbance correction.

where r_c is the calibrated radius, and r_{out} and r_{in} are the outer and inner radius of the vanadium can, respectively. The number of atoms in the above volumes was then found by multiplying the density times the volume and the fraction of each atom found in the quartz and vanadium together was calculated. To calculate the effective number density, scattering cross section, and absorbance cross section, the following formulas were used

$$\rho_{eff} = \rho_{SiO_2} \cdot \chi_{SiO_2} + \rho_v \cdot \chi_v \quad 2.7$$

$$\sigma_{eff\ abs} = \sigma_{SiO_2\ abs} \cdot \chi_{SiO_2} + \sigma_{v\ abs} \cdot \chi_v \quad 2.8$$

$$\sigma_{eff\ scatt} = \sigma_{Si\ scatt} \cdot \chi_{Si} + \sigma_{O\ scatt} \cdot \chi_O + \sigma_{v\ scatt} \cdot \chi_v \quad 2.9$$

where ρ is the density, χ is the mol fraction, σ_{scatt} is the scattering cross section, and σ_{abs} is the absorbance cross section.

Once all these calculations were performed, the effective thickness, effective can density, and effective absorbance and cross section of the can, were input into PDFgetN. An initial estimate was made for the effective density of the sample. The density of the sample was changed until $S(Q)$ of the sample oscillated around 1 (Figure 2.5b). The resulting $S(Q)$ was then used for Rietveld refinements.

2.3.2 Rietveld refinements

A Rietveld refinement was performed using GSAS as it was with the X-ray diffraction data. However, the neutron experiment generated a data set for each detector back at the three different angles. In order for the refinements to converge properly, the model was refined for one histogram at a time, then, at the end, all three histograms were refined together. For the Le Bail extraction, the background was refined using a power series and the profile parameters were refined using the terms for type 1, which fits the peak shape to Gaussians.

2.4 Inelastic neutron scattering

Measurements were performed on the High Energy Transfer (HET) time of flight spectrometer at the ISIS pulsed neutron source of Rutherford Appleton Laboratory, UK. The neutron scattering cells were loaded in a nitrogen atmosphere glove box to ensure

maximum purity. The samples were contained in a prefluorinated Teflon sheet with dimensions 5cm x 5cm x 0.01mm before placing it in a very thin aluminum sample plate 3mm in width. The thin aluminum plate is necessary to reduce the absorbance effects of a highly absorbing silver sample and the Teflon is used to prevent any corrosion through the aluminum plate.

HET is a direct geometry spectrometer with large angular ^3He detector coverage. This coverage spans the scattering angles $\varphi = 3^\circ - 7^\circ$ (4m) and $\varphi = 9^\circ - 29^\circ$ (2.5m) in two separate banks. The sample was mounted on a 3-stage displex cryostat where a base temperature of 8K was reached. Incident energies were monochromated with a Fermi chopper and the optimal settings for this chopper were with incident energies of 100 meV and 50 meV. The setting using $E_i=100$ meV (400 Hz) gave an energy resolution of 3.9 meV full-width-half-maximum (FWHM) while the $E_i=50$ meV (300 Hz) gave a resolution of 1.9 meV FWHM. Samples were run with incident energies of 100 meV and 50 meV at temperatures of 35K, and 8K for 10 hours which is approximately 1700 μA hours of integrated proton current.

Empty cells were run at the same temperatures because the background affects the low Q region which was analyzed for magnetism. By running the empty cell, it was found that PTFE elastically scatters very strongly at 1.3\AA^{-1} and extends into the low vector region crucial to the magnetic scattering. The elastic line is also affected by absorbance from the sample. The intensity decreased by approximately 20% when the sample was present due to these effects. Therefore, the elastic peak was scaled appropriately when subtracting the background.

2.5 Susceptibility measurements

SQUID magnetometry was used for the susceptibility measurements which were performed at both the University of Liverpool and Oak Ridge National Laboratory. In a dry, nitrogen atmosphere glove box, approximately 100 mg of the sample was loaded into PTFE sample holders which had been previously fluorinated to clean the cell.

Measurements were applied under a weak applied field of 100 Oe for a range of temperatures from 300-2K.

To perform the background subtraction, it was necessary to take into account that the diamagnetic signal of the Teflon was greater than the paramagnetic signal of the sample at higher temperatures. The Teflon was subtracted directly from the sample with an additional constant present to account for scaling of the background and also any diamagnetic signal. To obtain the constant, data from approximately two times the ordering temperature to a reliable temperature where the signal was still with little or no diamagnetic contribution was fit, adjusting the constant until Curie-Weiss behavior was obtained for the corrected signal in the paramagnetic phase.

3 Structural and magnetic characterization of Cs₂AgF₄

This chapter presents the magnetic and structural characterization of Cs₂AgF₄ using X-ray and neutron diffraction, inelastic scattering, and magnetic susceptibility measurements. The inelastic experiment was performed by S. McLain and susceptibility measurements were taken by both D.A. Tennant and B.C. Sales.

3.1 Introduction

Cs₂AgF₄ was chosen for this study because of its obvious structural and possible magnetic similarities to La₂CuO₄ based on the Cu^{II}/Ag^{II} and O²⁻/F⁻ analogies discussed in Chapter 1. La₂CuO₄, which is very similar in structure to K₂NiF₄, is a precursor to the high T_C materials, and superconducts when doped with a small percentage of strontium or barium.^{19,75-79} The K₂NiF₄ structure type is a body centered tetragonal unit cell with a space group of *I4/mmm* and is classified as an *n*=1 member of a Ruddlesden-Popper series.^{80,81} The Ruddlesden-Popper series has the formula A_{*n*+1}B_{*n*}X_{3*n*+1}, where the *n*=1 unit cell structure consists of one layer of perovskite material, ABX₃, stacked between rock salt layers of AX and the subscript is the number of stacked perovskite layers in the unit cell (Figure 3.1).^{82,83} La₂CuO₄ shares this structure type, but has a small distortion; the CuO₆ octahedra are slightly tilted which leads to an orthorhombic lattice. La₂CuO₄ is a Mott insulator and 2D Heisenberg antiferromagnet with a strong magnetic coupling constant of $J \approx 120$ meV, which indicates a strong magnetic correlation between the electron spins. Its antiferromagnetic nature is thought to derive from superexchange, due to oxygen *p* orbitals bridging the Cu *d* orbitals in the CuO₂ planes.

3.1.1 Previous studies of Cs₂AgF₄

Studies performed by R. Hoppe show measurements of the susceptibility of Cs₂AgF₄ at a small number of temperatures. This data can be accurately described by the 10th order high temperature series for the susceptibility of a 2D Heisenberg ferromagnet given by Baker et al (Figure 3.2).⁸⁴ The resulting magnetic coupling is $J=-4.8$ meV. The small coupling constant indicates that the cooperative magnetism displayed by this material is extremely weak. Hoppe's measurements show typical Curie-Weiss behavior at high temperatures, with an ordering temperature T_C of approximately 20K, making this

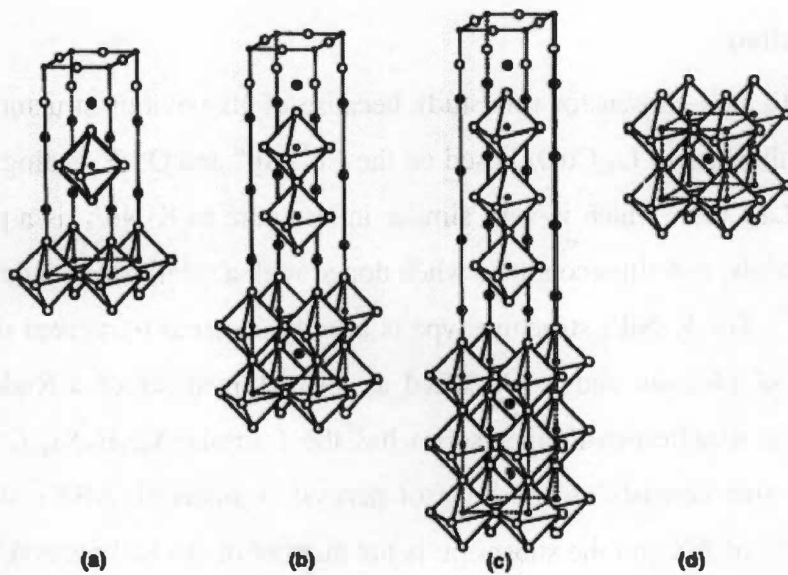


Figure 3.1: Perovskite stacking scheme for the a) $n=1$, b) $n=2$, and c) $n=3$ Ruddlesden-Popper phases. A perovskite unit cell can be seen in d).⁸²

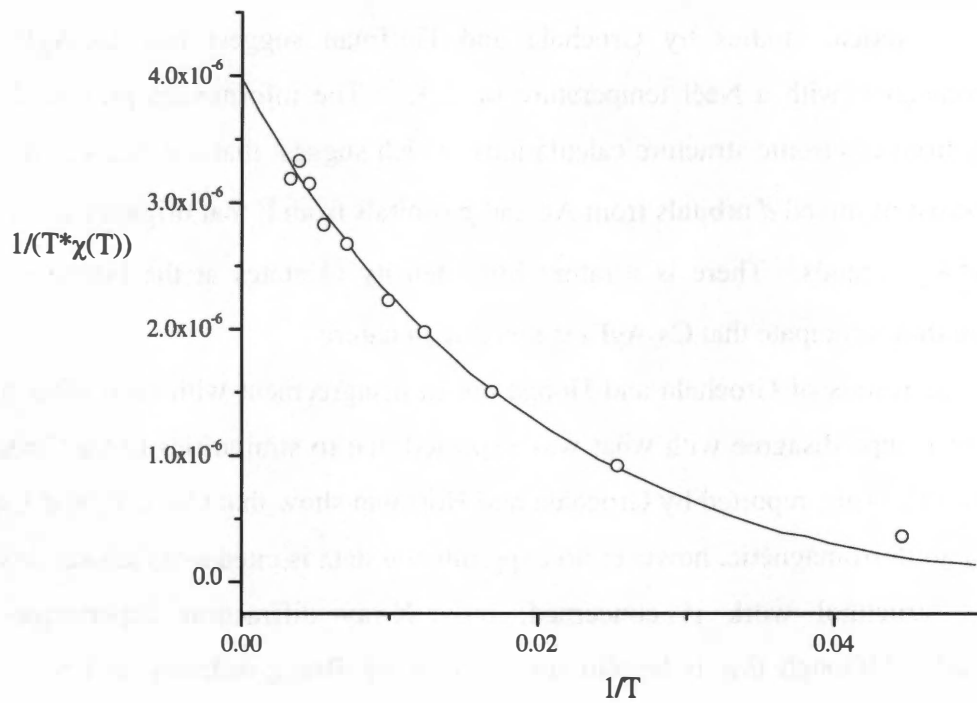


Figure 3.2: Susceptibility data of Hoppe fit to a 10th order 2D Heisenberg ferromagnet with paramagnetic behavior above T_C .⁸⁴⁻⁸⁶

one of the few known 2D Heisenberg ferromagnetic insulators.

Hoppe also performed a structural investigation of Cs_2AgF_4 using X-ray diffraction.³⁸ It was found that this material crystallizes in the $I4/mmm$ tetragonal space group, with lattice parameters of $a = b = 4.58 \text{ \AA}$ and $c = 14.19 \text{ \AA}$. This structure is in the classic K_2NiF_4 family, as described above along with La_2CuO_4 .

Theoretical studies by Grochala and Hoffman suggest that Cs_2AgF_4 is an antiferromagnet, with a Néel temperature of 20K.¹⁸ The information presented in this paper is from electronic structure calculations, which suggest that the states at the Fermi level consist of mixed d orbitals from Ag and p orbitals from F that originate from the z^2 and $x^2 - y^2$ bands. There is a rather high density of states at the Fermi level and therefore they anticipate that Cs_2AgF_4 is metallic in nature.

The results of Grochala and Hoppe are in disagreement with each other and the results of Hoppe disagree with what was expected due to similarities to La_2CuO_4 . The studies on Cs_2AgF_4 reported by Grochala and Hoffman show that Cs_2AgF_4 and La_2CuO_4 are both antiferromagnetic, however no experimental data is cited as evidence. As far as Hoppe's structural work is concerned, only X-ray diffraction experiments were performed. Although this is helpful for determining Bragg ordering and heavy atom positions, it is not as useful as neutron diffraction in establishing the fluorine positions. Regarding the studies of magnetic behavior, the bulk susceptibility can determine the qualitative magnetic properties, but with the remarkable progress made with neutron scattering instrumentation, inelastic scattering can provide data on magnetic excitations which improve on the bulk susceptibility measurements. Inelastic neutron scattering is a local probe, which can be used to characterize the spin-spin interaction between the atoms in the lattice. The work presented in this chapter uses X-ray and neutron diffraction, inelastic neutron scattering and susceptibility measurements to quantitatively establish the nature of the magnetic interactions in Cs_2AgF_4 .

3.2 Data and results

3.2.1 X-ray diffraction

Rietveld analysis was performed on the X-ray diffraction data, as described in Chapter 2. First, the room temperature data was fit assuming an $I4/mmm$ space group. The refined lattice parameters are $a = b = 4.5845(13)$ Å and $c = 14.2062(7)$ Å. This structure consists of a distorted octahedral (4+2) Ag metal center, with Ag-F bond lengths of $2.29266(6)$ Å and $2.21072(11)$ Å. The material has AgF_2 square planar sheets on the top, bottom, and center of the unit cell, with two CsF sheets between the AgF_2 layers. The Cs-F bond in the Cs-F square planar sheets is $3.24625(9)$ Å and the Ag-F nearest neighbor distance in the AgF_2 sheets is $2.29226(6)$ Å. Table 3.1 gives a complete set of the bond lengths, and Table 3.2 gives the anisotropic displacement parameters (ADPs) obtained from the refinement. The average atomic positions can be determined in diffraction measurements, but the atom moves around this position due to thermal vibrations. These thermal vibrations can be represented by

$$B = 8\pi^2 \langle \mathbf{u}^2 \rangle \quad 3.1$$

where $\langle \mathbf{u} \rangle$ is the average thermal displacement. Each component of $\langle \mathbf{u} \rangle$ is defined as an anisotropic displacement parameter, or ADP. The atomic positions together with the ADP of each atom can be used to make a representation, or “ORTEP”, of the unit cell, as seen in Figure 3.3. The Rietveld refinement is shown in Figure 3.4.

The valence bond sum, which is defined as the average oxidation state, of the Ag^{2+} ion in the octahedron is 1.670, using parameters from the refinement. This sum is calculated using the expression

$$V_i = \sum_{j=1}^N \exp\left(\frac{R_1 - R_{ij}}{b}\right) \quad 3.2$$

where V_i is the valence of atom i , R_{ij} is the bond length between atom i and atom j , and R_1 and b are empirically determined parameters.⁸⁷ The value of the parameter b is 0.37 Å and R_1 is dependent on the components of the bond.⁸⁸

Cs_2AgF_4 was refined assuming the presence of three phases because impurities of

Table 3.1: Bond lengths from *I4/mmm* room temperature X-ray refinements for Cs₂AgF₄.

Bond	Length/ Å
Ag – Cs	3.82009(9)
Ag – F(1)	2.21072(11)
Ag – F(2)	2.29226(6)
Cs – Cs	4.58452(7)
Cs – F(1)	2.84760(15)
	3.24625(9)
	3.06841(8)
Cs – F(2)	3.06902(6)

Table 3.2: ADPs from the room temperature X-ray *I4/mmm* refinement.

$U_{ij} \cdot 100$						
Atom	U ₁₁	U ₂₂	U ₃₃	U ₁₂	U ₁₃	U ₂₃
Ag	7.00	7.00	11.52	0.0	0.0	0.0
Cs	4.98	4.98	10.78	0.0	0.0	0.0
F1	7.97	7.97	5.00	0.0	0.0	0.0
F2	5.01	16.99	2.53	0.0	0.0	0.0

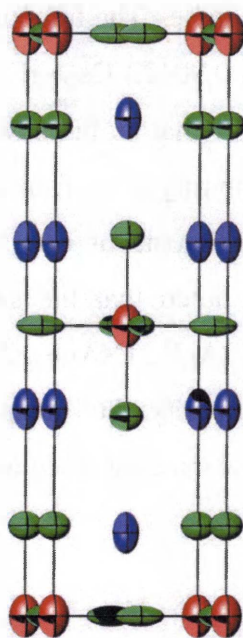


Figure 3.3: Ortep of Cs_2AgF_4 from the room temperature X-ray $I4/mmm$ refinements. The red atoms are silver, blue atoms are cesium, and the green atoms are fluorine.

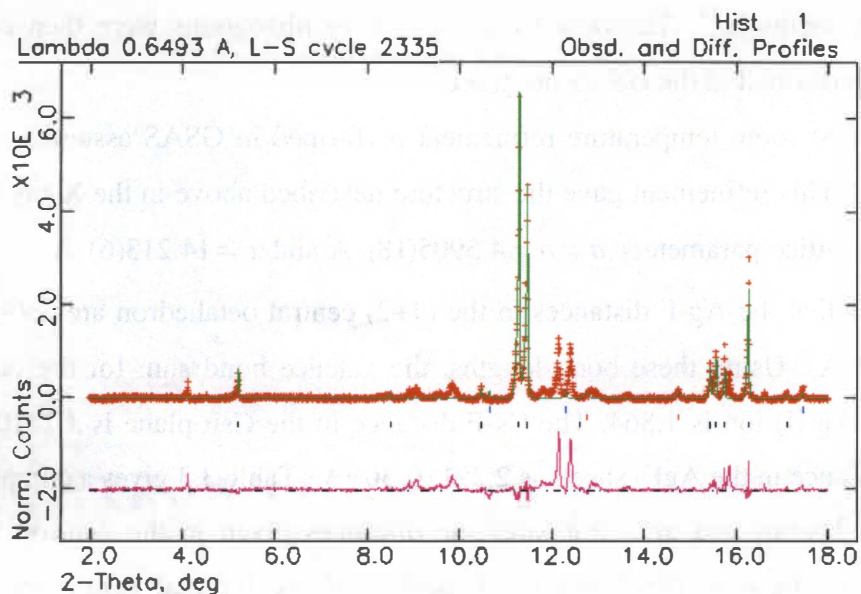


Figure 3.4: Three phase Cs_2AgF_4 Rietveld refinement for $I4/mmm$ space group at room temperature. The black tick marks represent Cs_2AgF_4 peaks, the red represent AgF , and the blue tick marks represent CsF . The red crosses indicate the data while the green lines represent the model. The purple pattern at the bottom represents the residual between the model and the data.

AgF and CsF were present in the sample. The fraction of each phase present (determined by the fitting routine in GSAS) is 0.90122 Cs₂AgF₄, 0.05637 AgF, and 0.045739 CsF. However, the refinements also show that an unknown phase is present (Figure 3.4). It was originally assumed that this impurity arose from prefluorinated starting products, but on running X-ray diffraction experiments of one sample with prefluorinated starting product and one without, it was noted that the same impurity was present in both samples. Several phases such as CsAgF₃, CsAgF₄, Ag₂O, and AgO were added into the refinement to account for the impurity, but none fit the observed peak positions. Therefore, the phase could be a new material, such as a higher order Ruddlesden-Popper phase.

3.2.2 Neutron diffraction

The neutron structure factor $S(Q)$, for the room temperature Cs₂AgF₄ neutron data is shown in Figure 3.5. These structure factors were corrected for absorption and background subtracted using PDFgetN, according to the method developed in the experimental methods.⁷⁴ The data from these three histograms were then used in the refinement performed in the GSAS program.⁷¹

The first room temperature refinement performed in GSAS assumed an $I4/mmm$ space group. This refinement gave the structure described above in the X-ray diffraction results, with lattice parameters $a = b = 4.5905(18)$ Å and $c = 14.213(6)$ Å. The neutron data suggests that the Ag-F distances in the (4+2) central octahedron are 2.29110(30) Å and 2.11413 Å. Using these bond lengths, the valence bond sum for the octahedrally coordinated Ag(II) ion is 1.864. The Cs-F distance in the CsF plane is 3.2410(4) Å and the Ag-F distance in the AgF₂ sheets is 2.29110(30) Å. Table 3.3 gives a complete listing of the bond lengths and also compares the distances given in the neutron diffraction refinements to those in the X-ray refinements and the thermal parameters from the neutron refinements are given in table 3.4.

This data was also fit using a 3 phase refinements with CsF and AgF as impurities with fitted percentages of 0.097% and 2.5% respectively. The fact that AgF is one of the impurity phases instead of the starting product of AgF₂ suggests that during the reaction

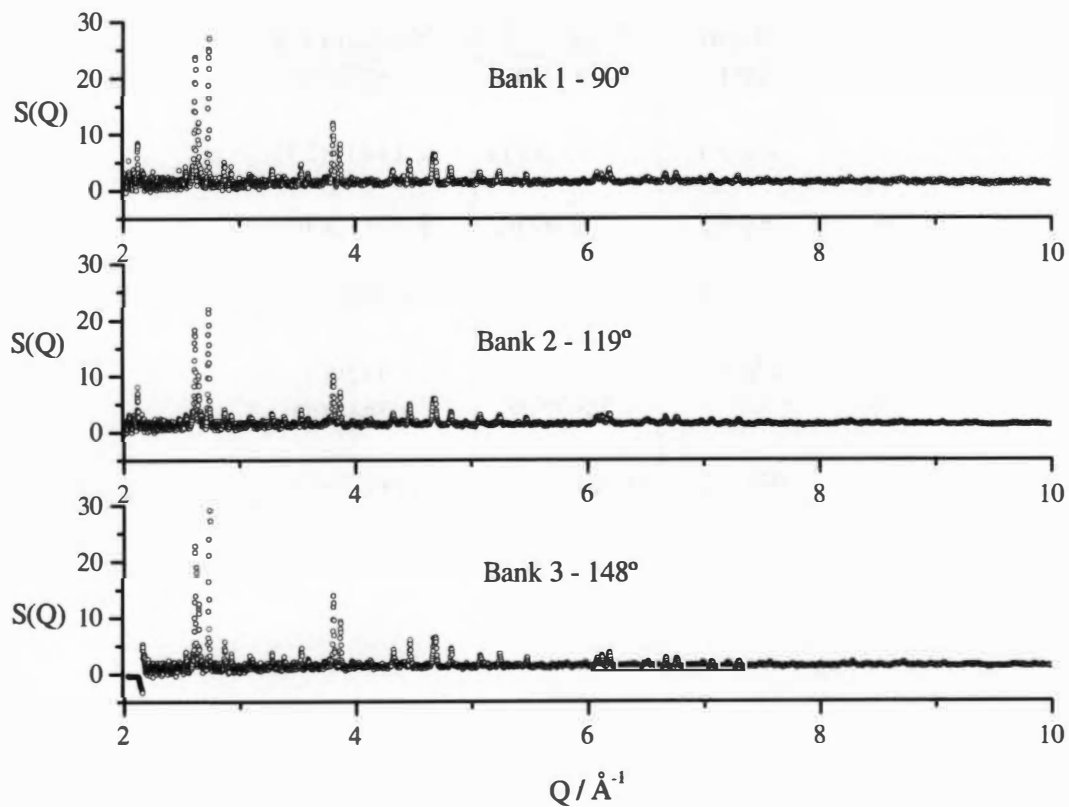


Figure 3.5: $S(Q)$ of Cs_2AgF_4 factor for the three detector banks of NPDF. The data extends out to around Q values of 40\AA^{-1} depending on the bank, but the data is only shown up to $Q=10 \text{\AA}^{-1}$ to better see the scattering at low Q .

Table 3.3: Comparison of the bond lengths from the X-ray vs. the neutron diffraction *I4/mmm* GSAS refinements.

Bond	X-ray / Å	Neutron / Å
Ag-Cs	3.82009(9)	3.8278(4)
Ag-F1	2.21072(11)	2.11413(27)
Ag-F2	2.29226(6)	2.29110(30)
Cs-Cs	4.58452(7)	4.5822(6)
Cs-F1	2.84760(15)	2.9429(4)
	3.24625(9)	3.2410(4)
Cs-F2	3.06841(8)	3.06636(9)

Table 3.4: Thermal parameters from the room temperature neutron *I4/mmm* refinement.

$U_{ij} \cdot 100$						
Atom	U₁₁	U₂₂	U₃₃	U₁₂	U₁₃	U₂₃
Ag	1.46	1.46	0.97	0.0	0.0	0.0
Cs	1.93	1.93	1.84	0.0	0.0	0.0
F1	2.91	2.91	1.00	0.0	0.0	0.0
F2	2.76	7.65	2.35	0.0	0.0	0.0

AgF₂ decomposes to AgF, releasing a small amount of F₂ gas. The unknown phase was not visible in the neutron data. The ortep which includes the thermal parameters is shown in Figure 3.6, and the full three phase refinement, giving $\chi^2 = 1.330$, is shown in Figure 3.7.

Room temperature refinements were also performed on the data assuming a *Bbcm* space group. This space group has orthorhombic symmetry, and should have the approximate lattice parameters of $a_{Bbcm} = \sqrt{2}a_{I4/mmm}$, $b_{Bbcm} = \sqrt{2}b_{I4/mmm}$, and $c_{Bbcm} = c_{I4/mmm}$ in relation to *I4/mmm*. The difference between the *I4/mmm* and *Bbcm* space groups here is that the fluorine positions in *I4/mmm* are symmetrical, while in *Bbcm*, the equatorial fluorines in the AgF₆ octahedron are slightly distorted, as shown in Figure 3.8. Lattice parameters from the refinement were $a = 6.4764(4)$ Å, $b = 6.4807(4)$ Å, and $c = 14.18704(21)$ Å. The distorted octahedron (2+2+2) has Ag-F bond lengths of 2.08695(9) Å, 2.11170(3) Å, and 2.49431(11) Å and the Cs-F in-plane distance is 3.24132 Å. (See Table 3.5 for a complete list of the *Bbcm* bond lengths and their comparison with *I4/mmm* bond lengths.) The bond lengths of the distorted octahedron with the Ag²⁺ center were used for the valence bond sum, which gave a silver oxidation state of 2.02. The different distances for the same type of bond show that the *Bbcm* unit cell is less symmetric than the *I4/mmm* unit cell. The F-Ag-F bond angles in the square plane of the octahedron are 89.909(5)°, 91.091° and 180.000(0)° due to fluorine displacement, while the same angles in the *I4/mmm* space group are 90° and 180°. The distortion is small, but still changes the structural properties of the material. The anisotropic displacement parameters are listed in Table 3.6.

Once again, a three phase refinement was used with AgF and CsF as impurities, which gave fitted fractions of 0.036 and 0.0061, respectively, with $\chi^2 = 1.293$. The ortep with the positions and ADPs generated from the Rietveld refinement is shown in Figure 3.9, and a histogram from the refinement itself is shown in Figure 3.10.

The neutron data was also fit with the space group $I\bar{4}c2$. These unit cell parameters are related to *I4/mmm* by $a_{I\bar{4}c2} = \sqrt{2}a_{I4/mmm}$, $b_{I\bar{4}c2} = \sqrt{2}b_{I4/mmm}$, and

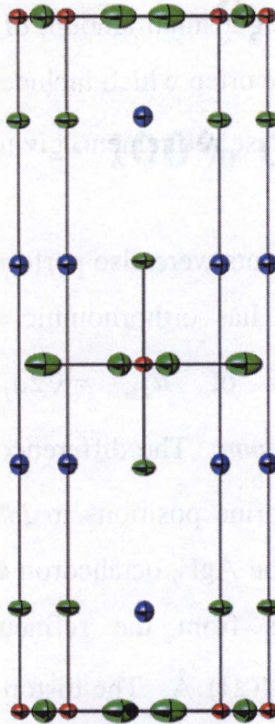


Figure 3.6: Ortep of Cs_2AgF_4 in the $I4/mmm$ space group at room temperature from the neutron data.

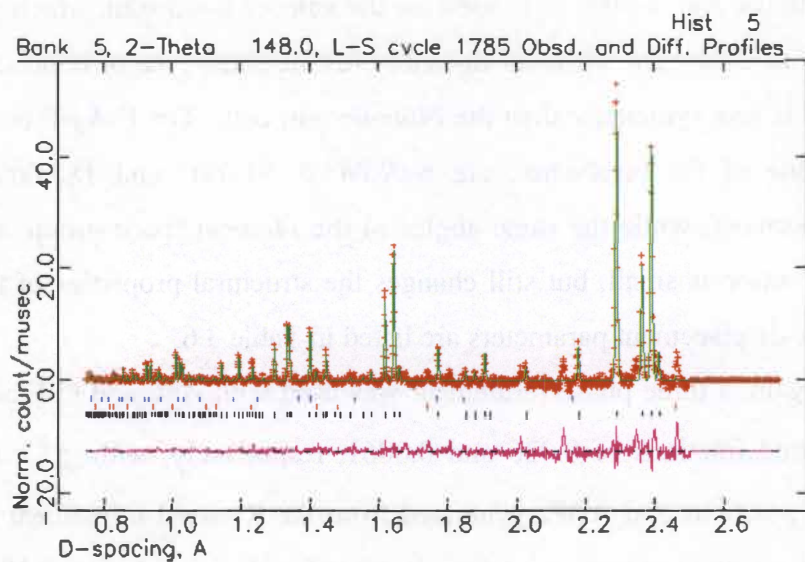


Figure 3.7: Three phase neutron Rietveld refinement using the $I4/mmm$ space group. The black represents the Cs_2AgF_4 peaks, the red marks represent the positions of AgF, and the blue represent CsF. The data in this plot is from the 148° bank of NPDF.

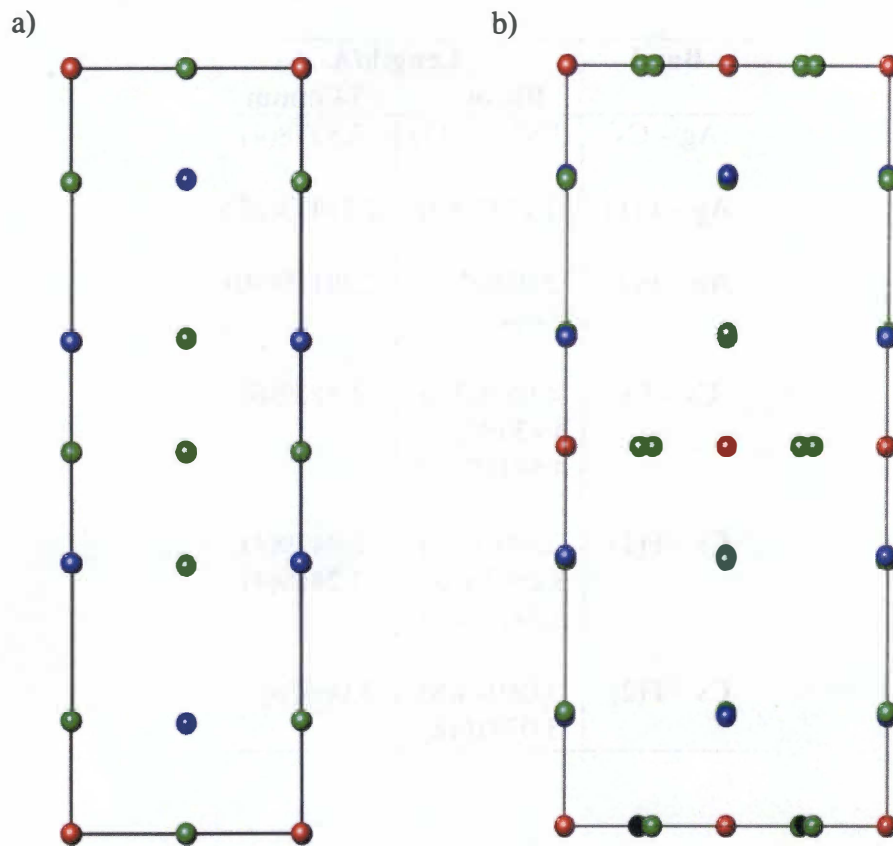


Figure 3.8: Comparison of the a) $I4/mmm$ and b) $Bbcm$ unit cells for an $n=1$ Ruddlesden-Popper phase.

Table 3.5: Bond lengths from the room temperature Cs_2AgF_4 *Bbcm* neutron refinement.

Bond	Length/Å	
	Bbcm	I4/mmm
Ag – Cs	3.82559(17)	3.8278(4)
Ag – F(1)	2.11170(3)	2.11413(27)
Ag – F(2)	2.08695(9) 2.49431(11)	2.29110(30)
Cs – Cs	4.06700(6) 4.43394(15) 4.58119(20)	4.5822(6)
Cs – F(1)	2.94832(4) 3.23935(20) 3.24132(20)	2.9429(4) 3.2410(4)
Cs – F(2)	3.06044(8) 3.07910(8)	3.06636(9)

Table 3.6: Thermal parameters from the room temperature *Bbcm* neutron refinement.

Atom	$U_{ij} \cdot 100$					
	U_{11}	U_{22}	U_{33}	U_{12}	U_{13}	U_{23}
Ag	3.17	1.73	1.64	0.82	0.0	0.0
Cs	3.42	0.89	2.08	0.22	0.0	0.0
F1	1.23	3.93	1.25	0.02	0.0	0.0
F2	3.32	3.39	2.80	0.29	0.0	0.0

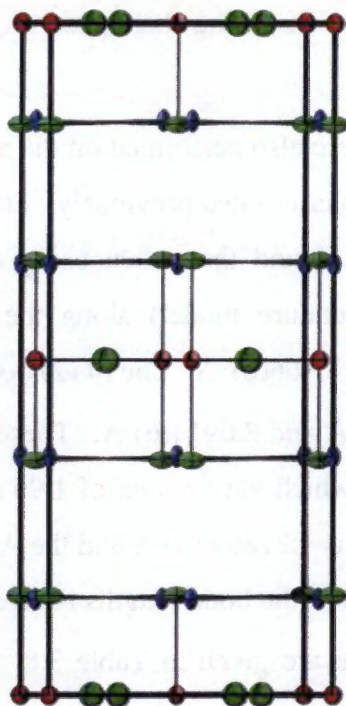


Figure 3.9: Ortep of Cs_2AgF_4 from the room temperature $Bbcm$ neutron refinements.

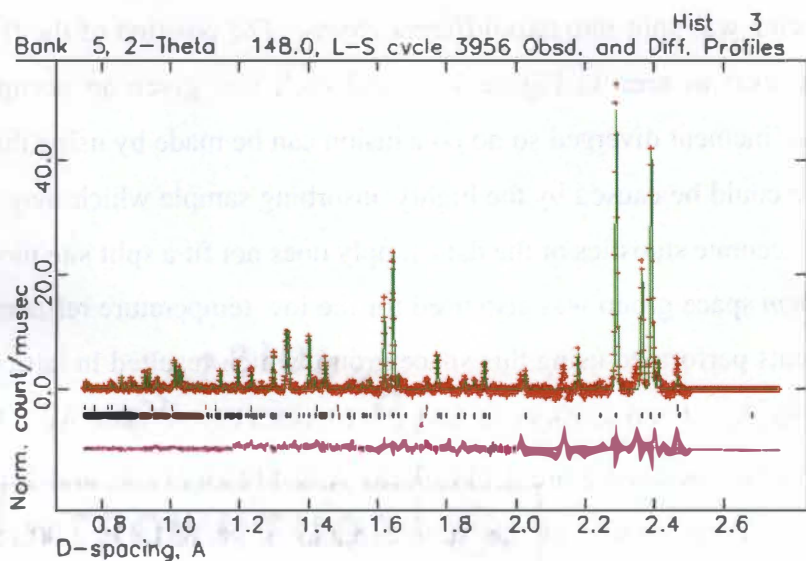


Figure 3.10: Rietveld refinement from the 148° detector bank of the room temperature Cs_2AgF_4 neutron data assuming the $Bbcm$ space.

$c_{I\bar{4}c2} = 2c_{I4/mmm}$. However, the fits using this space group did not converge and were therefore discarded.

Rietveld refinements were also performed on the neutron data at low temperature, (6K) assuming the same three phases cited previously. First the data was fit assuming the space group $I4/mmm$. It was found that when using $I4/mmm$, the lattice contracted (compared to the room temperature model) along the c axis, giving parameters of $a = b = 4.5573(13)$ Å and $c = 14.166(6)$ Å. The (4+2) octahedron of the Ag metal center has bond lengths of $2.2757(7)$ Å and $2.0914(6)$ Å. These bond lengths were used in the valence bond sum calculation which gave a sum of 1.96 for the silver center. The Cs-F bond distance in the CsF plane is $3.2186(10)$ Å and the Ag-F distance in the AgF_2 sheets is $2.2757(7)$ Å. A complete list of the bond lengths is given in Table 3.7, and the thermal parameters from the refinement are given in Table 3.8. These refinements gave a χ^2 value of $\chi^2 = 1.7066$, as shown in Figure 3.11 and an ortep using the parameters from the refinement is shown in Figure 3.12. The fitted sample purity was 95.13%, with impurity phases of 4.80% (AgF), and 0.2% (CsF).

The thermal parameters of the apical fluorine atom were elongated along the ab plane so a split-site refinement was attempted. For the split site refinement, each equatorial fluorine was split into two different atoms. The position of the fluorines were started 0.01 Å apart as seen in Figure 3.13, and each was given an occupancy of 0.5. However, the refinement diverged so no conclusion can be made by using this procedure. The divergence could be caused by the highly absorbing sample which may prevent high resolution and accurate statistics or the data simply does not fit a split site model.

The $Bbcm$ space group was also used for the low temperature refinements. Three phase refinements performed using this space group, which resulted in lattice parameters of $a = 6.4345(9)$ Å, $b = 6.4390(9)$ Å, and $c = 14.1495(12)$ Å. The Ag-F bond lengths in the (2+2+2) silver octahedra are $2.11139(18)$ Å, $2.11195(21)$ Å, and $2.44095(24)$ Å, with the F-Ag-F bond angles in the square plane of $89.831(11)^\circ$, $90.169(11)^\circ$, and $180.000(0)^\circ$. The complete list of bond distances from GSAS can be found in Table 3.9. Once again, these bond lengths were then used to find the bond valence sum for the silver

Table 3.7: Bond lengths from the Cs₂AgF₄ 6K *I4/mmm* refinement.

Bond	Length/Å
Ag – Cs	3.8123(9)
Ag – F(1)	2.0914(6)
Ag – F(2)	2.2757(9)
Cs – Cs	4.0872(12) 4.43907(9) 4.5513(14)
Cs – F(1)	2.9390(9) 3.2186(10)
Cs – F(2)	3.0586(7)

Table 3.8: Thermal parameters from the low temperature *I4/mmm* refinement.

$U_{ij} \cdot 100$						
Atom	U₁₁	U₂₂	U₃₃	U₁₂	U₁₃	U₂₃
Ag	1.82(13)	1.82(13)	1.57(19)	0.0	0.0	0.0
Cs	1.56(10)	1.56(10)	1.99(20)	0.0	0.0	0.0
F1	1.66(11)	1.66(11)	0.88(15)	0.0	0.0	0.0
F2	0.62(18)	9.16(30)	1.59(14)	0.0	0.0	0.0

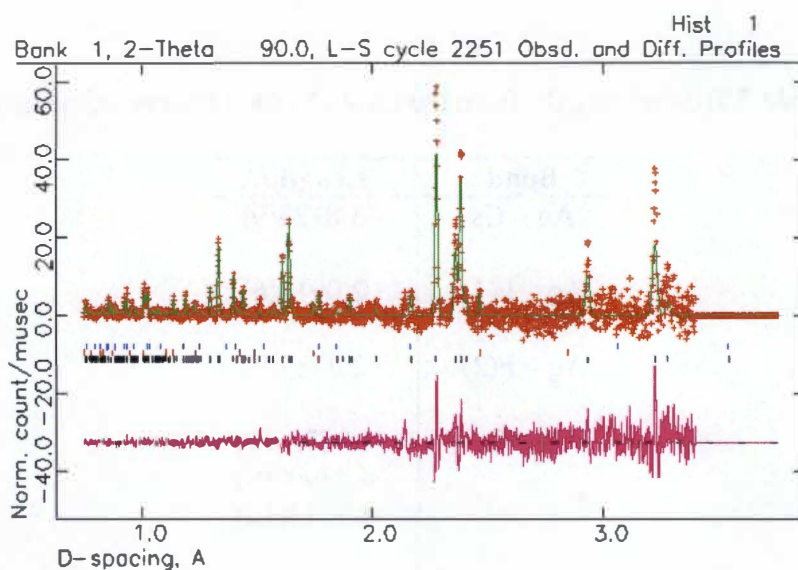


Figure 3.11: Rietveld refinement of the 48° bank of NPDF using the $I4/mmm$ space group for Cs_2AgF_4 at 6K.

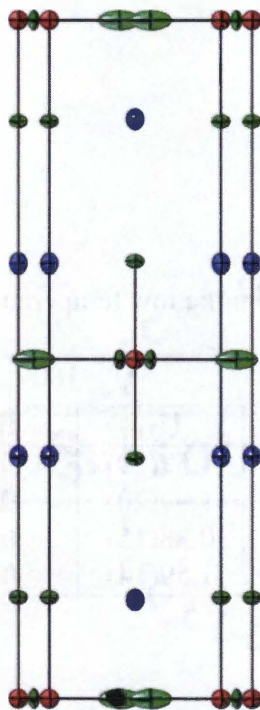


Figure 3.12: Cs_2AgF_4 unit cell model at 6K in the $I4/mmm$ space group. The blue atoms represent cesium, the red are silver, and the green atoms are fluorine.



Figure 3.13: Example of a split site model for the equatorial fluorines. Each fluorine has an occupancy of $\frac{1}{2}$.

Table 3.9: Bond lengths from the Cs_2AgF_4 6K *Bbcm* refinement.

Bond	Length/Å
Ag – Cs	3.8045(4)
Ag – F(1)	2.11139(18)
Ag – F(2)	2.11195(21) 2.44095(24)
Cs – Cs	4.5515(5) 4.4147(4) 4.05410(34)
Cs – F(1)	3.2206(5) 2.93633(24)
Cs – F(2)	3.09512(21) 3.00944(20)

center. This calculation gave a bond valence sum for Ag(II) of 2.021. The fit using the space group *Bbcm* looks better qualitatively than using the *I4/mmm* fit and resulted in a lower χ^2 , $\chi^2 = 1.423$ (Figure 3.14). Some of the thermal parameters however, gave values which are unphysical, i.e. the ADP values for some of the atoms were negative. Because the data was taken at such a low temperature, 6K, the thermal parameters are expected to be small. The low resolution of the data may have lead to a large error in the anisotropic displacement parameters, causing them to be slightly negative.

Refinements were also performed on the low temperature data using the $I4\bar{c}2$ space group. Just as in the case of the room temperature refinements, convergence was not achieved, and this space group was therefore rejected as a possible lattice symmetry.

3.2.3 Magnetic susceptibility

Magnetic susceptibility measurements show that Cs_2AgF_4 displays Curie-Weiss behavior, with a ferromagnetic ordering transition at 14.9K, and paramagnetic behavior at higher temperatures (Figure 3.15). A fit of the data to the 10th order high temperature series for the 2D Heisenberg ferromagnet gives an exchange constant of $J = -3.793\text{meV}$,

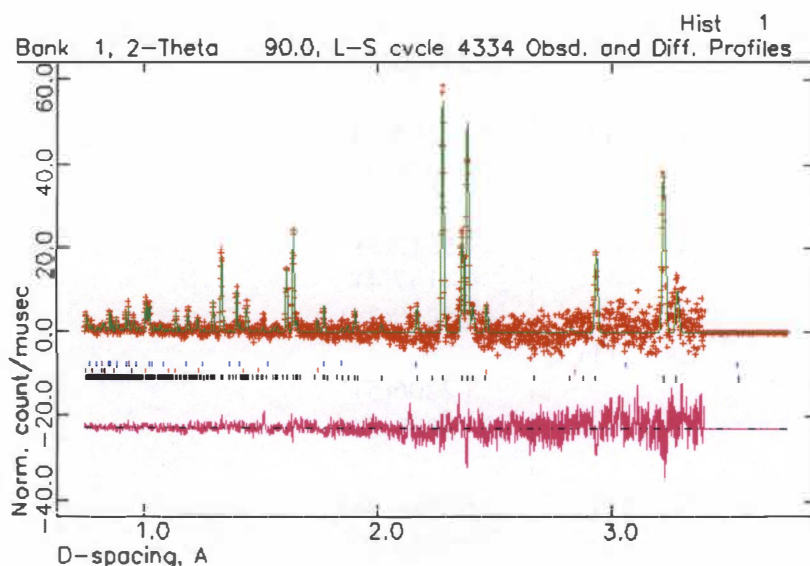


Figure 3.14: Rietveld refinement of the 48° bank of Cs_2AgF_4 data at 6K using the *Bbcm* space group.

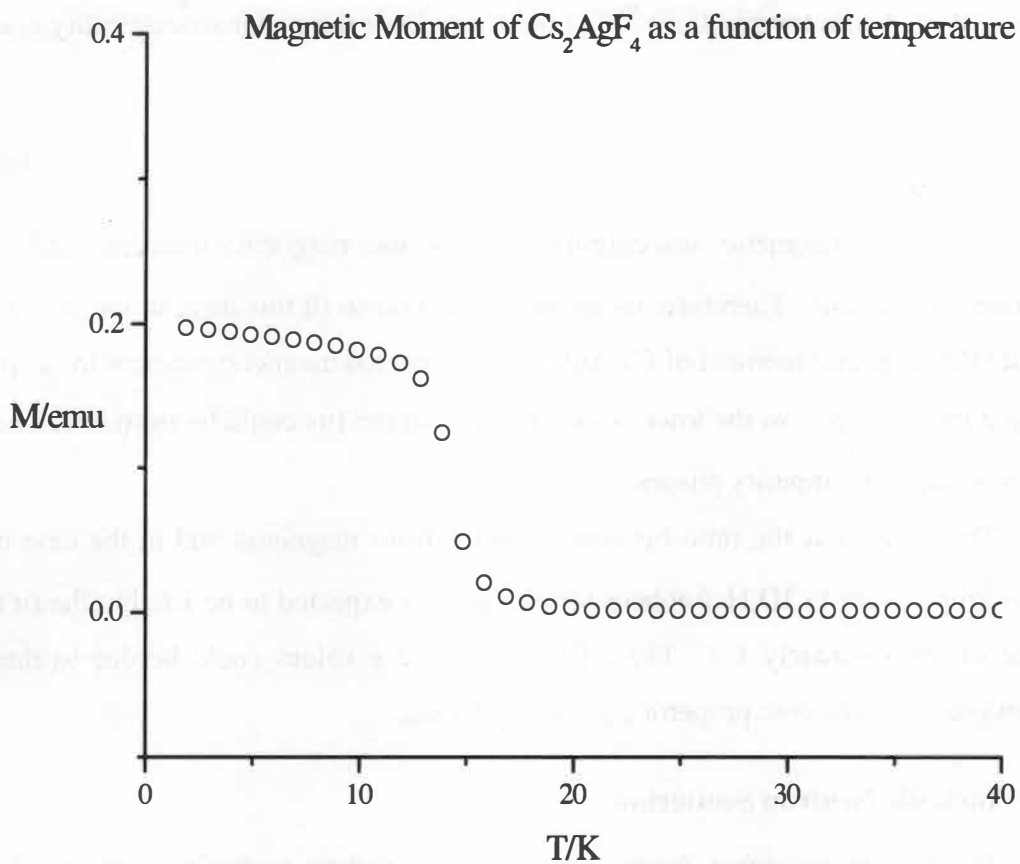


Figure 3.15: Magnetization data of Cs₂AgF₄ as a function of temperature.

a g factor of $g = 1.832$, and an Ag(II) ionic moment of $0.8\mu_B$ (Figure 3.16).⁸⁴

An ideal 2D Heisenberg ferromagnet will only order at 0K, so to estimate the ionic moment, the fit can only be usefully carried out significantly above 15K, (χ diverges at the Curie temperature).⁸⁹ At the Curie limit the molar susceptibility is equal to

$$\chi \sim \frac{\mu^2}{3kT} \quad 3.3$$

where χ is the magnetic susceptibility, μ is the magnetic moment, and k is Boltzmann's constant. Therefore, using the Curie limit to fit this data, it was possible to estimate the magnetic moment of Cs₂AgF₄. The expected magnetic moment for a spin-1/2 isotropic ion is $1.0\mu_B$, so the lower value given from the fits could be from covalency or from non-magnetic impurity phases.

The g factor is the ratio between μ and 1 Bohr magneton and in the case of an ideal isotropic, spin-1/2 2D Heisenberg ferromagnet, is expected to be 1.6, but the fit gave a value of approximately 1.8. The difference in the g values could be due to thermal fluctuations or anisotropic properties of the Ag(II) ion.

3.2.4 Inelastic Neutron Scattering

The first measurement taken using inelastic neutron scattering was well below this transition temperature at 8K. The raw data before the background subtraction can be seen in Figure 3.17a. There is a significant amount of scattering at low Q values, particularly at wave vectors less than 1\AA^{-1} . This low Q scattering is magnetic based on the fact that when the sample was warmed up to 150K, this intensity broadens out and decreases. Also, the scattering at higher Q values is a result of phonons and intuitively increases with the temperature according to the Bose-Einstein occupancy of the phonon modes. Figure 3.18 shows the data at 150K which is dominated by scattering due to phonons.

Because of the magnetic scattering at low wave vectors, the subtraction of the Teflon background was of the utmost importance. By running the empty cell, it was found that PTFE elastically scatters very strongly at 1.3\AA^{-1} as shown in Figure 3.19 and it

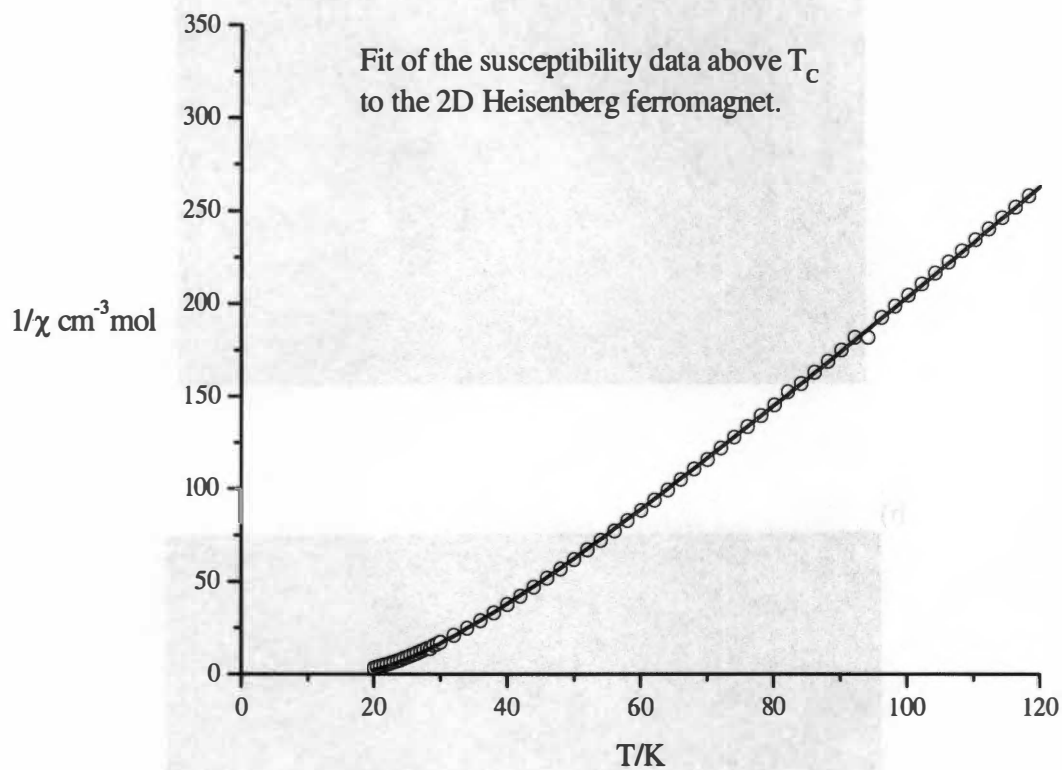


Figure 3.16: Fit of the 10th order ferromagnetic 2D Heisenberg model susceptibility to Cs_2AgF_4 , using data above the Curie temperature.⁸⁴⁻⁸⁶

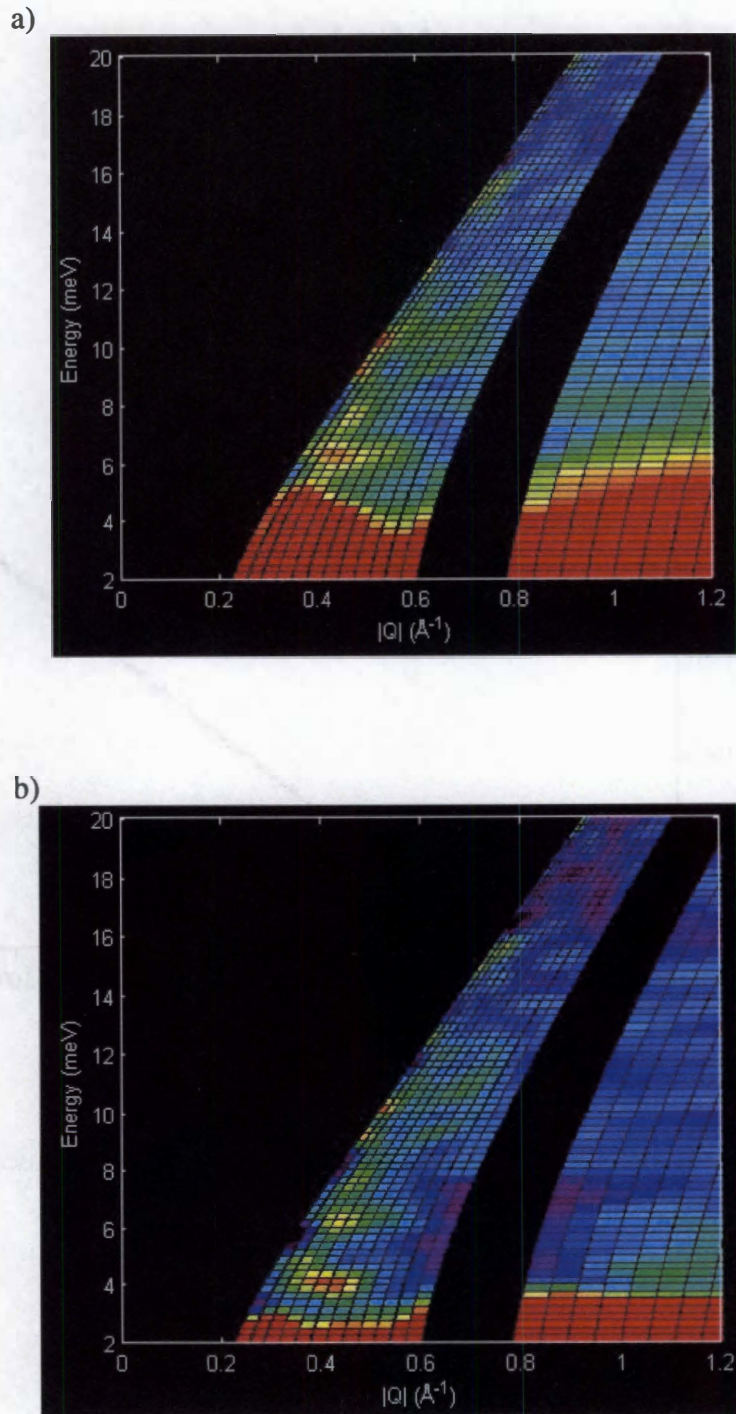


Figure 3.17: a) Cs_2AgF_4 inelastic neutron scattering data for $E_i=50\text{meV}$, $T=8\text{K}$, before background subtraction and b) after background subtraction.

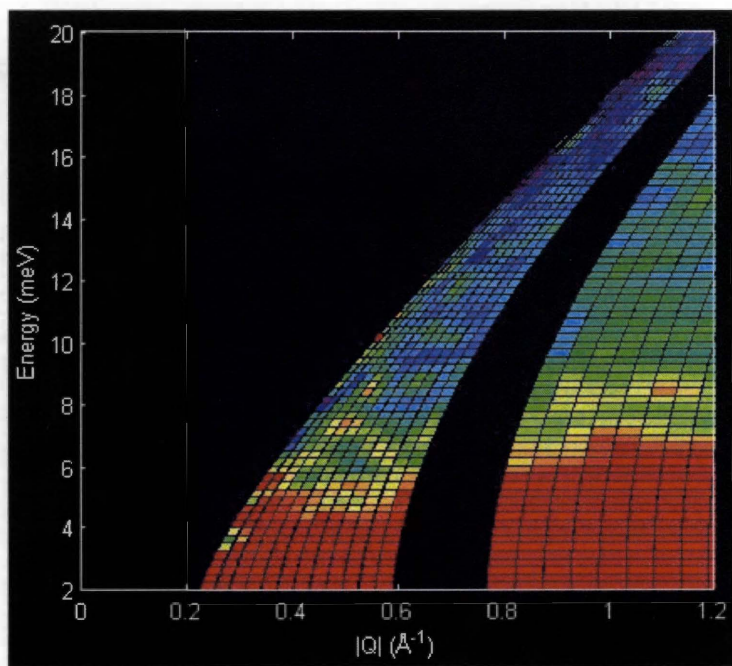


Figure 3.18: Cs_2AgF_4 inelastic neutron scattering data with $E_i=50\text{meV}$ and $T=8\text{K}$. The scattering intensity at these higher temperatures is due to phonons.

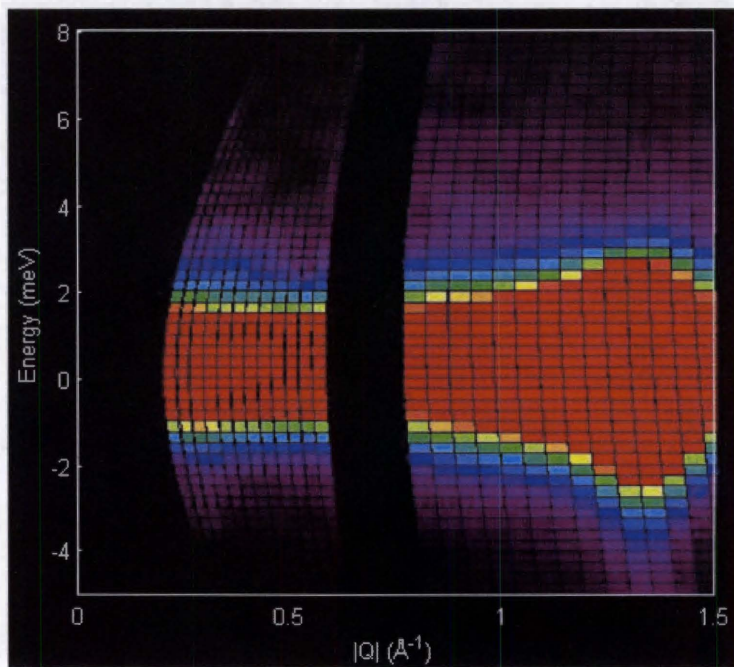


Figure 3.19: PTFE and aluminum can background data at $E_i=50\text{K}$. Note the elastic peak at $Q=1.3\text{\AA}^{-1}$.

extends into the low vector region crucial to the magnetic scattering. This Bragg peak from the teflon is affected by absorbance from the sample and actually decreases in intensity by approximately 20% when the sample was present. Therefore, the elastic peak was scaled appropriately when subtracting the background. Figure 3.17b shows the data once the background subtraction was performed.

Simulations were then performed to determine the theoretical scattering of a Heisenberg ferromagnet and antiferromagnet. An approximation of the dispersion of spin waves for an antiferromagnet is expressed as

$$\omega_{AF}(\mathbf{Q}) = 2SJ\sqrt{4 - (\cos(Q_a a) + \cos(Q_b a))^2} \quad 3.4$$

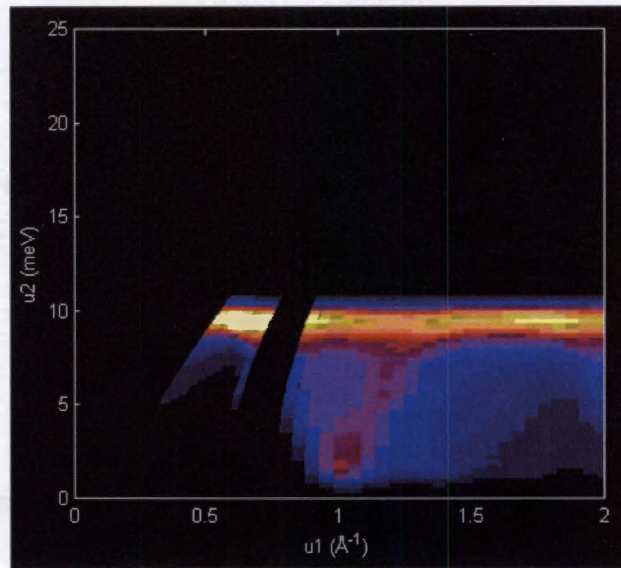
where $\omega_{AF}(\mathbf{Q})$ is the spin wave dispersion, S is the total spin, J is the coupling constant, Q is the wave vector, and a is the lattice spacing. The intensity of this pattern is weak and at low wave vectors, depends on Q linearly as shown in Figure 3.20a. However, the dispersion relation in a ferromagnet can be written as

$$\omega_F(\mathbf{Q}) = 2SJ(2 - \cos(Q_a a) - \cos(Q_b a)) \quad 3.5$$

where the intensity, as shown in Figure 3.20b, shows a cosinusoidal shape in the low Q boundary region. Figure 3.21 shows the fit of the ferromagnetic dispersion relation to the actual data.

By comparing the data obtained to the patterns from the simulations, it is quite clear that the data qualitatively resembles that of a ferromagnet. The data was fit to a 2D Heisenberg ferromagnet to obtain the coupling constant. To calculate J , the dispersion relation in equation 3.5 was found by taking the energy at constant wave vectors and Gaussian peaks were fit to the profile. The resulting coupling constant was $J = -5.0(4) \text{ meV}$, which is higher than the J value from the susceptibility measurements which could mean that the J value above the transition temperature is significantly different from the coupling constant below this temperature. These fits were performed only with the data below the wave vector region where the phonon scattering becomes dominant, and also, only the data above 6 meV was used in the fit because below this energy, any magnetic signal is masked by the quasi-elastic incoherent scattering that occurs.

a)



b)

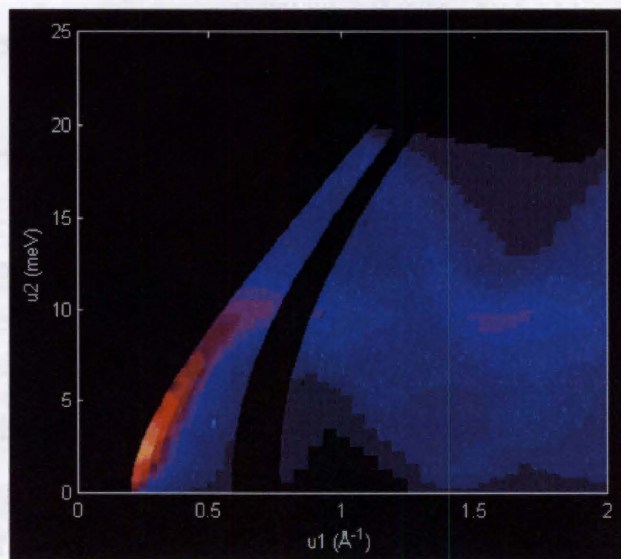


Figure 3.20: Simulated inelastic scattering pattern of Cs_2AgF_4 at $E_i=50$ for a) a2D Heisenberg antiferromagnet, and b) a 2D Heisenberg ferromagnet.

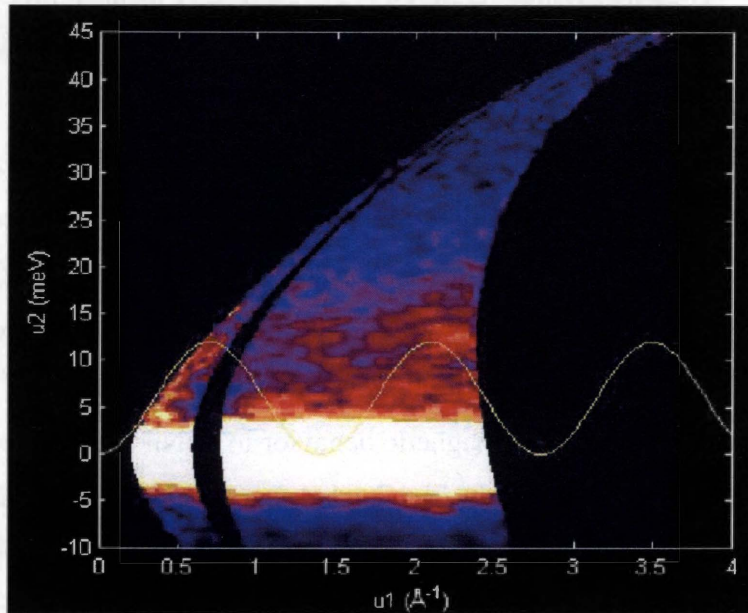


Figure 3.21: Cs_2AgF_4 inelastic scattering data at 8K fit to the ferromagnetic, cosinusoidal dispersion relation.

3.3 Discussion

3.3.1 Magnetism

The data from the susceptibility measurements clearly shows that the magnetic behavior of Cs_2AgF_4 is ferromagnetic and it also gives an estimate of the coupling constant, and the magnetic moment. Although susceptibility measurements such as these are useful for determining the general bulk magnetic behavior, inelastic neutron scattering was necessary to understand the interactions on a local scale. These results accurately confirmed the value of J to be $-5.0(4)$ meV which shows that the magnetic properties of Cs_2AgF_4 are indeed similar to those of a 2D Heisenberg ferromagnet.

Magnetic interactions in Cs_2AgF_4 were calculated by Grochala and Hoffman to be antiferromagnetic as in of La_2CuO_4 and K_2NiF_4 . K_2NiF_4 is a $S=1$ antiferromagnet with a Néel temperature of 180K and a coupling constant of 9.5 meV.^{90,91} Initial neutron measurements showed the antiferromagnetic behavior in K_2NiF_4 was 2D in nature due to the super-exchange interaction within each nickel sheet.⁹² This study noted that there was, however, a small amount of anisotropy between second nearest neighbor nickel sheets which caused the spin to align along the c -axis. Susceptibility measurements by Legrand and Van den Bosch, who paid particular attention to this anisotropy, reported that the anisotropy amounts to $1.5(\pm 0.2)\%$.⁹³ It was also found that the exchange and dipolar interactions between the nearest neighbor Ni^{2+} sheets cancel out below the transition temperature, but later measurements discovered a transition at 97.23K where a weak long range 3D antiferromagnetic effect begins.^{92,94,95}

La_2CuO_4 is a $S=1/2$ 2D Heisenberg antiferromagnet that orders at a Néel temperature of 325K and has a strong spin-spin magnetic exchange constant of approximately 120 meV.⁹⁶ This system consists of a 2D antiferromagnetic arrangement in the CuO_2 planes as seen in Figure 3.22.⁹⁷ The nearest neighbors of the in-plane coppers are aligned in an antiparallel arrangement where the spins in the bc plane are canted 0.17° away from the c axis.⁹⁷ This coupling between the Cu in-plane spins is extremely strong, but along with this 2D interaction, there is also a very weak interlayer coupling which is evident by the fact that the ordering temperature is not 0K.⁹⁸ This weak interlayer

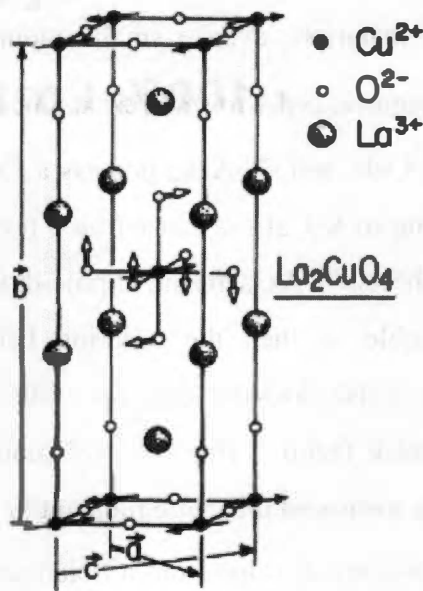


Figure 3.22: Antiferromagnetic array in the CuO_2 planes of La_2CuO_4 .⁹⁷ The arrows on the oxygen in the center octahedra represent the direction of rotation that causes the orthorhombic distortion.

coupling results in a highly anisotropic antiferromagnet where the coupling between copper and its out-of-plane nearest neighbors is unequal in its magnitude, resulting in two different J values. This interlayer coupling between the copper and its out-of-plane neighbors is believed to be caused by the orthorhombic distortion because in the high temperature tetragonal structure in La_2CuO_4 , the interaction between the Cu ions in the ab and bc planes is equal.⁹⁹

The inelastic neutron scattering results and the susceptibility measurements of Cs_2AgF_4 obviously do not agree with the magnetic behavior of K_2NiF_4 and La_2CuO_4 . Instead, Cs_2AgF_4 resembles K_2CuF_4 in its magnetic properties. K_2CuF_4 is one of the few known 2D spin $\frac{1}{2}$ ferromagnetic insulators.^{100,101} Its magnetism fits the 2D Heisenberg model with a coupling constant of $J = -1.0\text{meV}$ and possesses an ordering temperature of $T_c = 6.25\text{K}$. This 2D effect was investigated thoroughly by Yamada through susceptibility and specific heat measurements.⁸⁹ The ferromagnetic ordering occurs in the Cu(II) ions where the spins are aligned in the c plane.¹⁰² The susceptibility measurements were fit to a 2D Heisenberg ferromagnet using the fit developed by Baker et al.⁸⁴⁻⁸⁶ as

described above. Although it is known that an ideal 2D Heisenberg ferromagnet will order at $T_c = 0K$, in real materials, even a small amount of inter-layer coupling or anisotropy will cause the magnetic order to stabilize at a non-zero temperature, T_c which would explain why both K_2CuF_4 and Cs_2AgF_4 possess a Curie temperature above $0K$.⁸⁹ The weak interlayer coupling in K_2CuF_4 is caused by a ferromagnetic interaction of the copper ions in the CuF_2 sheets.¹⁰³ As a result, dipole-dipole interactions between the CuF_2 planes are not possible as then the ordering between the layers would be antiferromagnetic.¹⁰³ There is also evidence that this weak 3D effect in Cs_2AgF_4 is seen in its magnetic moment and g factor. The expected moment for an isotropic spin- $\frac{1}{2}$ Ag(II) ion is $1.0 \mu_B$, but the measured magnetic moment is $0.8 \mu_B$, while the expected g factor would be $g=1.8$ and the actual value from a field magnetization scan at $5K$ is 1.6 . The slight differences could be due to covalency effects, fluctuations, or hybridization.

3.3.2 Orbital ordering

The type of magnetism displayed by a certain material arises from the ordering of the orbitals of the participating atoms. For example, it is possible to explain the magnetism and orbital ordering by referring back to crystal field theory and Jahn-Teller distortion. When a $3d^9$ metal center undergoes a Jahn-Teller distortion, there are two possibilities for the ground state, a_{1g} or b_{1g} .¹⁶ Axial compression of an octahedron results in a partially filled a_{1g} orbital which is the $3z^2-r^2$ orbital as shown in Figure 3.23a whereas an axial elongation results in a b_{1g} ground state which is the x^2-y^2 orbital and can be seen in Figure 3.23b.^{16,90} However, thus far, there has been no known system which possesses an a_{1g} ground state, rather, the ground state is described using alternating partially filled z^2-x^2 and z^2-y^2 orbitals as seen in Figure 3.23c.

An example of orbital ordering in which a b_{1g} ground state occurs is La_2CuO_4 . In La_2CuO_4 , there is a CuO_6 octahedral with a d^9 center giving an electronic configuration of $t_{2g}^6 e_g^3$.⁹⁰ The three electrons in the e_g energy level result in a Jahn-Teller distortion where the distorted spin monomer is placed in the highest energy d orbital which is the x^2-y^2 orbital.⁹⁰ Therefore, an axial elongation occurs in this system and a b_{1g} ground state

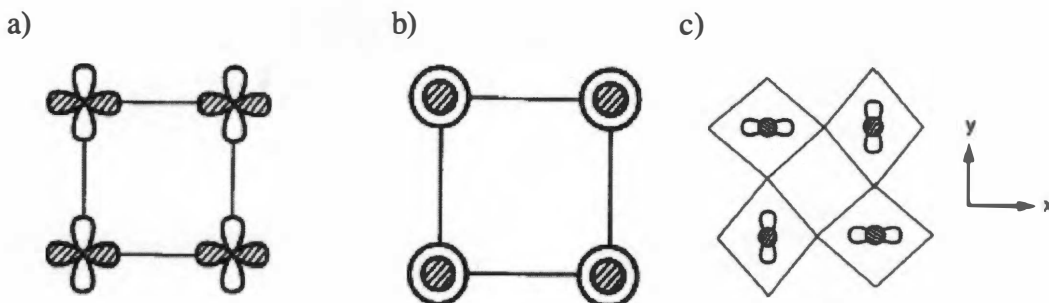


Figure 3.23: Orbital ordering for a) b_{1g} ground state, b) a_{1g} ground state, and c) linear combination of x^2-y^2 and x^2-x^2 d -orbitals as a possible ground state.

results with the unpaired electron occupying the highest d orbital which is $d_{x^2-y^2}$.^{16,90} Here, a large overlap of the Cu(II) x^2-y^2 orbital with the oxygen ligand p orbital occurs which results in the strong antiferromagnetism that is displayed by the high T_C cuprates. Figure 3.24 shows this type of ordering that is seen in La_2CuO_4 .

As mentioned, K_2NiF_4 also exhibits antiferromagnetic properties and has a b_{1g} ground state, but its origins are different than that of La_2CuO_4 . In K_2NiF_4 , a central octahedral NiF_6 complex exists, but unlike La_2CuO_4 , there are two unpaired spins in each e_g orbital and a Jahn-Teller distortion is not observed, however, there is a slight distortion of the octahedral in K_2NiF_4 , but it could be a result of anisotropy in the layered structure mentioned earlier. One of the unpaired electrons occupies the $d_{x^2-y^2}$ orbital and the other electron occupies the d_{z^2} orbital. As a result, a spin dimer, and antiferromagnetic interaction is likely to be counterbalanced by a ferromagnetic interaction which is why the coupling constant of K_2NiF_4 is not as large as in La_2CuO_4 .⁹⁰ Also, there is a large energy gap in the interaction between the x^2-y^2 orbitals shown in Figure 3.23a which is likely to give rise to the antiferromagnetic behavior.⁹⁰

As in La_2CuO_4 , Jahn-Teller distortion is also responsible for the ferromagnetic ordering of K_2CuF_4 . However, theoretical work by Kugel and Khomskii, and later experimental work by Ito and Akimitsu showed that the in-plane orbital ordering seen in La_2CuO_4 was not a possible mechanism for the ferromagnetic ordering seen in

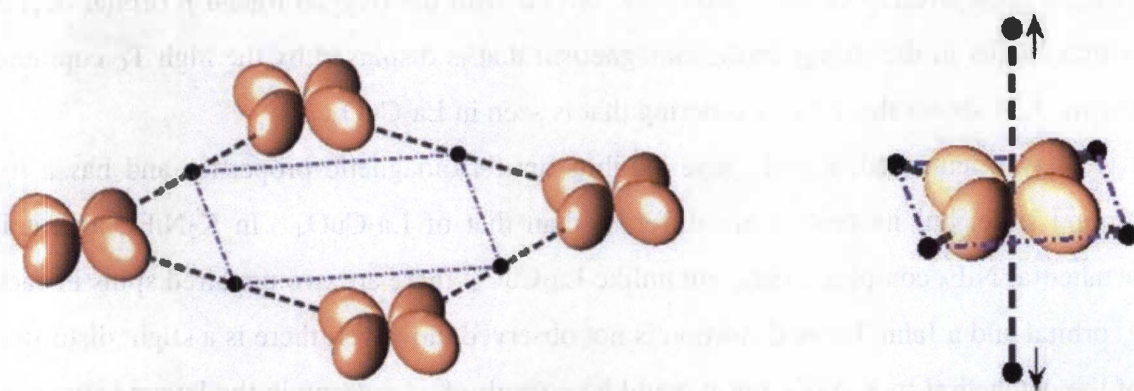


Figure 3.24: Formation of a b_{1g} ground state with partial filled x^2-y^2 orbitals (left) is accompanied by axial extension of octahedral ligands (right).

K_2CuF_4 .¹⁰⁴⁻¹⁰⁶ A b_{1g} ground state would not be possible in the case of a ferromagnet based on Hund's rules. If there is a positive overlap between the x^2-y^2 copper orbitals and the p orbitals of the fluorine, then the overlap would cause the two unpaired electrons to fall into the same orbital and due to Hund's rules, two spins must align antiparallel thus causing an antiferromagnetic ordering. Also, if the ground state were a_{1g} with z^2-r^2 orbitals, then the same problem would occur with the positive overlap causing an antiferromagnetic spin alignment. However, the z^2-r^2 orbitals can be split up into linear combinations of orthogonal, non-overlapping orbitals. These orbitals, the z^2-x^2 and z^2-y^2 orbitals, are the linear combinations of the $3z^2-r^2$ orbital and alternate at each corner around the c axis by 90° , therefore allowing a ferromagnetic ordering in the copper ions of the K_2CuF_4 lattice without breaking Hund's rules. Ito and Akimitsu, showed experimental evidence for this orbital ordering scheme by performing a polarized neutron study.¹⁰⁵ This study showed anisotropy of the spin density distribution which is evidence for the proposed orbital ordering effect, as the spin-spin interaction of a symmetric tetragonal structure would be isotropic.¹⁰⁵ Therefore, the antiferrodisordered pattern of the z^2-x^2 and z^2-y^2 orbitals of K_2CuF_4 as seen in Figure 3.25 results in a strong ferromagnetic state along with a distortion of the fluorine atom positions which lowers the symmetry from the $I4/mmm$ to the $Bbcm$ space group. It is suggested that Cs_2AgF_4 also follows this particular orbital ordering which also occurs in K_2CuF_4 . Due to the fact that it shares strong magnetic similarities with K_2CuF_4 , it is not possible for Cs_2AgF_4 to possess the same orbital scheme described for La_2CuO_4 and K_2NiF_4 .

3.3.3 Structure

In search for the structural characterization, the neutron data was fit to the $I4/mmm$ space group, which is the K_2NiF_4 structure type (Figure 3.26) and is also the initial characterization of the material, and $Bbcm$, which is the space group of K_2CuF_4 (Figure 3.27).

At room temperature, the Cs_2AgF_4 $I4/mmm$ model fits the data well, with a χ^2 of $\chi^2 = 1.330$. However, the fit to the data at low temperature, while giving a slightly

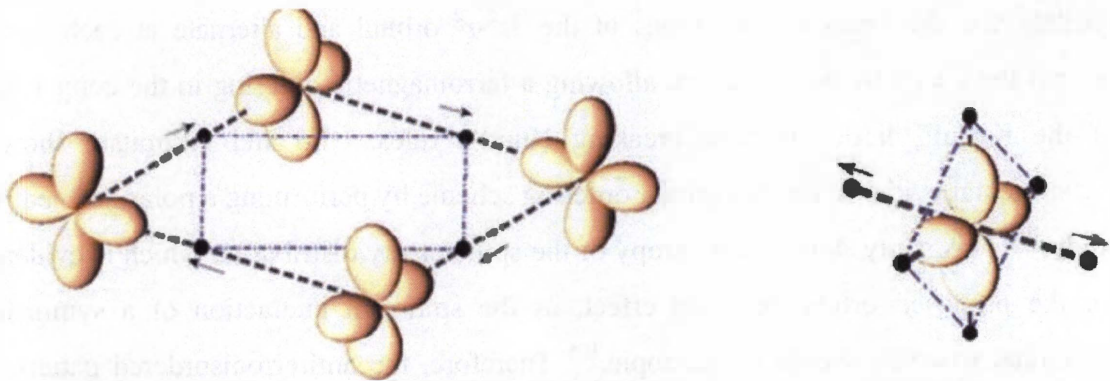


Figure 3.25: Anharmonic coupling to ligands favors the formation of staggered orbital ordering of z^2-x^2 and z^2-y^2 orbitals, as in K_2CuF_4 . In-plane ligands are displaced from central positions, lowering the crystal symmetry. Strong ferromagnetic super-exchange occurs through the unfilled in-plane orbitals.

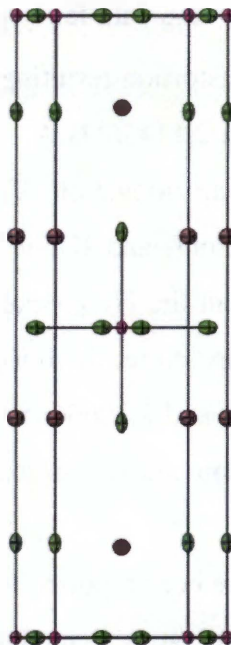


Figure 3.26: The unit cell of K_2NiF_4 including the thermal parameters. Lattice parameters are $a = b = 4.013 \text{ \AA}$ and $c = 13.088 \text{ \AA}$. The pink atoms are nickel, green atoms are fluorine, and the brown atoms are potassium.

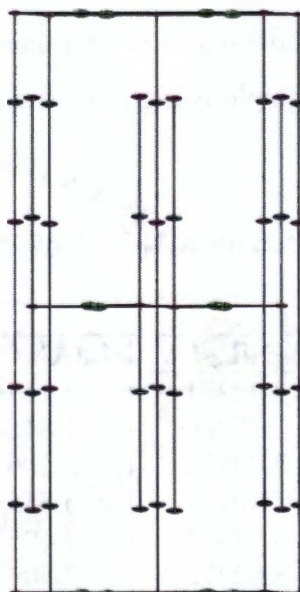


Figure 3.27: Ortep of K_2CuF_4 which is of the $Bbcm$ space group. The blue atoms represent copper, the green is fluorine, and the brown atoms are potassium.

higher χ^2 value of $\chi^2 = 1.7066$, fits the data fairly poorly (See Figure 3.10). The AgF_6 octahedron undergo a Jahn-Teller distortion resulting in a (4+2) octahedral complex with bond lengths of 2.29110(30) Å and 2.1143(27) Å. These bond lengths indicate that an axial contraction occurs rather than an elongation. The contraction is direct evidence that the orbital ordering model of La_2CuO_4 and K_2NiF_4 is not applicable to Cs_2AgF_4 . In K_2NiF_4 , distortion is not observed in the NiF_6 octahedron and the Ni-F bond length is 2.0065 Å. In La_2CuO_4 at room temperature, the bond lengths in the CuO_6 octahedra are 1.84800 Å for the in-plane oxygens, and 2.20666 Å for the axial oxygen atoms, which is evidence of the Jahn-Teller distortion causing an axial elongation along the *c* axis (See Table 3.10).

Many conflicting results have been reported for the structure of La_2CuO_4 . Studies have determined that La_2CuO_4 undergoes a tetragonal to orthorhombic distortion at approximately 500K.^{75,76,107,108} Also, the space group at high temperature is generally agreed to be the tetragonal *I4/mmm* space group, but the space group below the transition temperature is still in question. Reported space groups for the orthorhombic phase of La_2CuO_4 are *Cmca*, *Fmmm*, and *Bmab*. The most likely structure, however, is *Cmca*. This structure was reported by Jorgenson et. al. and the structure was determined by using powder diffraction on a sample that is greater than 95% pure.¹⁰⁷ This assumption is made because the purity of the sample is high, but more importantly neutron diffraction

Table 3.10: Bond length comparison for K_2NiF_4 , La_2CuO_4 , and Cs_2AgF_4 , all in the *I4/mmm* space group.

Bond	K_2NiF_4 / Å	La_2CuO_4 / Å	Cs_2AgF_4 / Å
Ni-K/La-Cu/Cs-Ag	3.42271	3.14783	3.82009(9)
Ni-F ₁ /Cu-O ₁ /Cs-F ₁	2.0065	1.84800	2.29110
Ni-F ₂ /Cu-O ₂ /Cs-F ₂	2.00652	2.20666	2.11413(27)
K-K/La-La/Cs-Cs	4.013	3.88593	4.5822(6)
	3.92814	3.69600	4.4287(4)
	3.82772	3.50920	4.0760(5)
K-F ₁ /La-O ₁ /Cs-F ₁	2.77289	2.54828	3.06636(9)
K-F ₂ /La-O ₂ /Cs-F ₂	2.83913	2.65228	3.2410(4)
	2.62362	2.42357	2.9410

studies are more reliable than the X-ray diffraction studies due to the ability of neutron diffraction to better locate the position of the oxygen atoms. Despite the discrepancies in the space group determination, each of the space groups are similar to the $I4/mmm$ space group. The study by Longo performed the diffraction experiment at several different temperatures and reported that the c/a ratio changed very little, indicating that there is a very subtle change going from the orthorhombic to the tetragonal phase.¹⁰⁸ Therefore, it is reasonable to compare the structure of Cs_2AgF_4 , (with the original structure proposed to be $I4/mmm$) to La_2CuO_4 .

Further evidence that the orbital ordering seen in La_2CuO_4 cannot be applied to Cs_2AgF_4 is in the atom displacement parameters of the equatorial fluorines in Cs_2AgF_4 . As seen in Figure 3.5 and Figure 3.11, the thermal displacement in these fluorines is stretched out along the a axis. To normalize the ADPs of the fluorines, their thermal parameters were divided by the parameters of cesium, the heaviest atom in the system. As shown in Table 3.11, the ADP's of the equatorial fluorines still show an elongation after normalization. The abnormal elongation is a signature of disorder, which in this case, would be in the plane of the AgF_6 octahedra.

The $Bbcm$ space group of K_2CuF_4 shows this type of disorder and therefore it is believed that this is also the structure of Cs_2AgF_4 . Fits were performed on Cs_2AgF_4 and at room temperature, the χ^2 value was $\chi^2 = 1.293$ which is smaller than the $I4/mmm$ room temperature fit. The low temperature data gave non-physical thermal parameters, but this could be due to resolution of the experiment and to the highly absorbing sample where small shifts may not be easily detectable. The $Bbcm$ model, as seen in Figure 3.8 does not show the degree of atomic displacement in the equatorial fluorines as in the

Table 3.11: Normalized thermal parameters from the low temperature $I4/mmm$ refinement.

$U_{ij} \cdot 100$						
Atom	U_{11}	U_{22}	U_{33}	U_{12}	U_{13}	U_{23}
F1	0.42	5.39	0.81	0.0	0.0	0.0
F2	1.09	1.09	0.45	0.0	0.0	0.0

Table 3.12: Bond length comparison for K_2CuF_4 and Cs_2AgF_4 , in the $Bbcm$ space group.

Bond	$K_2CuF_4 / \text{\AA}$	$Cs_2AgF_4 / \text{\AA}$
K-K/Cs-Cs	4.17497	4.43394(15)
K-Cu/Cs-Ag	3.46922	3.82559(17)
K-F ₁ /Cs-F ₁	2.60410	3.23935(20)
	2.95442	2.94832(4)
K-F ₂ /Cs-F ₂	2.77568	3.0664(4(8)
Cu-F ₁ /Ag-F ₁	1.93939	2.1170(3)
Cu-F ₂ /Ag-F ₂	2.23440	2.49431(11)
	1.94035	2.08594(9)

$I4/mmm$ model. This could be an indication that the space group is correct. Also, the axis of the octahedral contracts with the in plane Cu-F distance being 1.94035 Å and has a Cu-F bond of 2.23440 Å in K_2CuF_4 . In Cs_2AgF_4 the in-plane Ag-F distances are 2.49431(11) Å and 2.08695(9) Å while the axial Ag-F distance is 2.1170(3) Å. See Table 3.12 for a comparison of bond lengths of K_2CuF_4 and Cs_2AgF_4 . This evidence shows the Jahn-Teller distortion causes a contraction in the octahedral as it does in K_2CuF_4 and therefore the orbital ordering scheme presented for a ferromagnet is a viable option for the arrangement of the d orbitals in Cs_2AgF_4 .

To test the goodness of fit result in regards to the amount of distortion, refinements were performed where the distance of the fluorine displacement was varied from no distortion, which is the $I4/mmm$ space group, to a distortion of 0.35 Å, which is the stabilized distortion for the $Bbcm$ space group. Figure 3.28 shows that the χ^2 value of both $I4/mmm$ and $Bbcm$ could be possible configurations, but the $Bbcm$ space group χ^2 value is the lowest

3.3.4 Conclusion

Although the models for Cs_2AgF_4 in the $I4/mmm$ and $Bbcm$ space groups both fit the low temperature data, the $Bbcm$ space group gives a lower χ^2 and also the $I4/mmm$ space group shows a large displacement in the thermal parameters of the equatorial fluorine position which indicates disorder. Also, the type of orbital ordering for the $I4/mmm$ space group physically cannot produce a ferromagnetic effect like that seen in

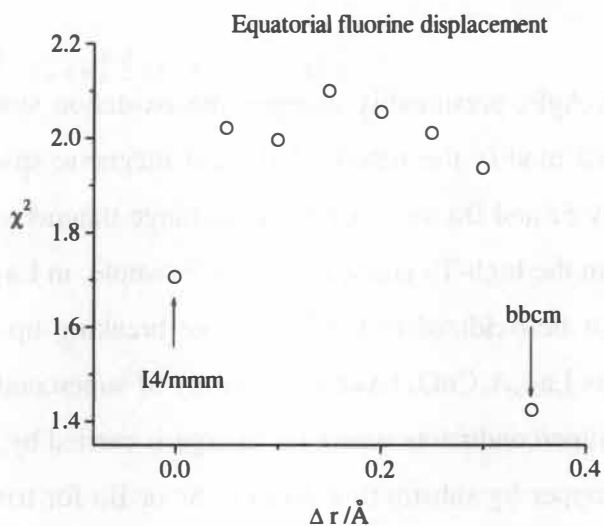


Figure 3.28: χ^2 value versus fluorine displacement for the low temperature Cs_2AgF_4 data. The fluorine displacement is Δr which is the distance from the symmetric $I4/mmm$ fluorine position to the displaced $Bbcm$ fluorine position.

Cs_2AgF_4 . Therefore, the ferromagnetic behavior of Cs_2AgF_4 most likely arises from the alternating $z^2 - y^2$ and $z^2 - x^2$ orbital ordering that is a product of the $Bbcm$ structure with a slight distortion in the equatorial fluorines.

4 Structural determination of $\text{Cs}_{1.9}\text{Ba}_{0.1}\text{AgF}_4$

4.1 Introduction

Doping of Cs_2AgF_4 presumably changes the oxidation state of the $S=1/2$ Ag^{2+} silver ions, which will modify the nature of the 2D magnetic spin lattice, just as hole doping of La_2CuO_4 by Sr and Ba ions disrupts long range magnetic correlations between the $S=1/2$ Cu^{2+} ions, in the high- T_C cuprates. As an example, in $\text{La}_{2-x}\text{Ba}_x\text{CuO}_4$, for every Ba^{2+} ion, a Cu^{2+} must be oxidized to Cu^{3+} therefore breaking up the alignment of the unpaired spins.¹⁰⁹ This $\text{La}_{2-x}\text{A}_x\text{CuO}_4$ ($\text{A}=\text{Ba},\text{Sr}$) family of superconducting copper oxides are known as *p*-type superconductors where the charge is carried by positive holes caused by the oxidation of copper by substituting divalent Sr or Ba for trivalent La resulting in the average oxidation state of copper to be greater than two.¹⁰⁹ Hole doping occurs in the magnetic CuO_2 planes, which drives an insulator to metal transition and results in a high- T_C superconductor. This statement means that the hole doping allows electrons to be removed from the Cu-O plane leaving behind vacancies in the band, which act as positively charged particles, and allow electrons hop hole sites. At some value of x , enough holes are created for the Cu-O layers to become metallic.¹¹⁰ What makes a superconductor a unique type of metal is that the resistance is zero below a certain critical temperature. An electron-lattice interaction occurs in metals which can deform or polarize the lattice, causing a displacement of ions by electric forces. This slight change in atomic position affects the other electron in the orbital due to the polarization and becomes surrounded by a positive charge which leads to an effective interaction between the electrons. The weak attraction between the electrons, which are called Cooper pairs, are close to the Fermi level and are slightly lower in energy, therefore leaving a small energy gap which inhibits the kind of interactions which lead to ordinary resistance seen in metals.¹¹⁰

In superconducting materials such as the copper oxides, the exact dynamics which cause the transition to a superconductor at higher temperatures remain unknown. The theory that best describes the high T_C superconductors is the *t*-*J* model, which is similar to the 2D Heisenberg model but includes a hole hopping term

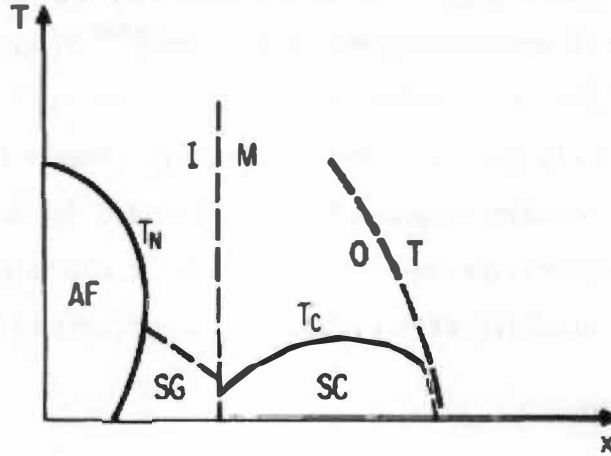


Figure 4.1: Phase diagram of $\text{La}_{2-x}\text{A}_x\text{CuO}_4$ (A=Ba, Sr). The abbreviations are AF(antiferromagnet), SG(spin glass), SC(superconducting), T_N (Neel Temperature), T_C (critical temperature), I (insulator), M (metal), O (orthorhombic), and T (tetragonal).¹¹¹

$$H = -t \sum_{\langle i,j \rangle \sigma} (c_{i\sigma}^+ c_{j\sigma} + h.c.) + J \sum_{i,j} \left(S_i S_j - \frac{1}{4} n_i n_j \right) \quad 4.1$$

where $h.c.$ is the hermitian conjugate, and c is a projection fermion operator.¹¹² The accuracy with which this model describes high- T_C superconductivity is currently unknown due to difficulties in simulations of dynamical fermions in more than one dimension. However, it is known that the magnetic properties of these materials are described very well by the 2D Heisenberg model and also the relationship between the metal-insulator transition, the onset of superconductivity, and the hole doping of the system can be seen in the phase diagram shown in Figure 4.1.

In contrast, the silver (II) fluorides such as Cs_2AgF_4 possess CsF layers separating the ferromagnetic AgF_2 planes as opposed to the high- T_C materials such as La_2CuO_4 , which are composed of strongly antiferromagnetic CuO_2 planes separated by insulating intermediate layers. The goal is to replace a fraction of the cesium with an ion of equivalent size that has a different oxidation state. Therefore, Ba^{2+} which has a slightly smaller radius of 1.49 Å, compared to a 1.81 Å radius for Cs^+ , is predicted to be an effective dopant. In Cs_2AgF_4 , the monovalent Cs ion is easily replaced by a divalent dopant such as Ba^{2+} creating the series of compounds of the type $\text{Cs}_{2-x}\text{Ba}_x\text{AgF}_4$. This

substitution corresponds to *n*-type “electron” doping where the electron is the charge carrier and the oxidation state of silver will be less than 2.¹⁰⁹ In this type of doping, there is an extra electron due to the reduction of the transition metal center and the extra electron could potentially be excited into the conduction band. Therefore, the doping may lead to strongly modified magnetic behavior, provided that the dopant analogously affects the charge balance in the magnetic AgF₂ planes. If associated with an insulator to metal transition, this doped system may also exhibit superconductivity.

4.2 Data and results

4.2.1 X-ray diffraction

The X-ray diffraction data was first used to index the unit cell before Rietveld refinements were performed. The Crysfire powder indexing program was used to determine the unit cell.¹¹³ In order to obtain accurate unit cell parameters, the impurity peaks for AgF, CsF, BaF₂, and an additional unknown phase which was also seen in Cs₂AgF₄ were not included in the indexing. The unit cell with the highest figure of merit was a tetragonal lattice with the parameters $a = b = 4.5817 \text{ \AA}$ and $c = 14.19 \text{ \AA}$. Table 4.1 shows all of the possible lattice parameters generated by Crysfire. Next, the space group was determined using the Chekcell program which gave possible space groups of, *I4*, *I-4*, *I4/m*, *I422*, *I4mm*, *I-4m2*, and *I4/mmm*. The space group *I4/mmm* was chosen as the most plausible space group due to the results from the undoped Cs₂AgF₄ structural studies.

Rietveld refinements were performed on Cs_{1.9}Ba_{0.1}AgF₄ room temperature X-ray data assuming the space group *I4/mmm*. The lattice parameters for Cs_{1.9}Ba_{0.1}AgF₄ found after these refinements are $a = b = 4.579865(27) \text{ \AA}$ and $c = 14.18328(14) \text{ \AA}$. The (4+2) Ag octahedron has Ag-F bond lengths of 2.28993(1) Å and 2.13880(2) Å. Using the valence bond sum method from the previous chapter, the valence bond sum of the silver metal center is 1.815. The bond lengths in the Cs-F/Ba-F planes are 3.2399 Å and 3.2491 Å respectively. Table 4.2 shows a complete listing of the bond lengths calculated in the refinement. During the refinement, constraints were placed on the occupancies of Cs and Ba so that their total occupancy always equaled 1. Additional constraints were placed on

Table 4.1: Possible lattice parameters for Cs_{1.9}Ba_{0.1}AgF₄ generated by Crysfire.¹¹³

Merit	a/ Å	b/ Å	c/ Å	α	β	γ
271.5	4.5817	14.19	4.5817	90	90	90
196.29	4.5831	4.5831	14.1944	90	90	90
155.96	4.5834	4.5825	14.1943	90	90	90
154	4.583	4.583	14.1939	90	90	90
147.45	4.5832	4.5829	14.1944	90	90	90
100.43	4.5831	4.5831	14.1944	90	90	90
93.2	4.5831	4.5831	14.1955	90	90	90
79.18	4.5834	4.5825	14.1943	90	90	90
74.86	4.5832	4.5829	14.1944	90	90	90
74.2	14.196	4.5823	4.5836	90	90	90
68.2	5.585	14.195	3.2409	90	124.849	90
68.2	5.585	14.195	3.2409	90	124.849	90
66.6	5.5849	14.1952	3.2409	90	124.849	90
65.3	8.5202	12.9584	5.9227	90	95.683	90
64.2	4.5836	14.1953	3.2409	90	90.62	90
64.2	5.6422	14.1953	3.2409	90	125.676	90
64.2	5.6422	14.1953	3.2409	90	125.676	90
63.1	5.6422	14.1955	3.2409	90	125.674	90
59.5	4.6156	14.195	3.2636	90	96.781	90
53.9	5.1293	14.1948	3.627	90	116.678	90
52.3	4.6565	14.1951	3.2933	90	100.176	90
52.2	5.3288	14.1955	3.2638	90	120.674	90
50	4.7442	14.1961	3.6743	90	104.966	90
50	5.1966	14.1961	3.6743	90	118.119	90
50	4.7707	14.1953	3.6271	90	106.115	90
43.6	5.9609	14.1942	3.2647	90	129.744	90
43.5	5.2068	14.1964	3.2934	90	118.33	90
34.4	4.7824	14.1963	3.3814	90	106.57	90
32.5	4.9754	14.1962	3.4036	90	112.889	90
32.5	4.8131	14.1962	3.4036	90	107.763	90
32.4	4.9756	14.1965	3.4033	90	112.886	90
32.1	5.0083	14.1965	3.3815	90	113.753	90
20	14.488	6.4795	7.2424	90	101.534	90
19.5	14.8418	9.1627	14.4885	90	107.038	90
7.98	10.0403	10.0403	18.2053	90	90	90

Table 4.2: Cs_{1.9}Ba_{0.1}AgF₄ bond distances from the room temperature X-ray *I4/mmm* refinements.

Bond	Distance/ Å
Ag-Cs	3.82856(2)
Ag-F1	2.13880(2)
Ag-F2	2.28993(1)
Cs-Cs	4.57986(3)
	4.41950(2)
	4.08423(4)
Cs-F1	3.23990(2)
	2.91072(3)
Cs-F2	3.06823(2)
Ag-Ba	3.74290(2)
Cs-Ba	4.58285(3)
	4.53374(3)
	3.91876(4)
Ba-F2	2.96067(3)
Ba-F1	3.24905(2)
	3.08621(3)

the thermal parameters of Cs and Ba so that the values would remain equal to each other. The occupancies are listed in Table 4.3 and the thermal parameters are listed in Table 4.4. The refined occupancies give a stoichiometry of $\text{Cs}_{1.91}\text{Ba}_{0.104}\text{AgF}_{3.922}$ which indicates a loss of fluorine during the reaction. Using this stoichiometry, the oxidation state of silver was calculated to be 1.882.

A four phase refinement was performed using the room temperature X-ray data. The impurities identified were AgF, CsF, and BaF₂, with CsF and BaF₂ being two of the starting products; AgF could be present as a result of decomposition of the starting product AgF₂. The sample purity was 86.75%, with 6.095% AgF, 5.43% CsF and 1.72% BaF₂. An unknown phase is also present in the data, with peaks in the same positions observed in Cs₂AgF₄. This indicates perhaps a reaction occurring with the sample container, or an impurity in the starting material, most likely in AgF₂, as this starting product is only 98% pure. The refinement gave a χ^2 value of $\chi^2 = 9.166$. The ortep of the unit cell is shown in Figure 4.2, and the Rietveld refinement is shown in Figure 4.3.

4.2.2 Neutron diffraction

The background subtraction and absorbance correction were performed according to the procedures outlined in Chapter 2. Using the corrected data, Rietveld refinements using GSAS were used to construct a model of Cs_{1.9}Ba_{0.1}AgF₄. First the refinements were performed on the room temperature data using the space group *I4/mmm*. A split-site between Cs and Ba was used with the same constraints on their occupancies and thermal parameters used in the X-ray diffraction refinements. Without using these constraints, the refinement diverged. The refined lattice parameters are $a = b = 4.58094(9)$ Å and $c = 14.1858(4)$ Å. The central (4+2) octahedron has in-plane Ag-F distances of $2.29047(4)$ Å and axial Ag-F distances of 2.14036 Å. These distances are used in the valence bond sum to give a value of 1.81. The Cs-F distances are $3.24153(6)$ Å, while the Ba-F in-plane distances are $3.24096(9)$ Å. The complete list of bonds can be found in Table 4.5 with their comparison to the X-ray values, while the ADPs can be found in Table 4.6. The occupancies, which can be seen in Table 4.7, give

Table 4.3: Occupancies of $\text{Cs}_{1.9}\text{Ba}_{0.1}\text{AgF}_4$ from room temperature X-ray refinements.

Atom	Occupancy
Ag	0.9605
Cs	0.9499
Ba	0.0501
F1	0.9950
F2	0.8987

Table 4.4: ADPs from the room temperature X-ray $I4/mmm$ refinement for $\text{Cs}_{1.9}\text{Ba}_{0.1}\text{AgF}_4$.

Atom	$U_{ij} \cdot 100$					
	U_{11}	U_{22}	U_{33}	U_{12}	U_{13}	U_{23}
Ag	1.986	1.986	1.907	0.0	0.0	0.0
Cs	3.051	3.051	1.966	0.0	0.0	0.0
Ba	3.051	3.051	1.966	0.0	0.0	0.0
F1	3.188	3.189	2.006	0.0	0.0	0.0
F2	4.329	8.346	2.411	0.0	0.0	0.0

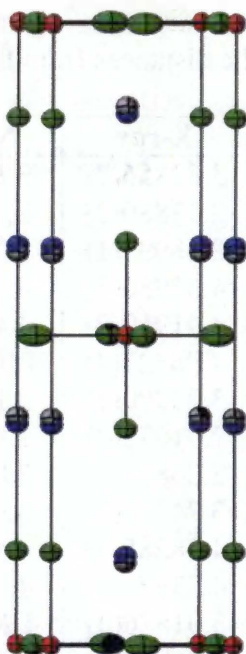


Figure 4.2: Ortep, or unit cell representation of $\text{Cs}_{1.9}\text{Ba}_{0.1}\text{AgF}_4$ from the room temperature X-ray refinements. A split site refinement was performed where the grey atoms are barium and the blue atoms are cesium

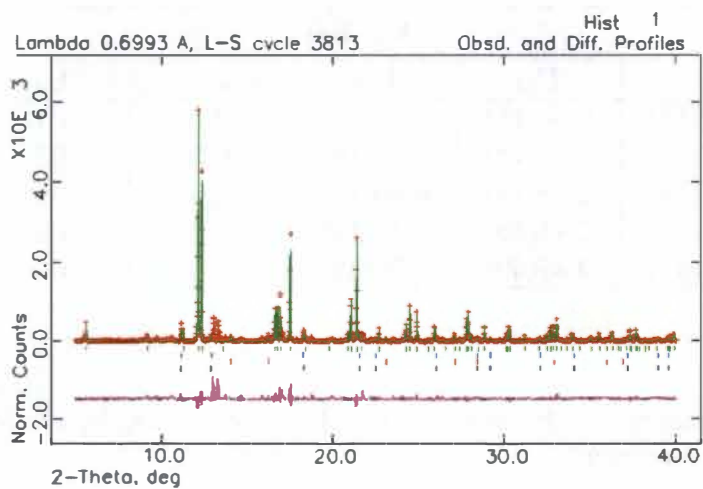


Figure 4.3: Four phase $I4/mmm$ refinement of the room temperature X-ray data for $\text{Cs}_{1.9}\text{Ba}_{0.1}\text{AgF}_4$. The green tickmarks represent the peak positions for $\text{Cs}_{1.9}\text{Ba}_{0.1}\text{AgF}_4$, the blue tickmarks are for CsF , red for AgF , and black for BaF_2 .

Table 4.5: $\text{Cs}_{1.9}\text{Ba}_{0.1}\text{AgF}_4$ bond distances from the room temperature neutron refinements with a comparison to the distances from the X-ray refinement.

Bond	X-ray	Neutron
Ag-Cs	3.82856(2)	3.81630(6)
Ag-F1	2.13880(2)	2.14036(6)
Ag-F2	2.28993(1)	2.29047(4)
Cs-Cs	4.57986(3)	4.58094(9)
	4.41950(2)	4.45413(8)
	4.08423(4)	4.03567(12)
Cs-F1	3.23990(2)	3.24153(6)
	2.91072(3)	2.93472(9)
Cs-F2	3.06823(2)	3.05252(5)
Ag-Ba	3.74290(2)	3.94210(6)
Cs-Ba	4.58285(3)	4.58665(9)
	4.53374(3)	4.30026(7)
	3.91876(4)	4.26453(12)
Ba-F2	2.96067(3)	3.20841(6)
Ba-F1	3.24905(2)	3.24096(9)
	3.07621(3)	2.70586(8)

Table 4.6: ADPs from the room temperature neutron $I4/mmm$ refinement for $\text{Cs}_{1.9}\text{Ba}_{0.1}\text{AgF}_4$.

$U_{ij} \cdot 100$						
Atom	U_{11}	U_{22}	U_{33}	U_{12}	U_{13}	U_{23}
Ag	0.94(15)	0.94(15)	1.20(21)	0.0	0.0	0.0
Cs	2.25(14)	2.25(14)	0.90(19)	0.0	0.0	0.0
Ba	2.25(14)	2.25(14)	0.90(19)	0.0	0.0	0.0
F1	2.41(16)	2.41(16)	1.21(19)	0.0	0.0	0.0
F2	2.71(32)	9.47(49)	2.20(22)	0.0	0.0	0.0

Table 4.7: Occupancies of the atoms in $\text{Cs}_{1.9}\text{Ba}_{0.1}\text{AgF}_4$ given by the room temperature $I4/mmm$ neutron refinement.

Atom	Occupancy
Ag	1.0234
Cs	0.954
Ba	0.046
F1	1.0041
F2	1.0013

a molecular formula of $\text{Cs}_{1.85}\text{Ba}_{0.082}\text{AgF}_{3.871}$, where the moles of Cs, Ba, and F are smaller than predicted due to unreacted starting products and other impurities.

Once again, a four phase refinement was performed with a sample phase purity of 87.96%. Impurities identified in the sample are AgF, CsF, and BaF_2 , with phase fractions of 0.0627, 0.0079, and 0.0497 respectively. The resulting χ^2 value is $\chi^2 = 2.612$ due to several unindexed peaks from the unidentified phase which is more visible in the X-ray diffraction data. The orpep of the model from these refinements can be seen in Figure 4.4 and the Rietveld refinement can be seen in Figure 4.5.

Room temperature refinements were also performed using the *Bbcm* space group. The lattice parameters from this refinement for this orthorhombic unit cell are $a = 6.4761(5)$ Å, $b = 6.4816(5)$ Å and $c = 14.1870(4)$ Å. The central octahedron has a (2+2+2) silver metal center due to distortion of the fluorines. The Ag-F bond lengths are 2.08028(12) Å and 2.50301(15) Å in the plane and 2.12007(6) Å along the *c* axis. These bond lengths were then used to calculate the valence bond sum of the silver center, which is 2.02. A complete list of bond lengths is given in Table 4.8. The ADPs for each atom, which are found in Table 4.9, are slightly abnormal, with an elongated planar F atom similar to the one seen in the *I4/mmm* refinement except that it is elongated along the *a* axis rather than the *b* axis. Also, there are a few unphysical thermal parameters in the off diagonal. Using the refined occupancies shown in Figure 4.10, the molecular formula is calculated as $\text{Cs}_{1.85}\text{Ba}_{0.1}\text{AgF}_{3.91}$ which once again indicates a loss of Cs and F to impurities during the reaction. This molecular formula is used to calculate the average oxidation state of silver which in this case is 1.95.

A four phase refinement was performed with CsF, AgF and BaF_2 as impurities with phase fractions of 0.0001, 0.0435, and 0.0001 respectively, which gives a sample purity of 95.63%. The χ^2 value of the *Bbcm* refinement does not improve significantly over the *I4/mmm* refinement, but stays almost the same with a value of $\chi^2 = 2.516$. As shown in Figure 4.6, the unidentified peaks of the *I4/mmm* phase are still unindexed in the *Bbcm* phase, indicating the presence of an unknown phase. The model of $\text{Cs}_{1.9}\text{Ba}_{0.1}\text{AgF}_4$ generated from this refinement can be seen in the orpep of Figure 4.7.

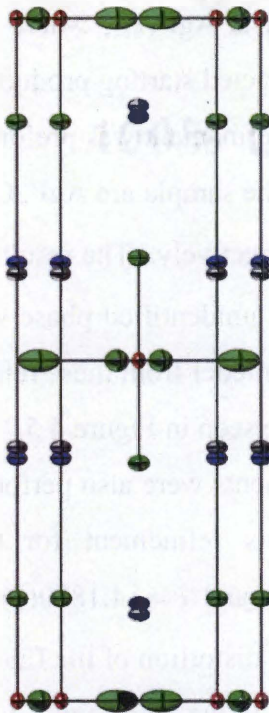


Figure 4.4: Model of $\text{Cs}_{1.9}\text{Ba}_{0.1}\text{AgF}_4$ based on the room temperature neutron refinements assuming an $I4/mmm$ space group.

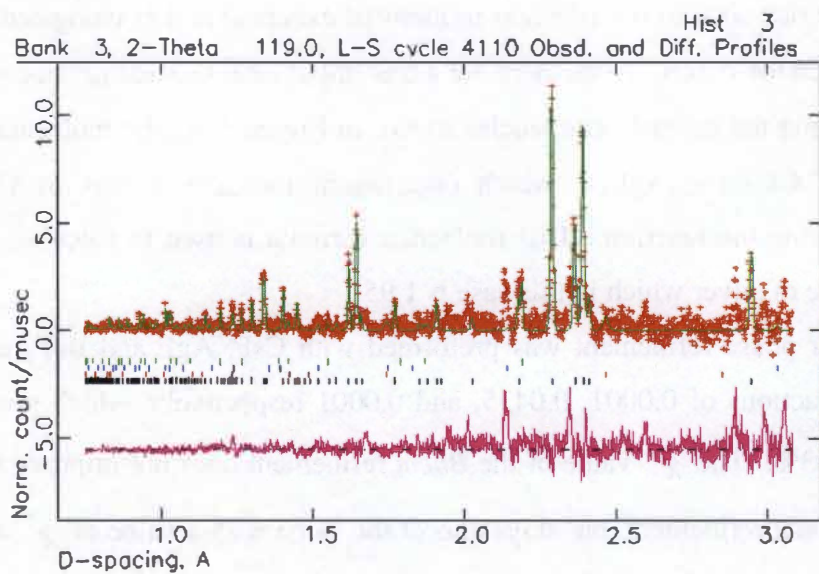


Figure 4.5: Rietveld refinement of the room temperature neutron data assuming an $I4/mmm$ space group. The black tickmarks represent $\text{Cs}_{1.9}\text{Ba}_{0.1}\text{AgF}_4$, the red AgF , the blue, CsF , and the green, BaF_2

Table 4.8: $\text{Cs}_{1.9}\text{Ba}_{0.1}\text{AgF}_4$ bond distances from the room temperature neutron refinements using the *Bbcm* space group.

Bond	Distance / Å
Ag-Cs	3.83537(22)
Ag-F1	2.12007(6)
Ag-F2	2.50301(15)
	2.08028(12)
Cs-Cs	4.58124(27)
	4.41027(20)
	4.0823(21)
Cs-F1	3.24155(26)
	3.23877(27)
	2.92232(8)
Cs-F2	3.13288(11)
	3.03182(10)
Ag-Ba	3.72318(24)
Cs-Ba	4.58621(27)
	4.55772(20)
	3.88885(11)
Ba-F1	3.25032(27)
	3.13573(9)
Ba-F2	2.99750(12)
	2.89171(11)

Table 4.9: ADPs from the room temperature neutron *Bbcm* refinement for $\text{Cs}_{1.9}\text{Ba}_{0.1}\text{AgF}_4$.

$U_{ij} \cdot 100$						
Atom	U_{11}	U_{22}	U_{33}	U_{12}	U_{13}	U_{23}
Ag	2.08	2.08	2.08	0	0.0	0.0
Cs	2.36	2.90	1.92	-0.88	0.0	0.0
Ba	2.36	2.90	1.92	-0.88	0.0	0.0
F1	1.58	2.53	1.39	-0.06	0.0	0.0
F2	6.72	3.04	2.98	2.21	0.0	0.0

Table 4.10: Occupancies of the atoms in $\text{Cs}_{1.9}\text{Ba}_{0.1}\text{AgF}_4$ given by the room temperature *Bbcm* neutron refinement.

Atom	Occupancy
Ag	1.0038
Cs	0.9472
Ba	0.0528
F1	0.9644
F2	0.9969

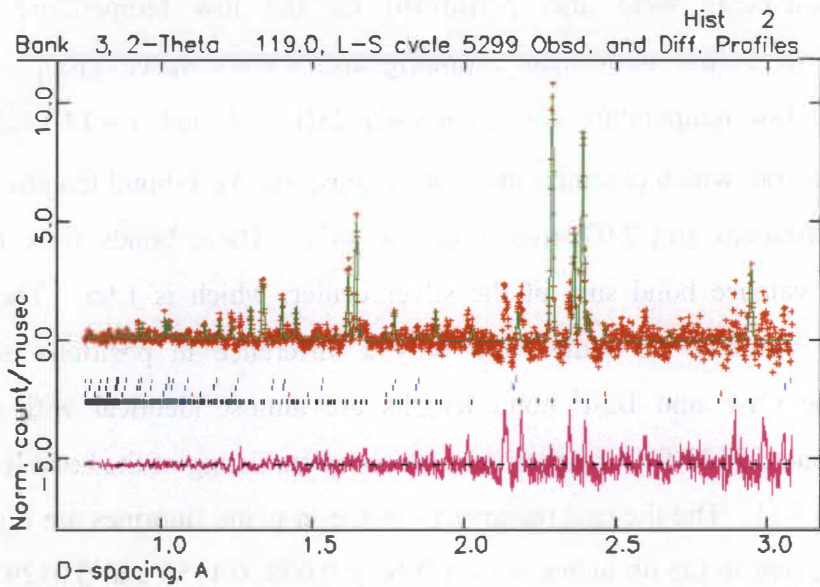


Figure 4.6: *Bbcm* Rietveld refinement of $\text{Cs}_{1.9}\text{Ba}_{0.1}\text{AgF}_4$ using the room temperature neutron data.

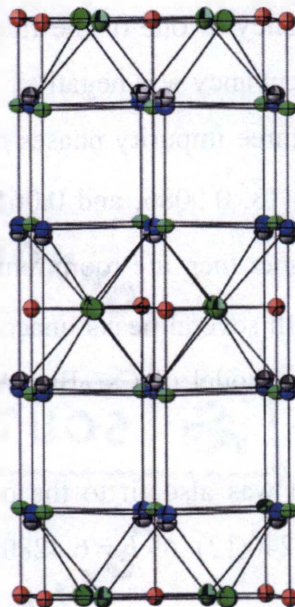


Figure 4.7: Model of $\text{Cs}_{1.9}\text{Ba}_{0.1}\text{AgF}_4$ based on the room temperature *Bbcm* refinements.

Rietveld refinements were also performed on the low temperature, 20K, data. Refinements were first performed assuming an $I4/mmm$ space group. The lattice parameters at low temperature are $a = b = 4.5428(12)$ Å and $c = 14.122(4)$ Å. The central octahedron, which contracts along the c axis, has Ag-F bond lengths of 2.2714(6) Å in-plane distances and 2.0994(6) Å on the axis. These bonds were then used to calculate the valence bond sum of the silver center, which is 1.96. The Cs and Ba positions are virtually the same, with only a difference in positions of 0.2235 Å. Therefore, the Cs-F and Ba-F bond lengths are almost identical with distances of 3.2138(9) Å and 3.2133(9) Å respectively. A complete listing of the bond lengths can be seen in Table 4.11. The thermal parameters of the in-plane fluorines are unusual in that they are elongated in the ab plane, with ADPs of 0.008, 0.1155 and 0.0129 for U_{11} , U_{22} and U_{33} respectively. A complete list of the thermal parameters for each atom type is given in Table 4.12. The refined occupancies give a molecular formula of $Cs_{1.86}$, $Ba_{0.1}AgF_{3.72}$ (Table 4.13). This stoichiometry gives an oxidation state for silver of 1.94.

A split site refinement was performed on the in-plane fluorine atoms with the abnormally large thermal displacements along the ab plane. The refinements started with each atom 0.1 Å apart. Constraints were placed so that the occupancy of each F was a combined value of 1 and equal thermal parameters. However, this refinement gave unphysical values with an occupancy of one of the fluorines possessing a value greater than 1 while the other fluorine occupancy was negative.

The refinement included three impurity phases of AgF, CsF and BaF₂ which are present in phase fractions of 0.0413, 0.0086, and 0.061 respectively. The χ^2 value is $\chi^2 = 3.066$, which is slightly higher than the room temperature χ^2 . The lower quality of the fit is clear in Figure 4.8 with several peaks unaccounted for, and missing intensity due to an inaccurate model. The model of $Cs_{1.9}Ba_{0.1}AgF_4$ can be seen in the ortep of Figure 4.9.

The low temperature data was also fit to the orthorhombic $Bbcm$ space group. The lattice parameters are $a = 6.4240(12)$ Å, $b = 6.4280(11)$ Å, and $c = 14.1256(6)$ Å.

Table 4.11: $\text{Cs}_{1.9}\text{Ba}_{0.1}\text{AgF}_4$ bond distances from the low temperature $I4/mmm$ refinements.

Bond	Distance/ Å
Ag-Cs	3.7789(8)
Ag-F1	2.0994(6)
Ag-F2	2.2714(6)
Cs-Cs	4.5428(12)
	4.4127(8)
	4.0353(11)
Cs-F1	3.2133(9)
	2.9438(8)
Cs-F2	3.0381(6)
Ag-Ba	3.9012(8)
Ba-F1	3.2133(9)
	2.7319(7)
Ba-F2	3.1718(6)

Table 4.12: ADPs from the low temperature neutron $I4/mmm$ refinement for $\text{Cs}_{1.9}\text{Ba}_{0.1}\text{AgF}_4$.

$U_{ij} \cdot 100$						
Atom	U_{11}	U_{22}	U_{33}	U_{12}	U_{13}	U_{23}
Ag	2.87	2.87	1.19	0.0	0.0	0.0
Cs	2.20	2.20	1.75	0.0	0.0	0.0
Ba	2.20	2.20	1.75	0.0	0.0	0.0
F1	1.23	1.23	2.24	0.0	0.0	0.0
F2	0.80	11.55	1.29	0.0	0.0	0.0

Table 4.13: Occupancies of the atoms in $\text{Cs}_{1.9}\text{Ba}_{0.1}\text{AgF}_4$ given by the low temperature $I4/mmm$ neutron refinement.

Atom	Occupancy
Ag	1.0038
Cs	0.9472
Ba	0.0528
F1	0.9644
F2	0.9969

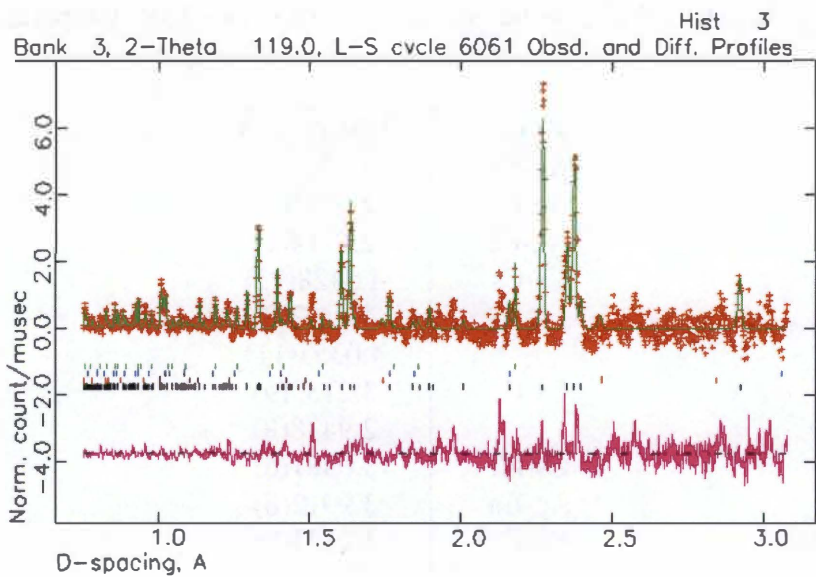


Figure 4.8: $I4/mmm$ Rietveld refinement for $Cs_{1.9}Ba_{0.1}AgF_4$ using the low temperature neutron data.

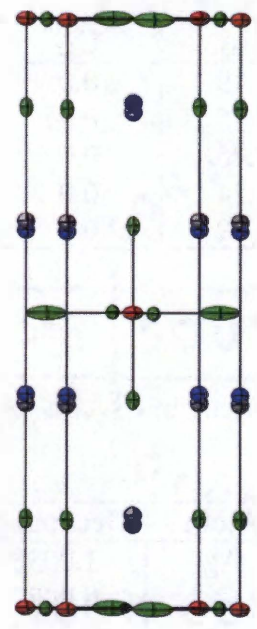


Figure 4.9: Model of $Cs_{1.9}Ba_{0.1}AgF_4$ based on the low temperature $I4/mmm$ neutron refinement.

The fluorine distortion that occurs in the *Bbcm* lattice results in a silver center octahedron that is contracted along the axis, and has two different bond lengths in the AgF_4 plane. The Ag-F distances in the octahedron are 2.11032(8) Å along the axis and the in-plane bond lengths are 2.14958(28) Å and 2.39502(31) Å. These bond lengths are used to find the valence bond sum of the silver center, which is 1.987. A split site was used for the Cs and Ba positions where their distance starts with a 0.1 Å difference and after the refinements, this difference remains essentially the same at 0.12754(1) Å. A complete list of the bond lengths can be seen in Table 4.14. For the split site refinement, the occupancy for Ba was originally 0.05 and for Cs, the occupancy began at 0.95. With the refined occupancies, the formula is $\text{Cs}_{1.86}\text{Ba}_{0.082}\text{AgF}_{3.99}$, indicating a loss of material to impurities. This stoichiometry gives an oxidation state of 1.976 for silver. A list of refined occupancies can be found in Table 4.15. The ADPs for the refinement were unphysical for the off diagonal values of some of the atoms. See Table 4.16 for the list of thermal parameters. See Figure 4.10 and 4.11 for the refinement and the unit cell ortep.

4.2.3 Magnetism

Susceptibility measurements were performed on $\text{Cs}_{1.9}\text{Ba}_{0.1}\text{AgF}_4$ in an applied field of 100 Oe. This data shows that $\text{Cs}_{1.9}\text{Ba}_{0.1}\text{AgF}_4$ displays typical Curie-Weiss behavior, which means it is a paramagnet at high temperatures, and a ferromagnet below the Curie temperature. It undergoes a magnetic transition at approximately 40K, and orders ferromagnetically below this temperature. Fits of this data will be performed at a future time. The magnetization is plotted as a function of temperature in Figure 4.12.

4.3 Discussion

As shown in the magnetization data, doping of Cs_2AgF_4 does considerably change the magnetic behavior of this material. In Cs_2AgF_4 , the transition temperature is approximately 15 K. At this temperature, ferromagnetic ordering occurs and the magnetization increases sharply at temperatures below the Curie temperature. However, in $\text{Cs}_{1.9}\text{Ba}_{0.1}\text{AgF}_4$, the transition temperature is approximately 40 K, which is a factor of 2.7 larger than the T_C undoped sample. At lower temperatures, the magnetization curve is also much broader than the data of Cs_2AgF_4 as shown in Figure 4.13.

Table 4.14: Cs_{1.9}Ba_{0.1}AgF₄ bond distances from the low temperature *Bbcm* refinements.

Bond	Distance/ Å
Ag-Cs	3.7885(5)
Ag-F1	2.11032(8)
Ag-F2	2.14958(28)
	2.39502(31)
Cs-Cs	4.5439(6)
	4.4318(4)
	4.01139(16)
Cs-F1	3.2157(6)
	2.94679(12)
Cs-F2	3.06391(23)
	3.00248(23)
Ag-Ba	3.8575(5)
Ba-F1	2.81925(11)
Ba-F2	3.2121(6)
	3.08914(22)

Table 4.15: Occupancies of the atoms in $\text{Cs}_{1.9}\text{Ba}_{0.1}\text{AgF}_4$ given by the low temperature *Bbcm* neutron refinement.

Atom	Occupancy
Ag	1.0217
Cs	0.9498
Ba	0.0502
F1	0.9964
F2	1.0418

Table 4.16: ADPs from the low temperature neutron *Bbcm* refinement for $\text{Cs}_{1.9}\text{Ba}_{0.1}\text{AgF}_4$.

$U_{ij} \cdot 100$						
Atom	U_{11}	U_{22}	U_{33}	U_{12}	U_{13}	U_{23}
Ag	3.43	2.58	1.37	-1.19	0.0	0.0
Cs	3.56	1.35	1.33	0.02	0.0	0.0
Ba	3.56	1.35	1.33	0.02	0.0	0.0
F1	2.77	1.12	2.23	-0.43	0.0	0.0
F2	4.70	6.16	2.05	4.67	0.0	0.0

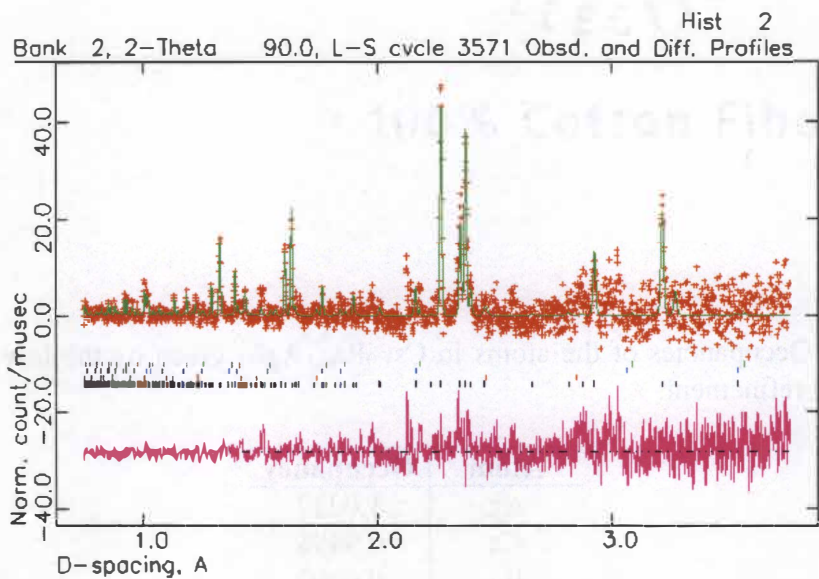


Figure 4.10: Four phase Rietveld refinement for $\text{Cs}_{1.9}\text{Ba}_{0.1}\text{AgF}_4$ using the *Bbcm* space group.

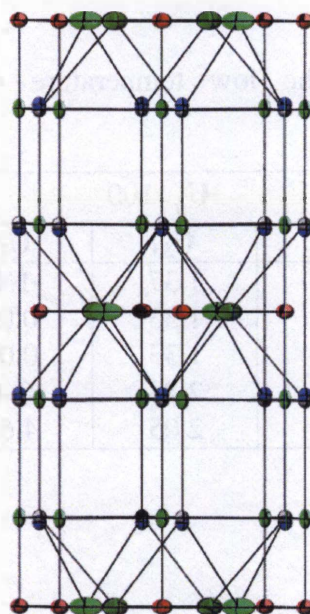


Figure 4.11: Ortep of $\text{Cs}_{1.9}\text{Ba}_{0.1}\text{AgF}_4$ using the *Bbcm* refinements.

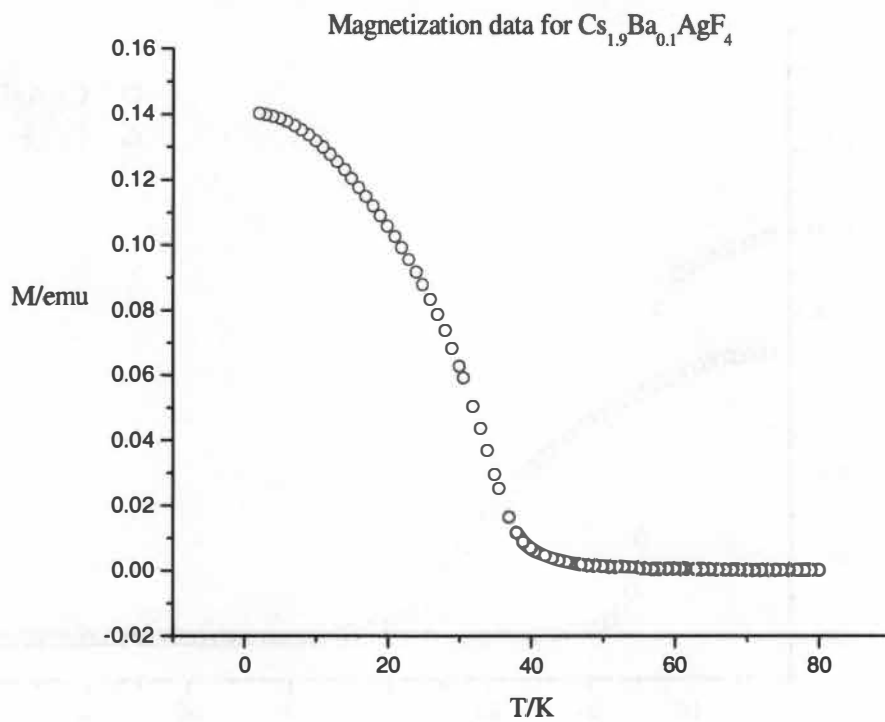


Figure 4.12: Magnetization of $\text{Cs}_{1.9}\text{Ba}_{0.1}\text{AgF}_4$ from versus temperature.

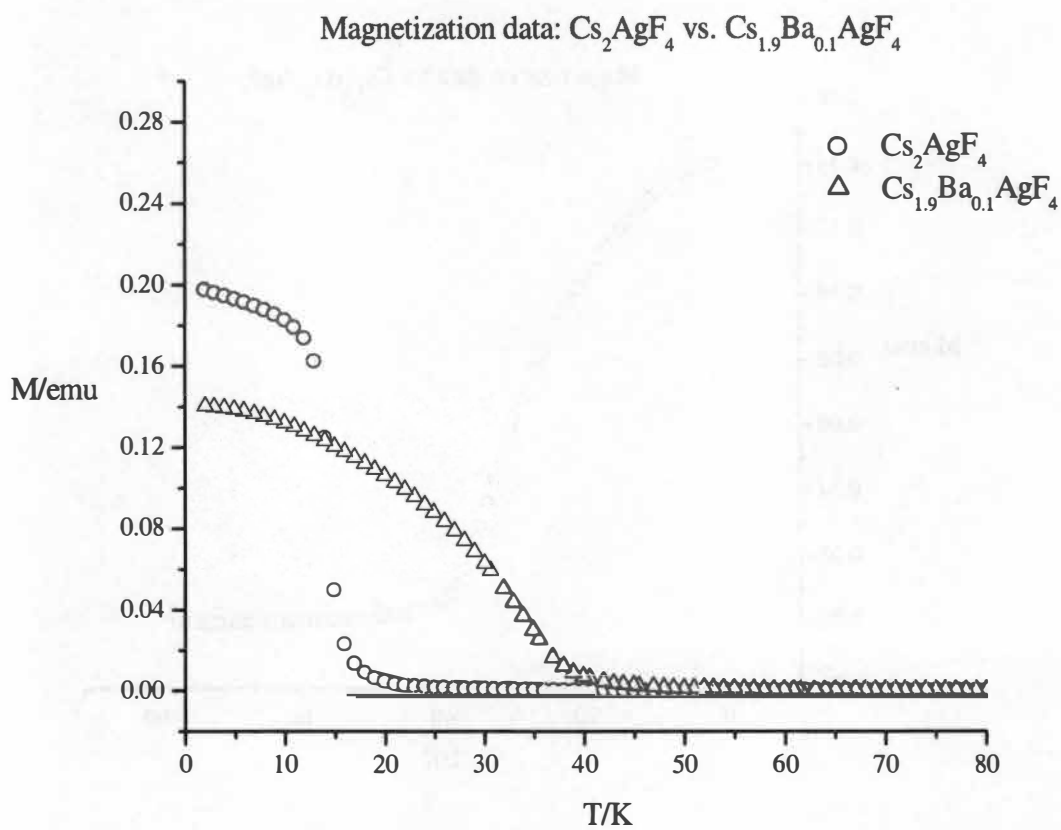


Figure 4.13: Magnetization curves comparing undoped Cs_2AgF_4 to doped $\text{Cs}_{1.9}\text{Ba}_{0.1}\text{AgF}_4$.

Table 4.17: Comparison of Cs_2AgF_4 , and $\text{Cs}_{1.9}\text{Ba}_{0.1}\text{AgF}_4$ lattice parameters assuming the space group $I4/mmm$.

Lattice	Cs_2AgF_4	$\text{Cs}_{1.9}\text{Ba}_{0.1}\text{AgF}_4$
a	4.5905(18)	4.58094(9)
b	4.5905(18)	4.58094(9)
c	14.213(6)	14.1858(4)

One viable explanation for such an effect could be due to an increased anisotropy in the layers of the unit cell and also a weaker magnetism between planes. As mentioned in previous chapters, a pure 2D ferromagnet theoretically orders at 0K; ordering temperatures above 0K are due to anisotropies or fluctuations in the magnetic material.⁸⁹ The defect results in a lower activation energy for the spins to align in their domain.¹⁰⁹ Evidence of an increased anisotropy is seen by looking at the crystal structure of $\text{Cs}_{1.9}\text{Ba}_{0.1}\text{AgF}_4$. Compared to Cs_2AgF_4 , the lattice contracts significantly along the c axis and contracts a small amount in the ab plane. The fact that the unit cell contracts when it is doped could possibly result from the replacement of cesium (which has an ionic radius of 1.81 Å), by barium, an ion with a smaller radius of 1.49 Å. As shown in Table 4.17, the unit cell is 14.1858(4) Å along the c axis, whereas in Cs_2AgF_4 , c is 14.213(6) Å, indicating a change of 0.2%. Although this change is quite small, it could potentially increase the anisotropy enough to raise the magnetic transition temperature. Doping Cs_2AgF_4 with Ba^{2+} could increase the anisotropy in several ways. Firstly, the crystal structure becomes structurally anisotropic due to one in twenty cesium ions being replaced with a slightly smaller barium ion. This exchange could place an additional strain or stress on the material which could in turn alter the magnetic properties, making it easier for the spins to overcome thermal fluctuations and align at a higher temperature. Secondly, the electronic structure also increases the anisotropy because one in twenty of the monovalent cesium is being replaced by divalent barium causing the oxidation state of a percentage of the silver ions to change from +2 to +1. The evidence for the change in oxidation state of silver is shown in the valence bond sum, which ranges from 1.81 to 2.02 depending on the refinement, with only one calculated valence bond sum over 2.00.

By doping Cs_2AgF_4 with a small amount of Ba^{2+} , only the transition temperature was altered, not the type of magnetic behavior as was seen in the well studied high T_C material La_2CuO_4 . Cs_2AgF_4 is compared to La_2CuO_4 in an attempt to understand reason why this silver (II) fluoride material behaves the way it does.

As discussed in the previous chapter, La_2CuO_4 is orthorhombic as a result of a slightly tilted CuO_6 octahedron. Several experiments have shown that there is a dopant and temperature induced structural phase transitions from orthorhombic to tetragonal structure.^{77,78,114-117} For example, a powder diffraction study by Axe et. al. finds that for a narrow range of Ba concentrations in $\text{La}_{2-x}\text{Ba}_x\text{CuO}_4$, beyond the expected high temperature tetragonal (HTT) transition to a low temperature orthogonal (LTO) phase, there is also another phase transition to a low temperature tetragonal (LTT) phase upon further cooling.¹¹⁴ The LTT phase is distinguished by the tilt angle of the CuO_6 octahedra. Up to $x=0.15$ the tilt angle decreases as x is increased, but when x is larger than 0.15, the local tilt remains but disorders over a long range, giving rise to the average HTT structure.⁷⁸ This low temperature transition perhaps influences the superconductivity, which is most pronounced when $x \approx 1/8$.¹¹⁸

Similar behavior is also observed when Sr is the dopant. Strontium is substituted at the La^{3+} site and induces atomic distortions. Sr donates a hole and also considerably distorts the neighboring oxygen environment by disordering the CuO_6 octahedra from their periodic structure.⁷⁷ As in the barium doped copper oxides mentioned previously, on average the octahedra are not tilted at high temperatures, but locally, the tilt can still be identified above the transition temperature.^{77,78,116}

As just mentioned, some studies suggest that the tilting of the CuO_6 octahedron is may play a role in the superconductivity of certain Ba^{2+} concentrations. Figure 4.14 shows the unit cell of $\text{La}_{1.83}\text{Ba}_{0.17}\text{CuO}_4$, which has a Bragg structure represented by the tetragonal $I4/mmm$ space group. This figure shows that the anisotropic thermal ellipsoids of both oxygen atoms are rather unusual. The O(2) equatorial oxygen has an unusually large transverse amplitude and is actually 3% closer to La than to the Cu and the O(1) apical oxygens possess a large vertical amplitude of its thermal parameter.^{107,119} It is

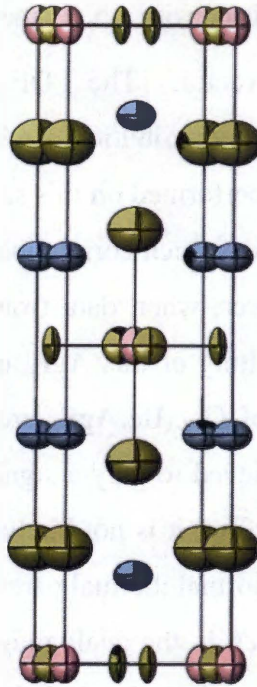


Figure 4.14: Ortep of La_{1.83}Sr_{0.17}CuO₄. The green atoms represent oxygen, the blue atoms represent La/Sr and the pink atoms represent copper.

believed that a strong electron-phonon coupling occurs at the equatorial oxygen atoms, which may in turn, lead to the superconducting effect displayed by these materials.

By looking at the properties of La_{2-x}A_xCuO₄ (A=Ba, Sr), it is clear why Cs_{1.9}Ba_{0.1}AgF₄ does not share the same superconducting behavior as the copper oxides described above. Firstly, in Cs₂AgF₄ and Cs_{1.9}Ba_{0.1}AgF₄, the average Bragg structure shows that the central AgF₆ octahedron does not tilt as in La₂CuO₄ and some of its doped derivatives. In order to determine if the AgF₆ octahedron may tilt, Pair Distribution Function analysis (PDF) must be performed to determine the local order. PDF analysis is able to determine the local structure by examining the diffuse scattering caused by deviations in the average structure and contains information about two body interactions.^{120,121} The PDF is obtained by taking the Fourier transform of the normalized $S(Q)$

$$G(r) = 4\pi r [\rho(r) - \rho_0] = \frac{2}{\pi} \int_0^{\infty} Q [S(Q) - 1] \sin(Qr) dQ \quad 4.2$$

where $\rho(r)$ is the microscopic pair density, ρ_0 is the average number density, and Q is the magnitude of the scattering vector. The PDF contains both Bragg and diffuse scattering, from which a bond length distribution can be determined between all atom.¹²¹ This type of analysis could not be performed on this sample due to the impurities because it would not be possible to determine which correlations were from the sample and which were from the impurities. However, when data from a pure sample is obtained, it is believed that there would be no tilting of this AgF_6 octahedron. The reason for this is because the magnetic properties of $\text{Cs}_{2-x}\text{Ba}_x\text{AgF}_4$ are so different from the lanthanum copper oxides where the tilt is believed to play a significant role in the superconducting behavior of these materials. Therefore, it is not likely that the effect will be seen in this silver fluoride series. Also, the abnormal thermal parameters seen in the oxygen atoms of $\text{La}_{2-x}\text{A}_x\text{CuO}_4$ ($\text{A}=\text{Ba},\text{Sr}$) are not seen in the analogous fluorine atoms in $\text{Cs}_{1.9}\text{Ba}_{0.1}\text{AgF}_4$. As a result, the electron-phonon coupling that is believed to occur through the oxygen atoms in the copper oxides, most likely does not occur in the silver fluoride comparison. As electron-phonon interactions are a possible origin for superconducting behavior, this would be expected in a material such as $\text{Cs}_{1.9}\text{Ba}_{0.1}\text{AgF}_4$, which does not show superconducting properties as does the copper oxides used for comparison.

4.4 Conclusion

Through this preliminary study on $\text{Cs}_{1.9}\text{Ba}_{0.1}\text{AgF}_4$, it is evident that Ba^{2+} doping of Cs_2AgF_4 does indeed significantly alter the magnetic properties, however, it does not induce superconductivity. The Curie temperature at which ferromagnetic ordering occurs increases from $\sim 15\text{K}$ to $\sim 40\text{K}$ under doping, but the structure of the material remains unchanged with the only significant modification being a lattice contraction along the c axis.

Although this study is not complete, it shows promising results that can lead to a complete phase diagram of $\text{Cs}_{2-x}\text{Ba}_x\text{AgF}_4$. Diffraction data has been collected from $\text{Cs}_{1.8}\text{Ba}_{0.2}\text{AgF}_4$ and $\text{Cs}_{1.7}\text{Ba}_{0.3}\text{AgF}_4$, both of which have additional peaks that indicate a lowering of symmetry. Upon peak indexing, the possible lattice parameters with the highest figure of merit are orthorhombic, which is direct evidence of a tetragonal to

orthorhombic transition that is dependent on doping concentration. The space group is yet to be determined. These results, however, do indicate that an interesting structural change takes place which merits further investigation in a future, more detailed characterization of this new class of materials.

Faint, illegible text at the top of the page, possibly bleed-through from the reverse side.

References

- (1) Orchard, A. F. *Magnetochemistry*; Oxford University Press, 2003.
- (2) Parasnis, D. S. *Magnetism: From Lodestone to Polar Wandering*, 1961.
- (3) Buschow, K. H. J., DeBoer, F.R. *Physics of magnetism and magnetic materials*, 2003.
- (4) Crangle, J. *Solid State Magnetism*, 1991.
- (5) Earnshaw, A. *Introduction to Magnetochemistry*, 1968.
- (6) Figgis, B. N., Hitchman, M. A. *Ligand Field Theory and its Applications*, 2000.
- (7) Levine, I., N. *Quantum Chemistry*; Prentice Hall, 1991.
- (8) Levy, L.-P. *Magnetism and Superconductivity*, 2000.
- (9) Ratner, M. A., Schatz, G. C. *Introduction to Quantum Mechanics in Chemistry*, 2001.
- (10) Selwood, P. W. *Magnetochemistry*, 1956.
- (11) van Vleck, J. H. *Theory of Electric and Magnetic Susceptibilities*, 1932.
- (12) Merzbacher, E. *Quantum Mechanics*; 3rd. ed., 1998.
- (13) Van Vleck, J. H. "Valence strength and the magnetism of complex salts" *Journal of Chemical Physics* **1935**, *3*, 807-813.
- (14) West, A., R. *Solid State Chemistry and its Applications*, 1984.
- (15) Jahn, H. A., Teller, E. "Stability of polyatomic molecules in degenerate electronic states. I. Orbital degeneracy" *Proc. Roy. Soc. (London)* **1937**, *A161*, 220-235.
- (16) Albright, T. A., Burdett, J. K., Whangbo, M. H.. *Orbital Interactions in Chemistry*, 1985.
- (17) Pearson, R. G. "Jahn-Teller Effects" *Proceedings of the National Academy of Sciences of the United States of America* **1975**, *72*, 2104-2106.
- (18) Grochala, W., Hoffmann, R. "Real and hypothetical intermediate-valence AgII/AgIII and AgII/AgI fluorine systems as potential superconductors" *Angewandte Chemie, International Edition* **2001**, *40*, 2742-2781.
- (19) Bednorz, J. G., Mueller, K. A. "Possible high T_C superconductivity in the barium-lanthanum-copper-oxide system" *Zeitschrift fuer Physik B: Condensed Matter* **1986**, *64*, 189-193.

- (20) Bednorz, J. G., Mueller, K. A. "Perovskite-type oxides - the new approach to high T_C superconductivity" *Prix Nobel* **1988**, 65-98.
- (21) Housecroft, C. E. *Coordination Chemistry Reviews* "Silver" **1992**, *115*, 141-161.
- (22) Muller-Buschbaum, H. "On the crystal chemistry of oxoargentates and silver oxometallates" *Zeitschrift fuer Anorganische und Allgemeine Chemie* **2004**, *630*, 2125-2175.
- (23) Bartlett, N., Lucier, G., Shen, C., Casteel, W. J., Jr., Chacon, L., Munzenberg, J., Zemva, B. "The oxidizing properties of cationic high oxidation state transition-element fluoro species" *Journal of Fluorine Chemistry* **1995**, *71*, 163-164.
- (24) Hagiwara, R., Hollander, F., Maines, C., Bartlett, N. "The crystal structure of $[Ag(XeF_2)_2]AsF_6$ formed in the oxidation of xenon by silver(II) fluoride hexafluoroarsenate" *European Journal of Solid State and Inorganic Chemistry* **1991**, *28*, 855-866.
- (25) Zemva, B., Hagiwara, R., Casteel, W. J., Jr., Lutar, K., Jesih, A.; Bartlett, N. "Spontaneous oxidation of xenon to Xe(II) by cationic Ag(II) in anhydrous hydrogen fluoride solutions" *Journal of the American Chemical Society* **1990**, *112*, 4846-4849.
- (26) Lucier, G., Muenzenberg, J., Casteel, W. J., Jr., Bartlett, N. "Preparation and Structural and Magnetic Properties of $AgF+MF_6^-$ ($M = Ir, Ru, Sb, Bi$) and $Ag^{2+}(BiF_6^-)^2-$ ". *Inorganic Chemistry* **1995**, *34*, 2692-2698.
- (27) Lucier, G., Shen, C., Casteel, W. J., Jr.; Chacon, L., Bartlett, N. "Some chemistry of high oxidation state transition metal fluorides in anhydrous HF" *Journal of Fluorine Chemistry* **1995**, *72*, 157-163.
- (28) Lucier, G. M., Whalen, J. M., Bartlett, N. "High yield room temperature syntheses of $KAgF_4$ and AgF_3 and the preparation and unit cell of $LiAgF_4$ " *Journal of Fluorine Chemistry* **1998**, *89*, 101-104.
- (29) Shen, C., Zemva, B., Lucier, G. M., Graudejus, O., Allman, J. A., Bartlett, N. "Disproportionation of Ag(II) to Ag(I) and Ag(III) in Fluoride Systems and Syntheses and Structures of $(AgF^+)_2AgF_4^-MF_6^-$ Salts ($M = As, Sb, Pt, Au, Ru$)" *Inorganic Chemistry* **1999**, *38*, 4570-4577.

- (30) Zemva, B., Lutar, K., Jesih, A., Casteel, W. J., Jr., Bartlett, N. "A general method for the synthesis of polymeric binary fluorides exemplified by AgF_3 , NiF_4 , RuF_4 , and OsF_4 " *Journal of the Chemical Society, Chemical Communications* **1989**, 346-347.
- (31) Zemva, B., Lutar, K., Jesih, A., Casteel, W. J., Jr., Wilkinson, A. P., Cox, D. E., Von Dreele, R. B., Borrmann, H., Bartlett, N. "Silver trifluoride: preparation, crystal structure, some properties, and comparison with AuF_3 " *Journal of the American Chemical Society* **1991**, *113*, 4192-4198.
- (32) Allen, G. C., McMeeking, R. F., Hoppe, R., Mueller, B. "Tetragonally distorted silver (II) complex in fluorides" *Journal of the Chemical Society, Chemical Communications* **1972**, 291-292.
- (33) Hoppe, R., Homann, R. "Trivalent silver: $\text{Cs}_2\text{K}[\text{AgF}_6]$ " *Naturwissenschaften* **1966**, *53*, 501.
- (34) Hoppe, R., Homann, R. "Fluoro complexes with silver and gold" *Zeitschrift fuer Anorganische und Allgemeine Chemie* **1970**, *379*, 193-198.
- (35) Hoppe, R., Muller, B. "Divalent silver: silver lead fluoride (AgPbF_6), silver tin fluoride (AgSnF_6), and silver zirconium fluoride (AgZnF_6)" *Naturwissenschaften* **1969**, *56*, 35.
- (36) Mueller, B., Hoppe, R. "Fluorides with divalent silver. Silver(II) hexafluorometallates, $\text{Ag}[\text{MF}_6]$, with M = germanium, tin, lead, titanium, zirconium, hafnium, rhodium, palladium, and platinum" *Zeitschrift fuer Anorganische und Allgemeine Chemie* **1972**, *392*, 37-41.
- (37) Mueller, B., Hoppe, R. "New fluorides with divalent silver : $\text{M(I)Ag(II)M(III)F}_6$ with M(I) = potassium, rubidium, and cesium and M(III) = aluminum, gallium, indium, thallium, scandium, iron, and cobalt" *Zeitschrift fuer Anorganische und Allgemeine Chemie* **1973**, *395*, 239-248.
- (38) Odenthal, R. H., Paus, D., Hoppe, R. "Magnetochemistry of divalent silver. New fluoroargentates(II). Dicesium, dirubidium, and dipotassium tetrafluoroargentates" *Zeitschrift fuer Anorganische und Allgemeine Chemie* **1974**, *407*, 144-150.

(39) Paus, D., Hoppe, R. "Rubidium nickel chromium hexafluoride type. VI. The magnetic behavior of cesium silver scandium hexafluoride, cesium copper indium hexafluoride, cesium copper gallium hexafluoride, and cesium copper zinc gallium hexafluoride ($\text{CsCu}_{1-x}\text{Zn}_x\text{GaF}_6$)" *Zeitschrift fuer Anorganische und Allgemeine Chemie* **1976**, 426, 83-94.

(40) Setter, J., Hoppe, R. "Hexafluoroindates(III): A_2TlInF_6 (A = rubidium, cesium), $(\text{RbTl})\text{BInF}_6$ (B = sodium, silver, potassium), and A_2AgInF_6 (A = rubidium, thallium, cesium)" *Zeitschrift fuer Anorganische und Allgemeine Chemie* **1976**, 423, 125-132.

(41) Fischer, R., Mueller, B. G. "Crystal structure of $\text{AgIIF}[\text{AgIIIF}_4]$ " *Zeitschrift fuer Anorganische und Allgemeine Chemie* **2002**, 628, 2592-2596.

(42) Graudejus, O., Mueller, B. G. " Ag^{2+} in trigonal bipyramidal surrounding new fluorides with divalent silver $\text{AgMII3MIV}_3\text{F}_{20}$ (MII = Cd, Ca, Hg; MIV = Zr, Hf)" *Zeitschrift fuer Anorganische und Allgemeine Chemie* **1996**, 622, 1549-1556.

(43) Mueller, B. G. "High pressure modifications of palladium difluoride and silver difluoride" *Naturwissenschaften* **1979**, 66, 519-520.

(44) Mueller, B. G. "Structure of quaternary fluorides with divalent silver: $\text{M(I)Ag(II)M(III)F}_6$ with M(I)=rubidium or cesium and M(III)=aluminum, gallium, or iron" *Journal of Fluorine Chemistry* **1981**, 17, 317-329.

(45) Mueller, B. G. "New complex fluorides with silver (2+) and palladium (2+): $\text{NaM(II)Zr}_2\text{F}_{11}$ (MII=Ag,Pd) and silver palladium zirconium fluoride ($\text{AgPdZr}_2\text{F}_{11}$)" *Zeitschrift fuer Anorganische und Allgemeine Chemie* **1987**, 553, 205-211.

(46) Mueller, B. G. "Fluorides with copper, silver, gold, and palladium" *Angewandte Chemie* **1987**, 99, 1120-1135.

(47) Mueller, B. G. "Ternary fluorides of divalent silver: $\text{Ag}(\text{MF}_6)_2$ (M=niobium, tantalum)" *Angewandte Chemie* **1987**, 99, 685-686.

(48) Mueller, B. G. "New ternary silver (II) fluorides: $\text{Ag(II)}_3\text{M(IV)}_2\text{F}_{14}$ (M(IV)= zirconium, hafnium)" *Zeitschrift fuer Anorganische und Allgemeine Chemie* **1987**, 553, 196-204.

- (49) Eujen, R., Zemva, B. "NMR spectra of AgF_4^- ion" *Journal of Fluorine Chemistry* **1999**, *99*, 139-140.
- (50) Goryunkov, A. A., Markov, V. Y., Boltalina, O. V., Zemva, B., Abdul-Sada, A. K., Taylor, R. "Reaction of silver(I) and -(II) fluorides with C_{60} : thermodynamic control over fluorination level" *Journal of Fluorine Chemistry* **2001**, *112*, 191-196.
- (51) Grochala, W., Egdell, R. G., Edwards, P. P., Mazej, Z., Zemva, B. "On the covalency of silver-fluoride bonds in compounds of silver (I), silver (II), and silver (III)" *ChemPhysChem* **2003**, *4*, 997-1001.
- (52) Jesih, A., Lutar, K., Zemva, B., Bachmann, B., Becker, S., Mueller, B. G., Hoppe, R. "Single crystal investigations on silver (2+) fluoride" *Zeitschrift fuer Anorganische und Allgemeine Chemie* **1990**, *588*, 77-83.
- (53) Lutar, K., Jesih, A., Zemva, B. "On the synthesis of xenon(VI) fluoroargentate(III)" *Revue de Chimie Minerale* **1986**, *23*, 565-571.
- (54) Nakajima, T., Matsuo, Y., Zemva, B., Jesih, A. "Synthesis of fluorine-graphite intercalation compounds by elemental fluorine and high oxidation-state transition-metal fluorides" *Carbon* **1996**, *34*, 1595-1598.
- (55) Zemva, B., Lutar, K., Jesih, A. "Higher silver fluorides: synthesis, structure and oxidation capabilities" *Zbornik Referatov s Posvetovanja Slovenski Kemijski Dnevi, Maribor, Slovenia, Sept. 18-19, 1997* **1997**, 440-445.
- (56) Pearson, R. G. "Hard and soft acids and bases" *Journal of the American Chemical Society* **1963**, *85*, 3533-3539.
- (57) Botti, A., Bruni, F., Ricci, M. A., Soper, A. K. "Neutron diffraction study of high density supercritical water" *Journal of Chemical Physics* **1998**, *109*, 3180-3184.
- (58) Soper, A. K. "The quest for the structure of water and aqueous solutions" *Journal of Physics: Condensed Matter* **1997**, *9*, 2717-2730.
- (59) Soper, A. K. "The radial distribution functions of water and ice from 220K to 673K and at pressures up to 400 MPa" *Chemical Physics* **2000**, *258*, 121-137.
- (60) Soper, A. K. "Probing the structure of water around biological molecules: concepts, constructs, and consequences" *Physica B: Condensed Matter (Amsterdam)* **2000**, *276-278*, 12-16.

- (61) Deraman, M., Dore, J. C., Powles, J. G., Holloway, J. H., Chieux, P. "Structural studies of liquid hydrogen fluoride by neutron diffraction. I. Liquid deuterium fluoride at 293K" *Molecular Physics* **1985**, *55*, 1351-1367.
- (62) McLain, S. E., Benmore, C. J., Siewenie, J. E., Urquidi, J., Turner, J. F. C. "On the structure of liquid hydrogen fluoride" *Angewandte Chemie, International Edition* **2004**, *43*, 1952-1955.
- (63) Wells, A. F. *Structural Inorganic Chemistry*; 5th edition ed., 1983.
- (64) Pynn, R. *Neutron Scattering: A Primer*.
- (65) Guinier, A. *X-ray diffraction in crystals, imperfect crystals, and amorphous bodies*, 1994.
- (66) Hubbell, J. H., Veigele, W. J., Briggs, E. A., Brown, R. T., Cromer, D. T., Howerton, R. J. "Atomic form factors, incoherent scattering functions, and photon scattering cross sections" *Journal of Physical and Chemical Reference Data* **1975**, *4*, 471-538.
- (67) Squires, G. L. *Introduction to the theory of thermal neutron scattering*, 1978.
- (68) Rietveld, H. M. "Line profiles of neutron powder diffraction peaks for structure refinement" *Acta Crystallographica* **1967**, *22*, 151-152.
- (69) Rietveld, H. M. "Profile refinement method for nuclear and magnetic structures" *Journal of Applied Crystallography* **1969**, *2*, 65-71.
- (70) Young, R. A. *The Rietveld Method*, 1993.
- (71) Larson, A. C.; von Dreele, R. B. Los Alamos Laboratory Report LAUR 86-748.
- (72) Lalignat, Y., Le Bail, A., Ferey, G., Hervieu, M., Raveau, B., Wilkinson, A., Cheetham, A. K. "Synthesis and ab-initio structure determination from x-ray powder data of barium palladium oxide (Ba_2PdO_3) with sevenfold coordinated barium(2+). Structural correlations with K_2NiF_4 and Ba_2NiF_6 " *European Journal of Solid State and Inorganic Chemistry* **1988**, *25*, 237-247.

(73) Le Bail, A., Duroy, H., Fourquet, J. L. "The ab-initio structure determination of lithium antimony tungstate (LiSbWO_6) by x-ray powder diffraction" *Materials Research Bulletin* **1988**, *23*, 447-452.

(74) Peterson, P. F., Gutmann, M., Proffen, T., Billinge, S. J. L. "PDFgetN: a user friendly program to extract the total scattering structure factor and the pair distribution function from neutron powder diffraction data" *Journal of Applied Crystallography* **2000**, *33*, 1192.

(75) Boni, P., Axe, J. D., Shirane, G., Birgeneau, R. J., Gabbe, D. R., Jenssen, H. P., Kaster, M. A., Peters, C. J., Picone, P. J., Thurston, T. R. "Lattice instability and soft phonons in single crystal $\text{La}_{2-x}\text{Sr}_x\text{CuO}_4$ " *Phys. Rev. B* **1988**, *38*, 185-194.

(76) Fleming, R. N., Batlogg, B., Cava, R. J., Rietman, E. A. "Temperature and composition dependence of the tetragonal-orthorhombic distortion in $\text{La}_{2-x}\text{Sr}_x\text{CuO}_4$ " *Phys. Rev. B* **1987**, *35*, 7191-7194.

(77) Haskel, D., Stern, E. A., Hinks, D. G., Mitchell, A. W.; Jorgensen, J. D. "Altered Sr environment in $\text{La}_{2-x}\text{Sr}_x\text{CuO}_4$ " *Physical Review B: Condensed Matter* **1997**, *56*, R521-R524.

(78) Haskel, D., Stern, E. A., Hinks, D. G., Mitchell, A. W., Jorgenson, J. D., Budnick, J. I. "Dopant and temperature induced structural phase transition in $\text{La}_{2-x}\text{Sr}_x\text{CuO}_4$ " *Phys. Rev. Lett.* **1996**, *76*, 439.

(79) Rao, C. N. R., Ganguli, A. K. "Structural aspects of superconducting cuprates" *Acta Cryst.* **1995**, *B51*, 604-618.

(80) Ruddlesden, S. N., Popper, P. "New compounds of the K_2NiF_4 -type" *Acta Cryst.* **1957**, *10*, 538-539.

(81) Ruddlesden, S. N., Popper, P. "The compound $\text{Sr}_3\text{Ti}_2\text{O}_7$ and its structure" *Acta Cryst.* **1958**, *11*, 54-55.

(82) Greenblatt, M. "Ruddlesden-Popper $\text{Ln}_{n+1}\text{Ni}_n\text{O}_{3n+1}$ nickelates: structure and properties" *Current Opinion in Solid State & Materials Science* **1997**, *2*, 174-183.

(83) Park, C., Snyder, R. L. "Perovskite stacking in the structures of the high temperature cuprate superconductors" *Applied Superconductivity* **1995**, *3*, 73-83.

- (84) Baker, G. A., Gilbert, H. E., Eve, J., Rushbrooke, G. S. "On the field-dependent susceptibility of the Heisenberg spin-1/2 ferromagnet" *Phys. Lett.* **1966**, *22*, 269-271.
- (85) Baker, G. A., Gilbert, H. E., Eve, J., Rushbrooke, G. S. "On the Heisenberg spin-1/2 ferromagnetic models" *Phys. Lett.* **1966**, *20*, 146-147.
- (86) Baker, G. A., Gilbert, H. E., Eve, J., Rushbrooke, G. S. "On the two dimensional, spin-1/2 Heisenberg ferromagnetic models" *Phys. Lett.* **1967**, *25A*, 207-209.
- (87) Brown, I. D., Altermatt, D. "Bond-valence parameters obtained from a systematic analysis of the inorganic crystal structure database" *Acta Cryst.* **1985**, *B41*, 244-247.
- (88) Brese, N. E., O'keeffe, M. "Bond-valence parameters for solids" *Acta Cryst.* **1991**, *B47*, 192-197.
- (89) Yamada, I. "Magnetic properties of potassium tetrafluorocuprate(II). Transparent two-dimensional ferromagnet" *Journal of the Physical Society of Japan* **1972**, *33*, 979-988.
- (90) Koo, H. J., Whangbo, M. H. "Analysis of the Spin Exchange Interactions in the Extended Magnetic Solids K_2NiF_4 , K_2CuF_4 , La_2CuO_4 , Nd_2CuO_4 , $KNiF_3$, and $KCuF_3$ " *Journal of Solid State Chemistry* **2000**, *151*, 96-101.
- (91) Miedema, A. R., de Jongh, L. J. "Experiments on simple magnetic model systems" *Adv. Phys.* **1974**, *23*.
- (92) Legrand, E., Plumier, R. "Neutron diffraction investigation of antiferromagnetic K_2NiF_4 structure" *Physica Status Solidi* **1962**, *2*, 317-320.
- (93) Legrand, E., Van den Bosch, A. "Magnetic measurements on compounds with K_2NiF_4 structure" *Solid State Communications* **1969**, *7*, 1191-1194.
- (94) Birgeneau, R. J., Guggenheim, H. J., Shirane, G. "Neutron scattering from potassium tetrafluoronickelate(II): a two dimensional Heisenberg antiferromagnet" *Physical Review Letters* **1969**, *22*, 720-723.

- (95) Skalyo, J., Jr., Shirane, G., Birgeneau, R. J., Guggenheim, H. J. "Magnons at low and high temperatures in the planar antiferromagnet K_2NiF_4 " *Physical Review Letters* **1969**, 23, 1394-1397.
- (96) Keimer, B., Harony, A., Auerbach, A., Birgeneau, R. J., Cassanho, A., Endoh, Y., Erwin, R. W., Kastner, M. A., Shirane, G. "Neel transition and sublattice magnetization of pure and doped La_2CuO_4 " *Phys. Rev. B* **1992**, 45, 7430-7435.
- (97) Endoh, Y., Yamada, K., Birgeneau, R. J., Gabbe, D. R., Jenssen, H. P., Kaster, M. A., Peters, C. J., Picone, P. J., Thurston, T. R., Tranquada, J. M., Shirane, G., Hidaka, Y., Oda, M., Enomoto, Y., Suzuki, M., Marakami, T. "Static and dynamic spin correlations in pure and doped La_2CuO_4 " *Phys. Rev. B* **1998**, 37, 7443.
- (98) Soukoulis, C. M., Datta, S., Lee, Y. H. "Spin wave theory for Heisenberg antiferromagnets" *Phys. Rev. B* **1991**, 44, 446.
- (99) Du, A., Wei, G. Z., Hu, Q. L. "Neel temperature of orthorhombic La_2CuO_4 " *Journal of Magnetism and Magnetic Materials* **1995**, 146, 201-202.
- (100) Li, W. H., Perry, C. H., Sokoloff, J. B., Wagner, V., Chen, M. E., Shirane, G. "Polarized neutron studies of forbidden magnons in the two-dimensional ferromagnet dipotassium tetrafluorocuprate(II)" *Physical Review B: Condensed Matter and Materials Physics* **1987**, 35, 1891-1898.
- (101) Moussa, F., Villain, J. "Spin-wave lineshape in two-dimensional dipotassium copper tetrafluoride: neutron experiments and theory" *Journal of Physics C: Solid State Physics* **1976**, 9, 4433-4451.
- (102) Borovik-Romanov, A. S., Kreines, N. M., Laiho, R., Levola, T., Zhotikov, V. G. "Optical detection of ferromagnetic resonance in K_2CuF_4 " *J. Phys. C* **1980**, 13, 879-885.
- (103) Feldkemper, S., Weber, W., Schulenbring, J., Richter, J. "Ferromagnetic coupling in nonmetallic Cu(II) compounds" *Phys. Rev. B* **1995**, 52, 313-323.
- (104) Hidaka, M., Inoue, K., Yamada, I., Walker, P. J. "X-ray diffraction study of the crystal structures of potassium copper fluoride (K_2CuF_4) and potassium copper zinc fluoride ($K_2Cu_xZn_{1-x}F_4$)" *Physica B+C: Physics of Condensed Matter + Atomic, Molecular and Plasma Physics, Optics (Amsterdam)* **1983**, 121, 343-350.

- (105) Ito, Y., Akimitsu, J. "Observation of orbital ordering in K_2CuF_4 " *Journal of the Physical Society of Japan* **1976**, *40*, 1333-1338.
- (106) Khomskii, D. I., Kugel, K. I. "Orbital and magnetic structure of two-dimensional ferromagnets with Jahn-Teller ions" *Solid State Communications* **1973**, *13*, 763-766.
- (107) Jorgenson, J. D., Scheuttler, H. B., Hinks, D. G., Capone, D. W., Zhang, K., Brodsky, M. B., Scalapino, D. J. "Lattice instability and high T_C superconductivity in $La_{2-x}Ba_xCuO_4$ " *Phys. Rev. Lett.* **1987**, *58*, 1024-1027.
- (108) Longo, J. M., Raccach, P. M. "The structure of La_2CuO_4 and $LaSrVO_4$ " *Journal of Solid State Chemistry* **1973**, *6*, 526-531.
- (109) Smart, L., Moore, E. *Solid State Chemistry: An Introduction*, 1992.
- (110) Kresin, V. Z., Wolf, S. A. *Fundamentals of Superconductivity*; Plenum Press: New York, 1990.
- (111) Aharony, A., Birgeneau, R. J., Coniglio, A., Kaster, M. A., Stanley, H. E. "Magnetic phase diagram and magnetic pairing in doped La_2CuO_4 " *Phys. Rev. Lett.* **1988**, *60*, 1330-1333.
- (112) Dagotto, E. "Correlated electrons in high-temperature superconductors" *Reviews of Modern Physics* **1994**, *66*, 763-840.
- (113) Shirley, R. In; The Lattice Press: 41 Guildford Park Avenue, Guildford, Surrey GU27NL, England, 2000.
- (114) Axe, J. D., Moudden, A. H., Hohlwein, D., Cox, D. E., Mohanty, K. M., Moodenbaugh, A. R., Xu, Y. "Structural phase transformations and superconductivity in $La_{2-x}Ba_xCuO_4$ " *Phys. Rev. Lett.* **1989**, *62*, 2751-2754.
- (115) Bednorz, J. G., Takashige, M., Mueller, B. G. "Susceptibility measurements support high T_C superconductivity in the Ba-La-Cu-O system" *Europhys. Lett.* **1987**, *3*, 379-385.
- (116) Bozin, E. S., Billinge, S. J. L., Kwei, G. H. "Re-examination of the second-order structural phase transition in $La_{2-x}A_xCuO_4$ ($A=Ba,Sr$)" *Physica B* **1998**, *241-243*, 795-797.

(117) Braden, M., Schnelle, W., Schwarz, W., Pyka, N., Heger, G., Fisk, Z., Gamayunov, K., Tanaka, I., Kojima, H. "Elastic and inelastic neutron scattering studies on the tetragonal to orthorhombic phase transition of $\text{La}_{2-x}\text{Sr}_x\text{CuO}_4$ " *Z. Phys. B* **1994**, *94*, 29-37.

(118) Crawford, M. K., Harlow, R. L., McCarron, E. M., Cox, D. E., Huang, Q. "Effects of structural phase transitions on superconductivity and magnetism in substituted derivatives of La_2CuO_4 " *Physica C* **1994**, *235-240*, 170-173.

(119) Day, P., Rosseinsky, M., Prassides, K., David, W. I. F., Moze, O., Soper, A. "Temperature dependence of the crystal structure of the ceramic superconductor $\text{La}_{1.85}\text{Sr}_{0.15}\text{CuO}_4$: a powder diffraction neutron study" *J. Phys. C* **1987**, *20*, L429-L434.

(120) Frey, F. "Diffuse scattering from disordered crystals" *Acta Cryst. B.* **1995**, *51*, 592-603.

(121) Proffen, T., Billinge, S. J. L. "PDFFIT, a program for full profile structural refinement of the atomic pair distribution function" *J. Appl. Crystallogr.* **1999**, *32*, 572-575.

Vita

Michelle was born on April 5, 1980 in Allen Park Michigan. She graduated from Allen Park High School as salutatorian in 1998. After high school, she attended Hillsdale College in Hillsdale Michigan where she majored in Chemistry and minored in Mathematics. In order to help put herself through school she worked at a coffee shop and a pizzeria along with working at a summer internship with Bill Hase at Wayne State University doing computational chemistry. She graduated cum laude from Hillsdale College in May 2002 and began graduate school at the University of Tennessee in August 2002. Her first area of research included using computational chemistry to perform molecular dynamics calculations on different atmospheric reactions. After a year and a half, she decided to change her research concentration and became a fluorine chemist. Upon receiving her Master's Degree from the University of Tennessee, she will be attending The Ohio State University to pursue her Ph.D.